Politecnico di Milano

School of Industrial and Information Engineering

Energy Engineering Master of Science

Optical design of a Beam Down Linear Fresnel Reflector for process heat production

Supervisor: Prof. Marco Binotti

Author: Lorenzo Piombini

Academic year:2022/2023

Ringraziamenti

Sono arrivato alla conclusione di questo percorso di studi. Durante questo capitolo della mia vita ho imparato molto, sia scolasticamente che, soprattutto, umanamente: ho scoperto i miei limiti ed imparato a spingerli sempre un po' più in là, ho incontrato persone che mi hanno mostrato modi diversi di pensare e vivere permettendomi così di crescere ed ho imparato che con la tenacia ed il sacrificio si possono raggiungere gli obiettivi ai quali si ambisce.
Questo percorso sarebbe risultato impossibile senza l'appoggio di molte persone. Per questo vorrei ringraziare di cuore:

Il professor Marco Binotti, per la sua immensa disponibilità, per aver sempre messo ordine nelle mie idee ed avermi spinto a scavare sempre un po' più a fondo.

Matteo, per le infinite e agguerrite partite a tennis, per i tanti consigli e soprattutto per la lunga e profonda amicizia che condividiamo sin dall'asilo.

Sara ed Eleonora, per essere sempre pronte ad ascoltarmi quando ho bisogno di sfogarmi, supportandomi sempre senza mai giudicare.

La mia famiglia per essere stata il mio punto di riferimento nei periodi burrascosi.

I miei genitori e mio fratello Luca, per aver creduto in me ed avermi sostenuto durante i momenti di difficoltà, per avermi permesso di intraprendere questa lunga avventura milanese e per non aver mai smesso di volermi bene.

Abstract

The addition of a beam down stage to a conventional Linear Fresnel Reflector generates an optical system that focuses the sun rays on the ground, therefore removing all the constraints on the dimension and weight of the receiver set by commercial LFR systems. This thesis consists in the geometrical and optical analysis of a system so built. The effect of the main geometrical parameters of the system (such as primary focus height, number of mirror rows, mirror spacing, etc.) on the width of the receiver has been investigated for a range of configurations with a Matlab model. Through a SolTrace model, the main causes of efficiency loss have been identified and the Incidence Angle Modifier curves obtained in order to determine the instantaneous, daily and annual optical efficiency of the system. After the introduction of the radiative losses of the absorber, an optimal configuration is selected. The global daily efficiency of the chose configuration amounts to 39.87% when the system operates at a constant temperature of 500°C

Sommario

L'aggiunta di uno stadio beam down ad un convenzionale sistema Fresnel lineare genera un sistema ottico che riflette i raggi solari verso il suolo, permettendo di rimuovere i vincoli sulla dimensione ed il peso del ricevitore tipici dei sistemi Fresnel lineari commerciali. Questa tesi consiste nell'analisi geometrica ed ottica di un sistema così costruito. L'effetto dei principali parametri geometrici del sistema (altezza del fuoco primario, numero di file di specchi, spaziatura degli specchi, ecc.) sull'ampiezza del ricevitore sono state investigate per un range di configurazioni con un modello Matlab. Attraverso un modello SolTrace, le principali cause di perdita di rendimento sono state identificate e le curve di Incidence Angle Modifier sono state ottenute per determinare l'efficienza ottica istantanea, giornaliera ed annuale del sistema. Dopo l'introduzione delle perdite radiative al ricevitore, una configurazione ottimale del sistema è stata selezionata. L'efficienza globale giornaliera della configurazione scelta ammonta a 39.87% quando il sistema opera ad una temperatura di 500°C.

Table of Contents

1 Introduction

1.1 Present energy background

The energy consumption has almost constantly increased over the past decades, mainly as a result of the expansion of the transport, industrial and residential sectors. This trend is expected to exacerbate with the growth of the developing countries. As the global energy mix still relies heavily on energy from fossil fuel, the increase in energy demand will inevitably result in the increase of greenhouse gases emissions mainly from oil, natural gas and coal. The reduction of these emissions is imperative to check the climb of the average world temperature. To this end, the Paris Agreement in 2015 saw the participation of almost 200 countries covering more than 90% of the global emissions. The main targets of the Agreement were to keep the global temperature rise below the 2°C over the 1990's levels and put into effect policies to decrease the cost of renewable energy technologies. In 2019 the European Union released the European Green Deal, a document in which the EU states its goals regarding the environment: the target of carbon neutrality is set for year 2050. One of the main points made by both treaties is the boost needed by renewable energies in terms of investment and research to increase their share in the global energy mix [1].
Renewable energies' share in the electricity generation sector has increased rapidly in the last decade as shown in *Figure 1-1*: considering solar, wind and hydro the share of renewables has reached 24.5% according to the International Energy Agency (IEA).

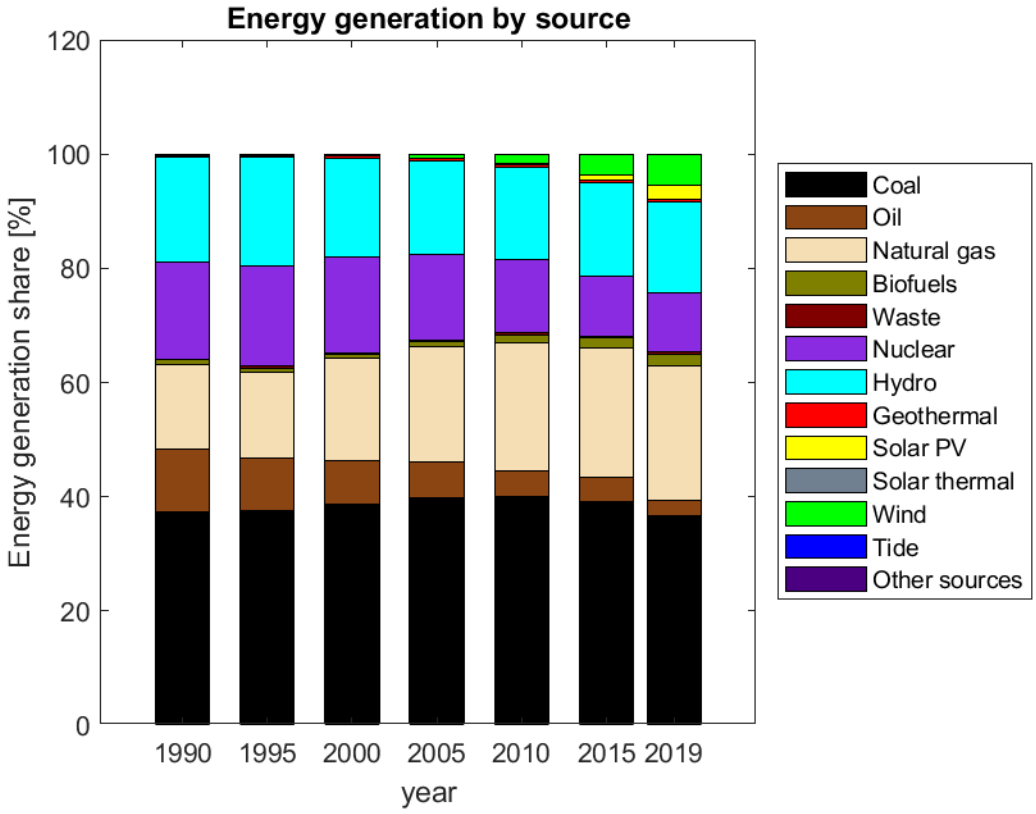

Figure 1-1 Energy generation mix from 1990 to 2019 as reported by the International Energy Agency (IEA) [2].

Wind and solar energy have become particularly relevant in recent years, being mainly responsible for the increase of the renewables share. For both different technologies have developed in the last few decades but only recently became competitive on the energy market. Among these, concentrating solar power (CSP) has seen a huge increase in energy output in the past ten years [2].

1.2 Concentrating solar power (CSP)

1.2.1 Main principles

The main principle of a CSP plant is to concentrate the solar rays on the surface of a receiver (or absorber), increase its temperature and then use it to supply heat to an underlying process.

The energy source of the technology is the sun. The sun can be considered as a black body at a temperature of 5777 K and its irradiance reaches more than 63000 kW/m^2. As the radiation travels through the space separating the sun from Earth, it is dispersed: the average extra-terrestrial irradiation is about 1367 W/m^2. After considering the attenuation effect of Earth's atmosphere this value can be lower than 1000 W/m^2. The actual value of direct normal irradiance is a function of latitude, altitude, cloud coverage, air pressure, pollution, cloud coverage, solar hour and day of the year.
The choice of location is then a key factor to design high performance CSP plants: the higher the average solar irradiation, the higher the initial amount of energy available for collection to the system.

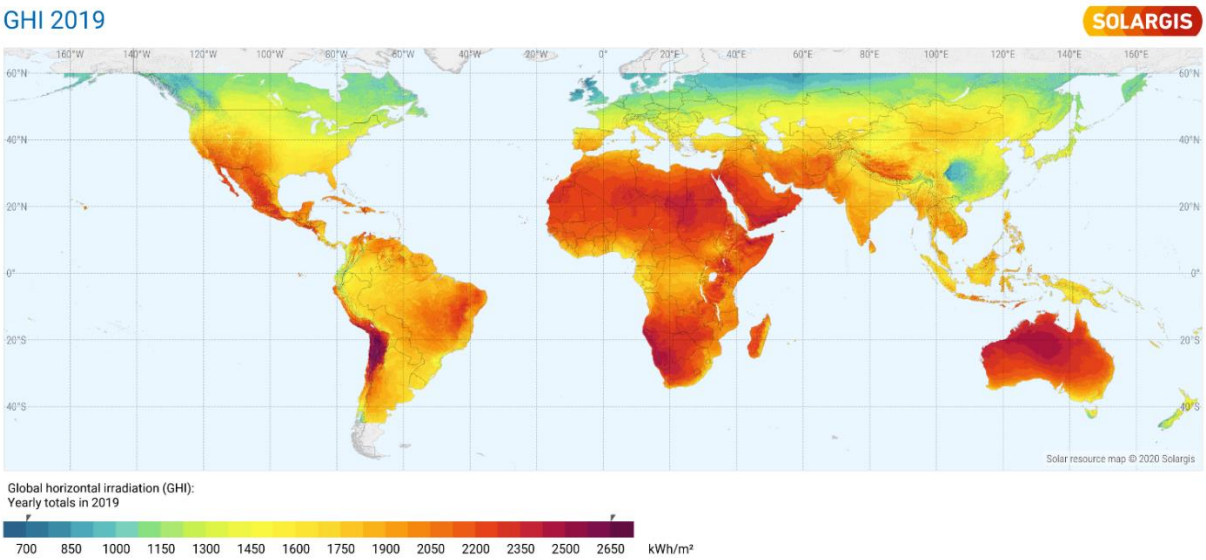

Figure 1-2 Annual average irradiation world map [3].

The collection of solar power is usually achieved through a field of high-reflectance mirrors that redirect and concentrate the sunlight on the surface of an absorber: the higher the concentration capability of the optical system, the higher the heat flux that will hit the receiver and therefore the higher its temperature will be.
If the underlying process of the CSP plant were a thermodynamic cycle for power production, the advantage of a high absorber temperature can be understood from the definition of the Carnot efficiency for a thermodynamic cycle:

$$\eta_{Carnot} = 1 - \frac{T_{amb}}{T_{abs}} \tag{1.1}$$

If the temperature of the receiver increases, the maximum efficiency of the cycle will increase.

However, this is not the only relevant aspect in the definition of the global efficiency of concentrating system: as the absorber increases its temperature, it will begin to exchange radiatively with the surrounding environment, causing a dispersion of the heat concentrated on its surface.
The power so dispersed can be expressed as:

$$\dot{Q}_{loss} = \sigma \varepsilon S_{abs}(T_{abs}^4 - T_a^4) \tag{1.2}$$

where σ is the Stefan-Boltzmann constant ($\sigma = 5.67\ 10^{-8} \frac{W}{m^2 K^4}$) and ε is the hemispherical emissivity of the absorber surface.
The absorber will have a certain absorption coefficient α_{abs} lower than one, just like the reflectivity ρ_m of the concentrating mirrors won't be unitary. If all the power collected by the mirror field is conveyed on the absorber, the thermal power impinging on the absorber can be expressed as:

$$\dot{Q}_{abs} = DNI\ (\alpha_{abs}\rho_m)\ S_m \tag{1.3}$$

where S_m is the total collective area of the mirror field and DNI the Direct Normal Irradiance.
The useful power will be de difference between the power impinging on the absorber and the one leaving it due to the radiative loss:

$$\dot{Q}_u = DNI\ (\alpha_{abs}\rho_m)\ S_m - \sigma \varepsilon S_{abs}(T_{abs}^4 - T_a^4) \tag{1.4}$$

The geometric concentration ratio is defined as the ratio between the total mirror field area and the absorber area:

$$C_g = \frac{S_m}{S_{abs}} \tag{1.5}$$

This quantity gives a measure of what is the concentration capability of the optical system. It can be used to rewrite equation (1.4) as follows:

$$\dot{Q}_u = S_{abs}\left(DNI\ (\alpha_{abs}\rho_m)\ C_g - \sigma \varepsilon (T_{abs}^4 - T_a^4)\right) \tag{1.6}$$

The receiver efficiency is defined as the ratio between the useful power on the absorber and the power intercepted by the mirror field:

$$\eta_{rec} = \frac{\dot{Q}_u}{\dot{Q}_m} = \frac{S_{abs}\left(DNI\ (\alpha_{abs}\rho_m)\ C_g - \sigma \varepsilon (T_{abs}^4 - T_a^4)\right)}{DNI\ S_m} = (\alpha_{abs}\rho_m) - \frac{\sigma \varepsilon (T_{abs}^4 - T_a^4)}{DNI\ C_g} \tag{1.7}$$

It is interesting to notice that the receiver efficiency can't exceed the value of $\alpha_{abs}\rho_m$ which represents the maximum optical efficiency of the system.

The absorber efficiency tends to decrease with the absorber temperature while the Carnot efficiency increases. The global efficiency of the system can then be expressed as:

$$\eta_{global} = \eta_{Carnot}\eta_{rec} \tag{1.8}$$

As shown in *Figure 1-3*, the global efficiency of the CSP systems presents a maximum over which is no longer convenient operate the plant. The temperature for which the maximum is achieved increases as the geometric concentration ratio is increased. At the same time the maximum efficiency reached increases more and more increasing C_g: it is then reasonable to decrease as much as possible the receiver area to increase the efficiency. A thermodynamic limit, however, exists on the concentration ratio: if the absorber area could be decreased at leisure, once equilibrium with the ambient and the underlying process is reached, the absorber temperature could increase so much as to overcome the superficial one of the sun, violating the second principle of thermodynamics as the sun radiation would have travelled from the sun to an hotter surface without any other effect [4].

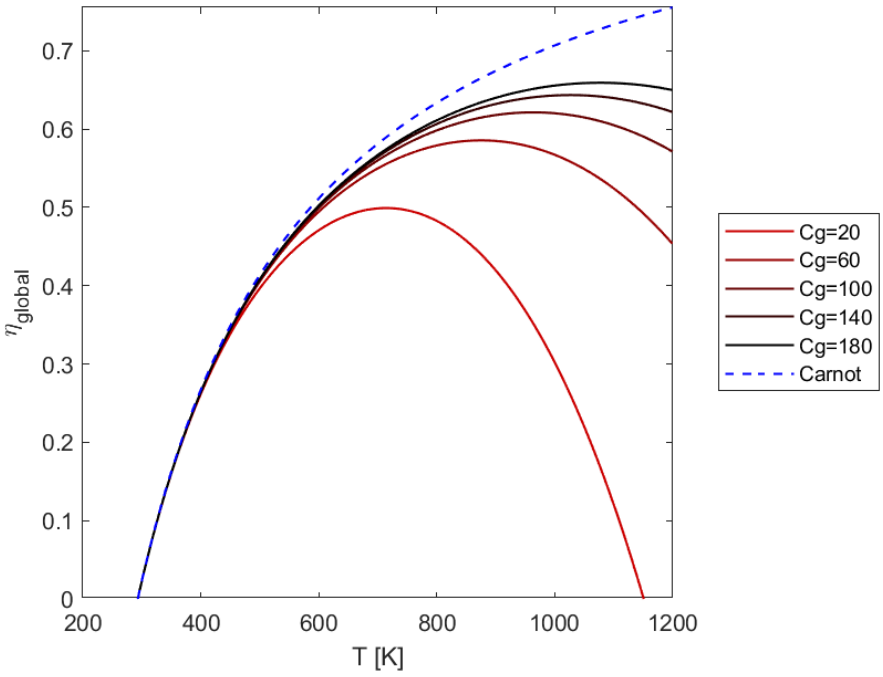

Figure 1-3 Global efficiency for a CSP system as function of the absorber temperature and parametrised for geometric concentrating ratio.

1.3 Definition of solar angles

The position of the sun in the sky is function of solar hour (*H*), site latitude (*L*), and day of the year (*D*) [8]. For simplicity's sake, we can assume that the symmetry axis of the system is aligned with the North-South axis. This way the longitudinal plane coincides with the North-South plane and the transversal plane with the East-West one.
The coordinate system of the field is set as follows: the positive direction of the x-axis points East, the positive direction of the y-axis points North and the positive direction of the z-axis points to the zenith (see Fig.1).

The sun vector is defined as the vector that, originating in the coordinate's system origin, points towards the centre of the sun.

Solar azimuth (γ_s) is the angle that the projection of the sun vector on the xy-plane forms with the negative part of the y-axis. So γ_s is considered 0 when the sun is due South and positive when the sun is in the South-West quadrant.

Solar zenith (θ_z) is the angle that the solar vector forms with the positive part of the z-axis. θ_z is considered 0 when the sun is in the zenith position and always has positive value.

Three more angles are useful to describe the sun position: transversal, longitudinal and incidence angle.

The transversal incidence angle (θ_t) is the angle that the projection of the sun vector on the transversal plane forms with the positive part of the z-axis.

The longitudinal incidence angle (θ_l) is the angle that the projection of the sun vector on the longitudinal plane forms with the positive part of the z-axis.

The angle θ_i is the angle between the sun vector and its projection of the transversal plane.

Based on sun-earth geometry [8], once day of the year, latitude and solar time are set, the position of the sun can be determined in terms of zenith and azimuth angles through the following equations:

$$\omega = 15(H - 12)\ hour\ angle \tag{1.9}$$

$$\delta = 23{,}45\ sin\left(360\frac{284 + D}{365}\right)\ declination \tag{1.10}$$

$$\alpha_s = sin^{-1}(cos(L)\,cos(\delta)\,cos(\omega) + sin(L)\,sin(\delta))\ \ solar\ angle\ (elevation\ angle) \tag{1.11}$$

$$\gamma_s = cos^{-1}((sin(\alpha_s)\,sin(L) - sin(\delta))/(cos(\alpha_s)\,cos(L)))\ \ \ azimuth\ angle \tag{1.12}$$

where *hour angle* is the portion of the 365° that the Earth spans in the course of the day that have been covered starting from noon (solar time H=12), the *declination* is the angle that the sun rays form with the equatorial plane and the *elevation angle* is the complementary to 90° of the zenith angle ($\theta_z = 90 - \alpha_s$).

The sun vector can be expressed as a function of θ_z and γ_s:

$$\begin{cases} x_s = \sin(\gamma_s)\sin(\theta_z) \\ y_s = -\cos(\gamma_s)\sin(\theta_z) \\ z_s = \cos(\theta_z) \end{cases} \tag{1.13}$$

The sun vector so expressed must still be normalized to become a unit vector useful for calculations.
The angles that describe the projection of the sun vector on the transversal and longitudinal plane can be also computed as a function of θ_z and γ_s [5] :

$$\theta_t = \tan^{-1}(|\sin(\gamma_s)|\tan(\theta_z)) \tag{1.14}$$

$$\theta_l = \tan^{-1}(\cos(\gamma_s)\tan(\theta_z)) \tag{1.15}$$

$$\theta_i = \sin^{-1}(\cos(\gamma_s)\sin(\theta_z)) \tag{1.16}$$

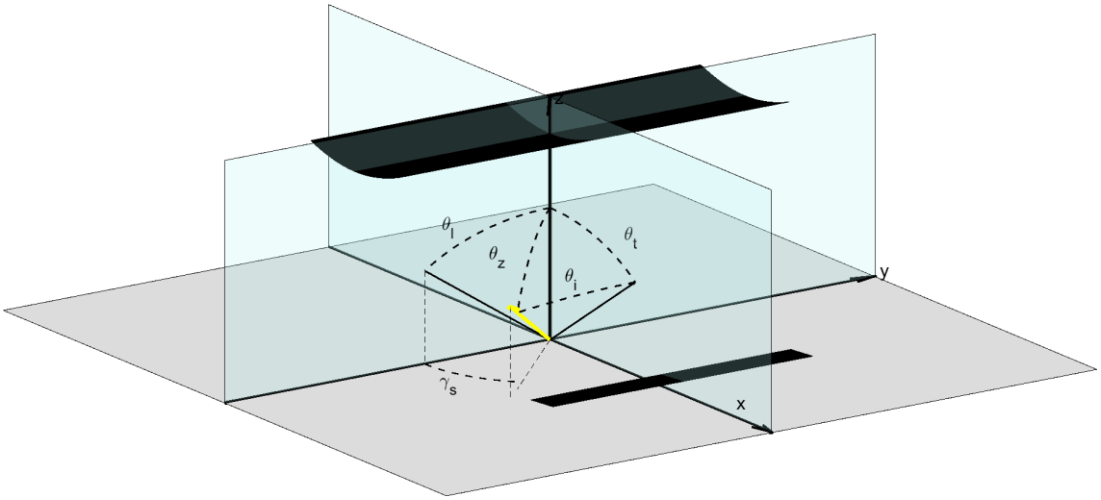

Figure 1-4 A representation of the reference system and the main solar angles.

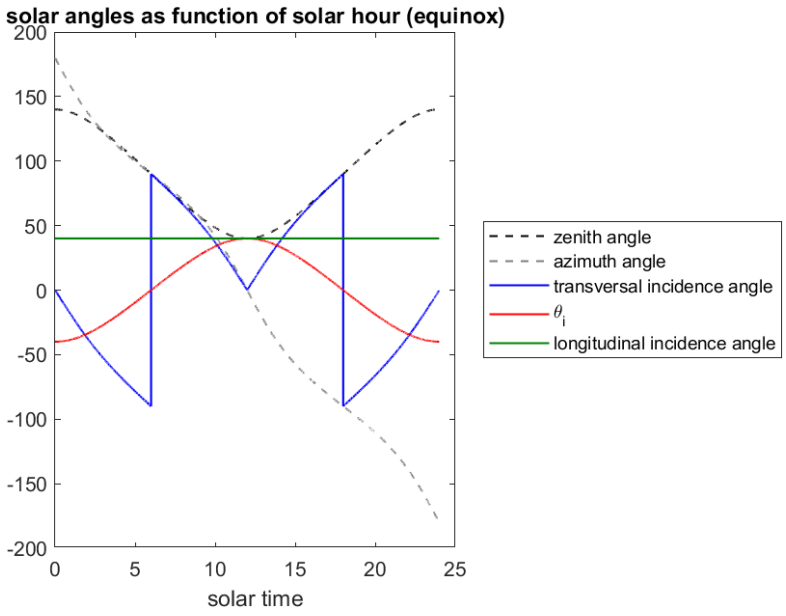

Figure 1-5 Solar angles as function of the solar hour in the day of the equinox for a latitude of 40°N.

In *Figure 1-5* the values of the different solar angles previously defined are shown for the day of the equinox (spring or autumn).

It is relevant to mention that at solar noon, the zenith, longitudinal incidence and θ_i angles assume the same value. By applying the equations listed in this Chapter, it can be noticed that this value is equal to the value of the latitude considered (40°N for this example).

1.4 Law of reflection

Snell's law of reflection describes the relationships existing between incident and reflected rays off a surface in the case in which the surface is perfectly specular, i.e., it doesn't introduce any reflection errors due to micro-roughness or mirror misshaping. For this reason, this law is also known as law of specular reflection.

We consider a vectorial notation where all vectors point away from the surface[4]. We define the following vectors:

$$\vec{\imath} = direction\ of\ incident\ ray$$

$$\vec{n} = direction\ of\ normal\ of\ reflector\ surface$$

$$\vec{r} = direction\ of\ reflected\ ray$$

The law of reflection states that:

- the angle of incidence equals the angle reflections:

$$\vec{\imath} \cdot \vec{n} = \vec{r} \cdot \vec{n} \tag{1.17}$$

- $\vec{\imath}$, $\vec{r}$ and $\vec{n}$ lay on the same plane:

$$(\vec{\imath} \times \vec{r}) \cdot \vec{n} = 0 \tag{1.18}$$

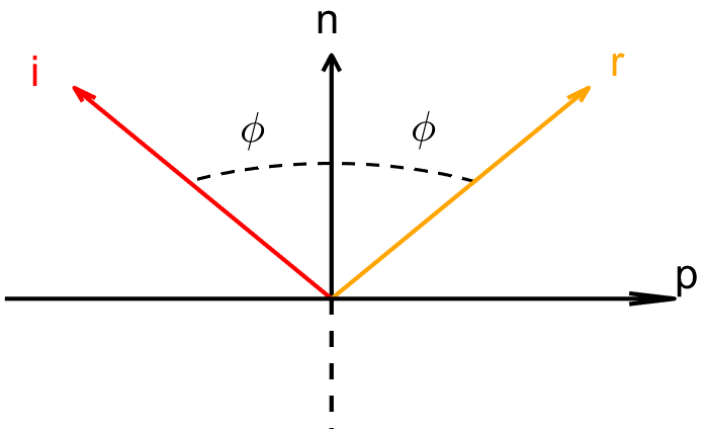

Figure 1-6 Unit vectors for the law of specular reflection

These two equations allow to, given the knowledge of two of the unit vectors, to compute the remaining one. Two different cases can occur: either both incidence and reflected ray are known and the surface normal in that point is required or incidence ray and normal are known and the direction of the reflected ray is required.

For both cases the following system can written:

$$\begin{cases} \vec{\imath} = -\sin(\phi)\ \vec{p} + \cos(\phi)\ \vec{n} \\ \vec{r} = \sin(\phi)\ \vec{p} + \cos(\phi)\ \vec{n} \end{cases} \tag{1.19}$$

where $\vec{p}$ is the vector perpendicular to $\vec{n}$ but still laying on the same plane as the others.

Case 1: incident and reflected ray known, surface normal unknown:

The two equations of system (1.19) can be added side to side to obtain:

$$\vec{\imath} + \vec{r} = 2\cos(\phi)\,\vec{n} = 2(\vec{\imath} \cdot \vec{n})\vec{n} \tag{1.20}$$

Since $\vec{n}$ is unknown, so is the angle ϕ. Using trigonometry, it can be demonstrated that:

$$2\cos(\phi) = \sqrt{2 + 2(\vec{\imath} \cdot \vec{r})} \tag{1.21}$$

It follows that:

$$\vec{n} = \frac{\vec{\imath} + \vec{r}}{\sqrt{2 + 2(\vec{\imath} \cdot \vec{r})}} \tag{1.22}$$

The denominator is now only a function of incident and reflected vectors and it can be computed. The denominator can be recognised as the module of $\vec{\imath} + \vec{r}$. Equation (1.22) can be rewritten in a more intuitive form as:

$$\vec{n} = \frac{\vec{\imath} + \vec{r}}{|\vec{\imath} + \vec{r}|} \tag{1.23}$$

Case 2: incidence ray and surface normal known, reflected direction unknown:

From the first equation of system (1.19), the term $(\sin(\phi)\ \vec{p})$ can be isolated and put in the second equation.

It follows that:

$$\vec{r} = -\vec{\imath} + 2(\vec{\imath} \cdot \vec{n})\vec{n} \tag{1.24}$$

1.5 CSP technologies

Different kinds of CSP technologies have been developed over the decades and they can be classified in different ways. The main classification is the one based on the focusing method: point focus and line focus plants. Each can then be divided in continuous or partitioned field (*Figure 1-7*).

These plants either heat the working fluid of the thermodynamic cycle (direct cycle) or a heat transfer fluid (HTF) that, via heat exchanger, heats the working fluid (indirect cycle).

1.5.1 Point focus

In point focus plants, the receiver consists of a single point towards which the sun rays are reflected by a mirror field. Two kinds of point focus technologies exist: solar dish and solar tower plants.

Solar dish

The system consists of a parabolic dish that concentrates the sunlight on the absorber positioned in their focus. The dish has a three-dimensional tracking system to follow the trajectory of the sun during the day and maximise the amount of radiation conveyed on the receiver. The main limit to their concentration ratio is that their diameter dimension that can't exceed 7-8 meters for technical reasons.
The fluid passing through the absorber is a heat transfer fluid that can reach temperatures up to 750°C.
The typical electrical power obtained by one single dish is between 10 and 25 kW.

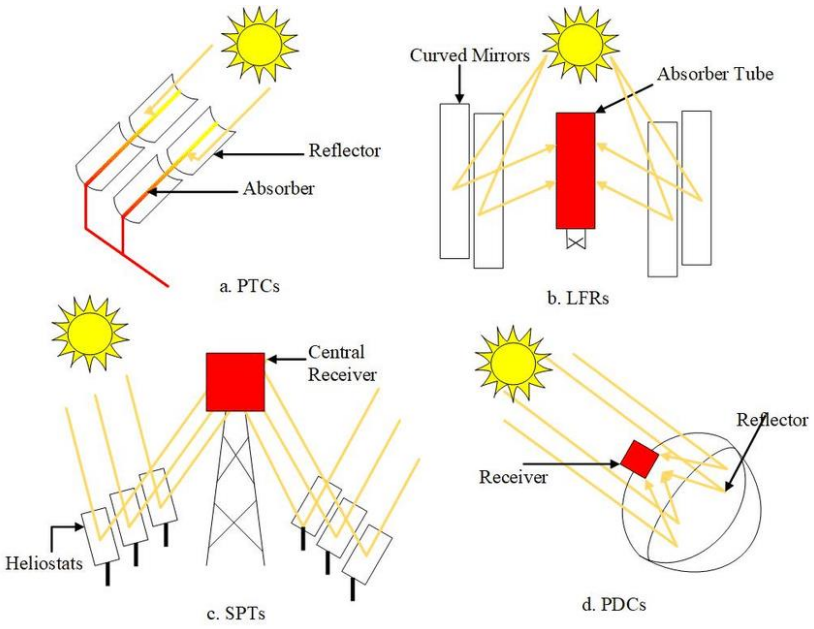

Figure 1-7 Different types of CSP plants.

Solar Tower

In this case, the collecting system consists of a field of heliostats that redirect the sun rays towards an absorber positioned at the top of a tower. The heliostats track the position of the sun thanks to a three-dimensional tracking system. Either the working fluid or a heat transfer fluid can flow in the absorber. The tower is usually higher than 100 meters and the size of the plants is of the order of tens of MWs. Examples of demonstrative plants are Planta Solar 10 and Planta solar 20, built in Spain near Seville: the two plants yield respectively 10 and 20 MW. The heliostat fields use respectively 645 and 1255 heliostats, each with and area of 120 m^2.

1.5.2 Line focus

In the line focus technology, the heliostat field redirects the sun rays towards a linear receiver. The main kinds of line focus CSP plants are the parabolic trough collector (PTC) and the linear Fresnel reflector (LFR).

Parabolic Trough Collector

A parabolic mirror reflects the sunlight on an absorber tube put in its focus. The trough can rotate only around its longitudinal axis, so the tracking system is only two-dimensional. As for the solar dish, the main limit to the concentration ratio is given by the aperture of the mirror (usually around 5 m) that must be limited because of gravity, wind loads and technical difficulty of realising of a large curved reflective surface. Conversely the trough is usually long (60-100 m) to reduce end-losses.
An example of CSP plant using PTC technology is the Solana power plant (USA): built in 2013, this plant reaches a power of 280 MWe and temperatures of about 370°C.

Figure 1-8 Solana solar plant in California.

Linear Fresnel Reflector

The LFR optical system breaks apart the parabolic mirror of a PTC to obtain smaller and cheaper almost-flat mirrors that redirect the sunlight towards a receiver put at a certain height. The receiver is fixed while the mirrors can rotate around their longitudinal axis to track the sun position.
An example of a working LFR CSP plant is the one sited in Lanzhou Dacheng Dunhuang: the temperature of the HTF reaches 550°C and the nominal power of the plant is 50 MW.

Figure 1-9 Lanzhou Dacheng Dunhuang plant in China.

The longitudinal length of the mirrors is of 1100 m for a total collective area of 1270000 m^2. As shown in *Figure 1-9*, the technology relies on modules deployed in series to achieve the required longitudinal length.

Each module, not longer than 3-4 meters, is comprised of a certain number of mirror rows (20 in the case of the Lanzhou Dacheng Dunhuang plant).
Sometimes a secondary concentrator is put on top the receiver to capture some rays that weren't correctly reflected to increase the efficiency of the system.

1.6 BDLFR systems and Beam-Down technology

A Beam Down Linear Fresnel Reflector (BDLFR) system consists of an array of primary reflectors (field mirrors) that redirect the sun beams up towards a secondary reflector (also called Beam Down reflector) put at a certain height. The sun rays are then reflected towards the ground, where they hit the surface of the receiver.

The BDLFR mirror field is analogous to the one of an LFR system and it inherits some of its strengths: the field mirrors are small and flat or only slightly curved, making them cheaper compared with the ones used for PTC or tower systems and less susceptible to wind and gravity loads thanks to a lighter support structure [5]. This last feature also plays a role in reducing the tracking energy consumption when coupled with a fixed receiver. Furthermore, the land occupation is minimized since, due to the smaller mirrors, shading is considerably reduced compared to PTC plants. Finally, positioning the mirrors at ground level makes them easier to clean.

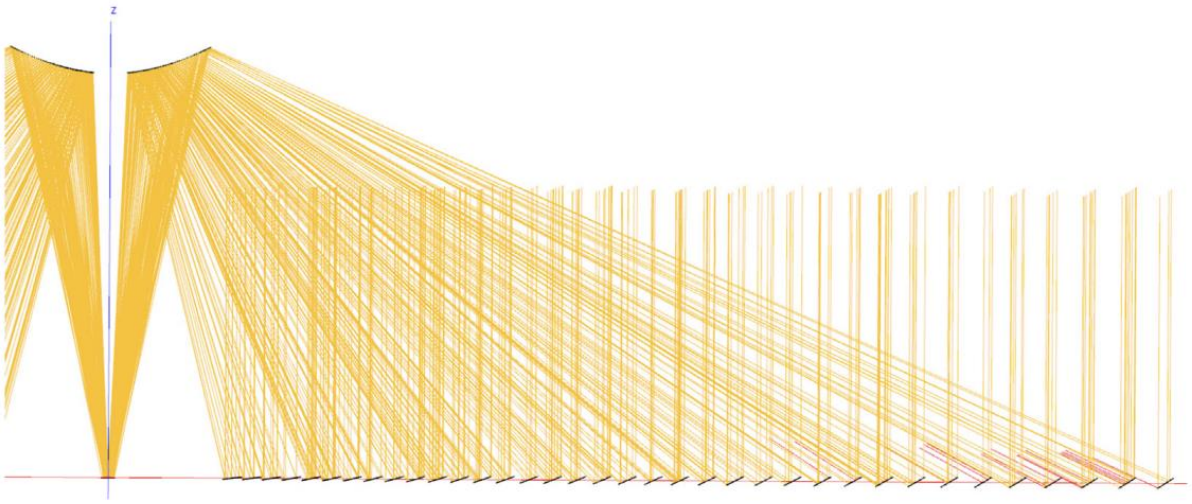

Figure 1-10 SolTrace 2D view of a BDLFR system with 40 mirror rows [6].

The main limitation of a LFR system is that the elevated receiver must be as light as possible to reduce the cost of the support structure. In applications like thermochemical processes, such as biomass pyrolysis or gasification or hydrogen production, the receiver is usually large and heavy, therefore its placement on top of the mirror field is impractical. This is where the beam-down technology becomes useful in these processes, allowing to position the receiver on the ground.

The BD mirror can either be a hyperbolic cylinder or an elliptic cylinder. In both cases the mirror field will direct the sun rays towards the focus point of the BD mirror that is situated above the cylinder in case of a hyperbolic BD reflector and below in the case of the elliptic one.

As discussed by Akiba Segal and Michael Epstein [7], the elliptic BD has lower performances than the hyperbolic BD, achieving lower concentration ratios for the same geometry of the system. In the following analysis the hyperbolic BD is the adopted.

The section of the hyperbolic cylinder, done with any plane parallel to the transversal one, is one branch of a hyperbola.

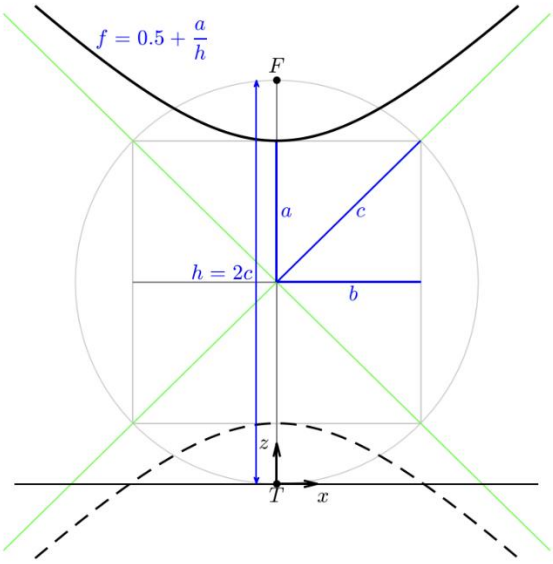

Figure 1-11 Upper branch of the beam-down hyperbola with its main geometric parameters. [6]

The upper focus of the hyperbola is called primary focus point (point F in Figure 1-11) The primary focus line is the geometric locus of all the primary focus points.
The lower (secondary) focus of the hyperbola instead coincides with the y-axis (point T in Figure 1-11).
This way, any ray directed towards the primary focus is reflected by the hyperbolic cylinder toward the secondary focus.
To define the geometry of the branch of hyperbola a hyperbola shape factor is introduced:

$$f = \frac{a + c}{2c} = 0.5 + \frac{a}{h} \tag{1.25}$$

where a is the length of the main semiaxis, b the length of the secondary semiaxis and h the primary focus height. The hyperbola parameters are correlated by the equation:

$$c = \sqrt{a^2 + b^2} = h/2 \tag{1.26}$$

and the hyperbola equation can be expressed as:

$$z = \frac{a}{b}\sqrt{x^2 + b^2} + c \tag{1.27}$$

The hyperbola shape factor can assume values ranging from 0.5 up to 1: in the first case the hyperbola will be a completely flat surface, in the second a vertical one. If the value of h is kept constant and f increases from 0.5 to 0.95 the lower vertex of the hyperbola rises while the hyperbola increases its curvature and reduces its width as shown in *Figure 1-12*.

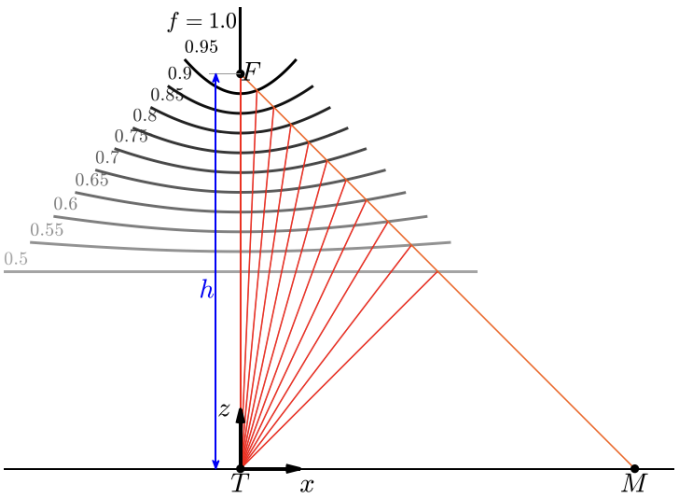

Figure 1-12 Effect of f on the shape of the hyperbola when h is kept constant [6].

2 Methodology

The aim of this thesis is to develop a model to evaluate the performance of a BDLFR system when coupled with a heat requiring process and to determine an optimal configuration of the system in terms of geometrical parameters.

To this end, two models have been developed:

- Ideal model of BDLFR systems
- Non-ideal model of BDLFR systems
- Simplified thermal model of BDLFR systems

The ideal model for BDLFR systems has been developed in Matlab and based on the work published by Sanchez-Gonzalez A and Gomez-Hernandez J "Beam-Down linear Fresnel reflector: BDLFR" [6]. From this paper have been taken the tracking equations to determine the correct orientation of the field mirrors, the effect of the main geometric parameters, the method to compute the absorber width accounting for the sunshape and the principles to determine the mirror spacing that optimizes optical efficiency at noon. Furthermore, it will be used to estimate the optical efficiency of the system in absence of optical errors to determine the main sources of optical loss.

The non-ideal model for BDLFR systems has been developed in SolTrace and used to estimate more accurately the instantaneous, daily and annual optical efficiency of the system, especially in the presence of optical errors and mirror reflectivity. To this end, this model has been used to determine the incidence angle modifiers curves of the system and consequently its power output for every possible position of the sun.

The thermal model is a Matlab code that evaluates the radiative losses towards the environment of the absorber once the power output of the system is known. It allows to compute the thermal and consequently the global efficiency of the system.

The interaction between the different models is shown in Figure 2-1.

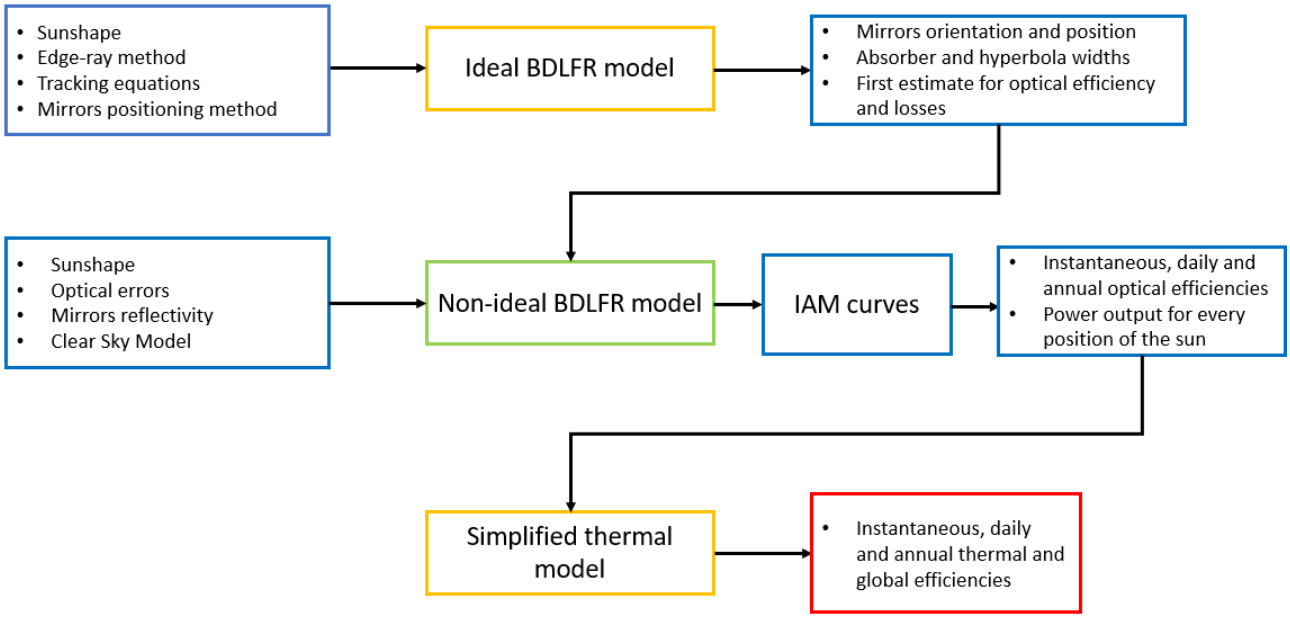

Figure 2-1 Interaction between the three models.

2.1 Main performance indicators

In Figure 2-1 some of the most important performance parameters are mentioned. Instantaneous optical, thermal and global efficiencies are defined as:

$$\eta_{opt} = \frac{P_{abs}}{P_{id}} \tag{2.1}$$

$$\eta_{th} = \frac{P_{abs} - \dot{Q}_{loss}}{P_{abs}} = \frac{P_u}{P_{abs}} \tag{2.2}$$

$$\eta_g = \eta_{opt}\eta_{th} = \frac{P_u}{P_{id}} \tag{2.3}$$

where P_{abs} is the real power impinging on the absorber, P_{id} the ideal power impinging on the mirrors without any kind of loss and P_u is the power available and used by the pyrolysis process.

2.2 SolTrace

As already underlined, the main simulation tools used in this thesis are Matlab and SolTrace. The first is used to create the geometry of the system and simulate the performance of the system once the optical efficiency is provided by the SolTrace simulation.

SolTrace is a software tool developed by NREL to model concentrating solar power optical systems and analyse their performance [8].
It uses a Monte Carlo ray tracing method to determine the exact path of a user-defined number of rays throughout the defined optical system.
The source of the rays is the sun, characterized by its position and by its sunshape. The position of the sun can be defined either in reference to the global reference system or by specifying the day, hour and latitude of the location.
The system can be divided in different stages, each with its own reference system with respect to the global one.
Each stage is comprised of one or more elements. Every element is defined by its position with respect to the reference system of the stage, an aim point, a surface shape, an aperture and a set of optical properties regarding its coefficients of reflectivity, transmissivity and absorptivity and the presence of optical errors. Two types of errors are defined: slope and specularity errors. The first accounts for macro irregularities in the mirror shape, the second for the roughness of the material.
The tracing method consists in generating rays randomly until the required number of interactions with the first stage is achieved. Then the rays are traced through the first stage and, once they leave it, though the second and so on.

Together with a user-friendly interface that allows to manually input the necessary data in the software, SolTrace is coupled with a LK engine, permitting the writing of scripts to be executed by the software thanks to a series of functions that allow the interaction between the engine and SolTrace itself.

3 Ideal BDLFR model

The ideal BDLFR model doesn't account for the optical errors introduced by the different stages of reflection. The only error considered is the one introduced by the sunshape. The goal of this model is to define the main geometric parameters of the system such as mirror positioning and orientation, width of hyperbolic cylinder and absorber and help give guidelines to select an optimal configuration.

This model is comprised of different sections: definition of the tracking equations, edge ray method, mirror spacing logic and the introduction of a CPC.

3.1 Tracking equations

Tracking equations aim to find the correct inclination of the mirrors so that a ray, reflected off the mirror centre and then off the BD reflector, will end exactly on the secondary focus (i.e., y-axis).
To do so we need some input parameters such as the position of the sun, the hyperbola shape factor f, the height of the primary focus point h, and the position of the mirror x_m.
The following methodology is the one used by Sánchez-González and Gómez-Hernández [1].
The position of the sun each hour of each day can be described with a unit vector $s = [s_x, s_y, s_z]$ originating in the centre of the mirror and pointing towards the centre of the sun (see Chapter 1.3).

The required reflected vector for the mirror points from the mirror centre towards the primary focus point. It can be then defined as the following unit vector:

$$r = \frac{[-x_m, F_y, h]}{\sqrt{x_m^2 + F_y^2 + h^2}} \tag{3.1}$$

where F_y can be found considering that, for the first law of reflection, the y-component of r and s must have the same module but opposite sign. It follows that:

$$F_y = -s_y \sqrt{\frac{x_m^2 + h^2}{(1 - s_y^2)}} \tag{3.2}$$

Also using the first law of reflection we can find the direction of the mirror normal as:

$$m = \frac{r + s}{|r + s|} \tag{3.3}$$

An important parameter to compute is the incidence angle ϕ_m of the sun rays on the mirror surface:

$$\cos(\phi_m) = m \cdot s = m \cdot r \tag{3.4}$$

By construction, $r_y + s_y = m_y = 0$. This suggests that, to correctly orientate the mirror, is enough to consider the projection of the main r and of the sun vector s on the transversal plane, without considering the y-component of all the vectors. The complete 3D analysis is instead useful to estimate what should be the longitudinal length of the hyperbola and receiver as to avoid any end-loss.

3.2 Edge ray method

3.2.1 Edge ray method by González-Hernández (GH edge ray method)

The sun appears in the sky as a disk of certain angular radius. This value can be obtained from the sun radius r and the sun-earth distance R:

$$\theta_{sun} = \operatorname{atan}\left(\frac{r}{R}\right) \approx \frac{r}{R} \cong 4.69\ mrad\ (0.25°) \tag{3.5}$$

A ray impinging on a point can be described as a cone with axis coincident with the main ray direction and aperture equal to θ_{sun}.

The edge ray method used by Sánchez-González and Gómez-Hernández [1] considers the three-dimensional image spread due to the lower and upper edge rays of the reflected cone originating in the mirror centre throughout the optical system, allowing to compute the correct absorber and hyperbola widths in the design condition.

The design condition considered by the authors is noon of the equinox for a latitude of 40°N.

As shown in Figure 3-1, the upper edge ray has a higher primary focus point than the ray reflected by the mirror centre while the lower edge's is lower. When their intersection points with the hyperbola are determined, by the law of reflection, it is possible to compute the direction of the rays reflected off the hyperbola and where they intersect the x-axis.

Since the further mirror row will have the highest image spread, the final size of the absorber aperture will be computed on this mirror. All the other mirror rows will have smaller spot sizes and so the spillage losses, at least in the design condition, are minimized.

It is worth mentioning that the image spread so described takes place in the plane containing the main reflected rays and not in the transversal plane as it would appear from *Figure 3-1*.

Given the last mirror position x_{last}, the shape factor of the hyperbola f, the primary focus point height h and using the tracking equations, the following can be said:

$$r_{last} = \frac{\left[-x_{last}\ , F_{y\ last}\ , h\right]}{\sqrt{x_{last}^2 + F_{y\ last}^2 + h^2}} \tag{3.6}$$

will be the main reflected vector of the last mirror (centre point).

$$m_{last} = \frac{r_{last} + s}{|r_{last} + s\,|} \tag{3.7}$$

$$\cos(\phi_{m\_last}) = r_{last} \cdot m_{last} \tag{3.8}$$

$$\phi_{m\_last} = \text{acos}(\cos(\phi_{m\_last})) \tag{3.9}$$

If we compute the slant range as:

$$d = \sqrt{x_{last}^2 + F_{y\,last}^2 + h^2} \tag{3.10}$$

then the variation in primary focus point height of the upper (+) and lower (-) edge ray can be computed using the law of sines:

$$dh_+ = d * \sin(\theta_{sun}) / \sin(\frac{\pi}{2} - \varepsilon_r - \theta_{sun}) \tag{3.11}$$

$$dh_- = d * \sin(\theta_{sun}) / \sin(\frac{\pi}{2} + \varepsilon_r - \theta_{sun}) \tag{3.12}$$

where ε_r is the elevation angle of the main reflected ray computed as the angle between the main reflected ray and its projection on the xy-plane.

and the upper edge ray primary focus height as:

$$h_\pm = h \pm dh_\pm \tag{3.13}$$

At this point we can determine the upper edge ray vector as:

$$r_\pm = \frac{[-x_{last}\,, F_{y\,last}\,, h_\pm]}{\sqrt{x_{last}^2 + F_{y\,last}^2 + h_\pm^2}} \tag{3.14}$$

To compute the hyperbola width, the point of intersection between the hyperbola and the lines passing through the mirror centre and having slope given by $r_\pm$ must be found.

$$\begin{cases} z = \frac{a}{b}\sqrt{x^2 + b^2} + h/2 \\ z = -\frac{h_\pm}{x_{last}}(x - x_{last}) \end{cases} \tag{3.15}$$

The solution is given by a second-grade equation in x whose coefficients are:

$$\alpha_{\pm} = \left(\frac{h_{\pm}}{x_{last}}\right)^2 - \left(\frac{a}{b}\right)^2 \tag{3.16}$$

$$\beta_{\pm} = -\frac{h_{\pm}(h_{\pm} \pm dh_{\pm})}{x_{last}} \tag{3.17}$$

$$\gamma_{\pm} = \left(\frac{h_{\pm} \pm dh_{\pm}}{2}\right)^2 - a^2 \tag{3.18}$$

The coordinates of the intersection point are given by $I_{\pm} = \left[I_{\pm}^{x}, I_{\pm}^{y} I_{\pm}^{z}\right]$ where:

$$I_{\pm}^{x} = \frac{-\beta_{\pm} - sgn(x_{last})\sqrt{{\beta_{\pm}}^2 - 4\alpha_{\pm}\gamma_{\pm}}}{2\alpha_{\pm}} \tag{3.19}$$

$$I_{\pm}^{y} = F_{y\,last}\left(1 - \frac{I_{\pm}^{x}}{x_{last}}\right) \tag{3.20}$$

$$I_{\pm}^{z} = h_{\pm}\left(1 - \frac{I_{\pm}^{x}}{x_{last}}\right) \tag{3.21}$$

The width of the hyperbola is $w_{hyp} = 2I_{+}^{x}$.

To determine the direction of the normal to the hyperbolic cylinder in the intersection points of the upper and lower edge rays the derivative in these points is computed as:

$$d_{hyp\pm} = \frac{aI_{\pm}^{x}}{b\sqrt{I_{\pm}^{x\,2} + b^2}} \tag{3.22}$$

The direction of the normal to the hyperbola surface is determined consequently considering that the secondary reflector is a hyperbolic cylinder and therefore the y-component of its normal is equal to 0 in every point.

$$n_{\pm} = \frac{\left[d_{hyp\,\pm}, 0, -1\right]}{\sqrt{d_{hyp\pm}^2 + 1}} \tag{3.23}$$

Now that the normal to the hyperbola is known, the direction of the reflected rays is determined using the law of reflection:

$$t_{\pm} = r_{\pm} + 2n_{\pm}\cos\phi_{hyp\,\pm} \tag{3.24}$$

where:

$$\cos\phi_{hyp\,\pm} = -r_{\pm}\cdot n_{\pm} \tag{3.25}$$

The intersection of the rays reflected off the hyperbola with the x-axis is the point $T_{\pm} = \left[T_{\pm}^{x}, T_{\pm}^{y}, 0\right]$ where:

$$T_{\pm}^{x} = I_{\pm}^{x} - \frac{t_{\pm}^{x}}{t_{\pm}^{z}} I_{\pm}^{z} \tag{3.26}$$

$$T_{\pm}^{y} = I_{\pm}^{y} - \frac{t_{\pm}^{y}}{t_{\pm}^{z}} I_{\pm}^{z} \tag{3.27}$$

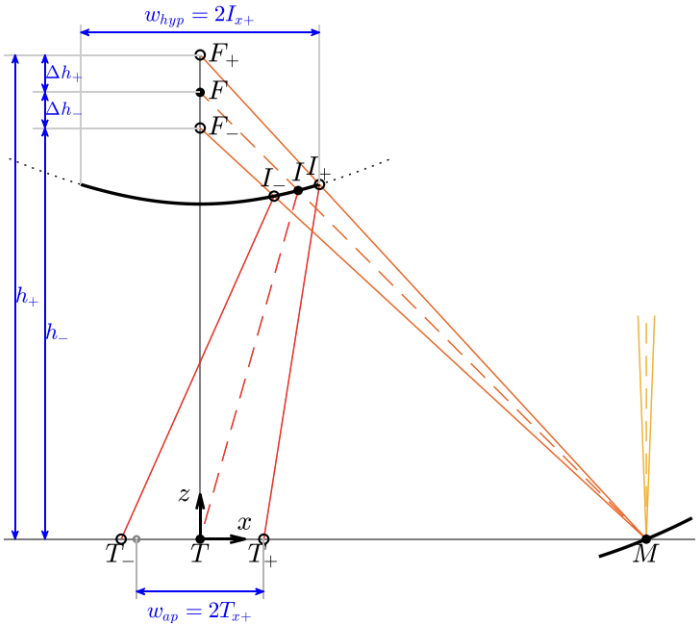

Figure 3-1 Absorber and hyperbola width defined with the edge ray method [6].

The absorber width is then computed as:

$$w_{abs} = 2T_{+}^{x} \tag{3.28}$$

From Figure 3-1, it can be understood that $|T_{-}^{x}| > |T_{+}^{x}|$ is always true. However, the amount of radiation lost because of how the absorber width is computed (using T_{+}^{x} instead of T_{-}^{x}) is rather small, lower than 5%, and so the criteria holds as it is also shown by the Soltrace simulation.

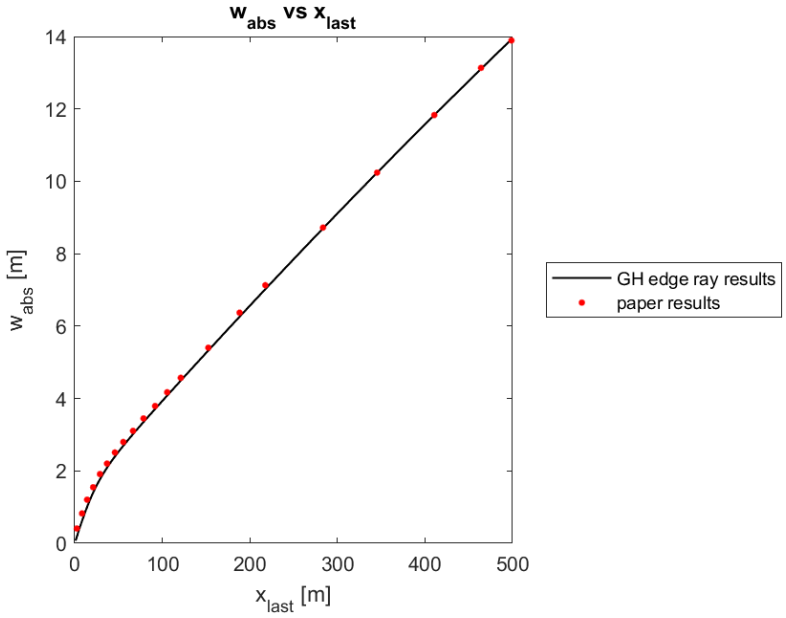

Figure 3-2 Absorber width as a function of the position of the last mirror row according to the GH edge ray method (f=0.8, h=50).

Considering the results in Figure 3-2, the absorber width tends to become null as the distance of the last mirror row approaches zero. In Figure 3-3 the position of the last mirror row is set to virtually 0 (x_{last} can't be equal to zero as it is at the denominator in some equations). As shown in Figure 3-3 (a), the three-dimensional method here described correctly represents the path of the upper and lower edge rays in the longitudinal plane. From Figure 3-3 (b) instead, it can be deduced that the method doesn't account for the real 3D image spread of the cone, producing an absorber width that tends to 0. As it will be analysed in the next chapters, this error only occurs when the mirror is relatively close to the z-axis. However, since this error regards mirror positions of actual practical interest, an alternative edge ray method has been developed.

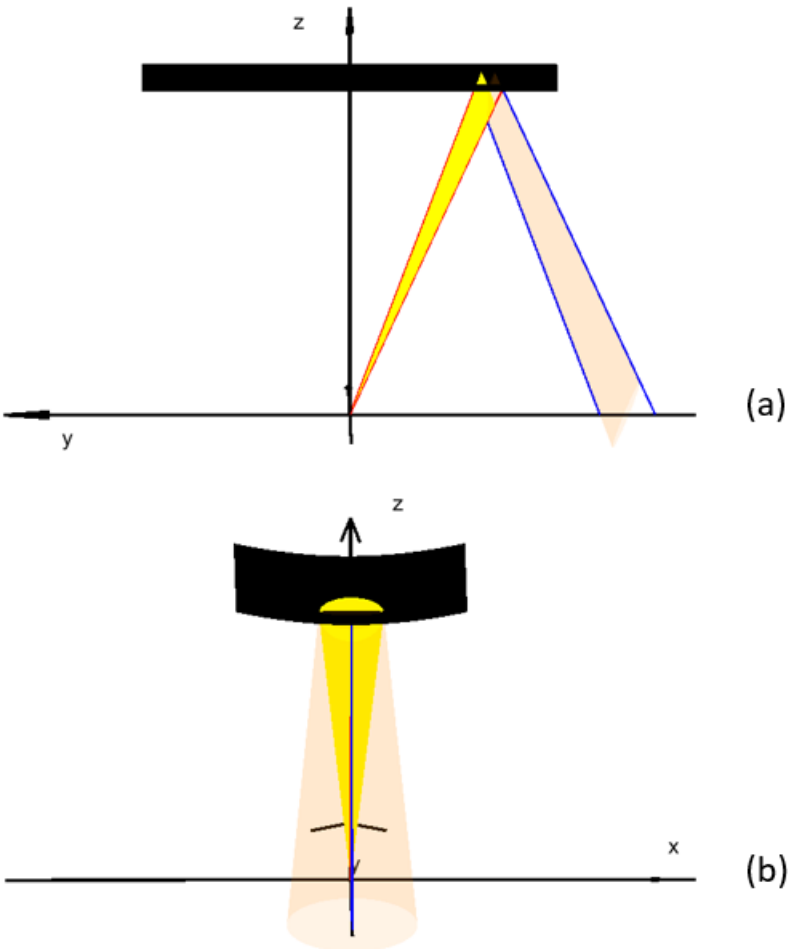

Figure 3-3 Reflection of the solar cone impinging on the centre of a mirror positioned in the centre of the reference system (x_m=0, h=10, f=0.8).

3.2.2 2D edge ray method

To overcome the limits of the edge ray method as proposed by Sánchez-González and Gómez-Hernández, a two-dimensional edge ray method is developed.

This method considers the projection of the solar cone impinging on the centre of the last mirror on the transversal plane and to then apply the same method evidenced in the three-dimensional method.

Considering that the design condition is the one previously defined (noon of the equinox at a latitude of 40°N), the width of the projected cone σ_{sun}, shown in Figure 3-4, can be computed as:

$$\sigma_{sun} = \frac{\theta_{sun}}{\cos(\theta_i)} = \frac{\theta_{sun}}{\cos(L)} = \frac{0.00469}{\cos(40)} = 0.006122\ rad \tag{3.29}$$

The equivalence between the angle θ_i and the value of the latitude is given by the design condition chosen.

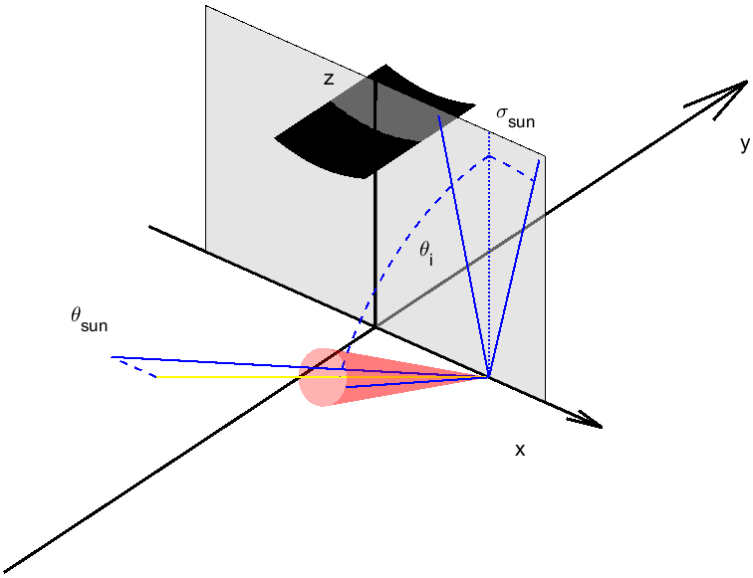

Figure 3-4 Projection of the solar cone on the transversal plane.

The main concept of the edge ray method is the same of the three-dimensional one but everything is computed on the transversal plane.

The sun vector, projected on the transversal plane at solar noon, is $s = [0,1]$.

The reflected ray off the last mirror instead is computed as:

$$r_{last} = \frac{[-x_{last}, h]}{\sqrt{x_{last}^2 + h^2}} \tag{3.30}$$

From the law of reflection, the mirror normal is:

$$m_{last} = \frac{r_{last} + s}{|r_{last} + s|} \tag{3.31}$$

Similarly to before, the incidence angle of the mirror is computed as:

$$\cos(\phi_{m_{last}}) = r_{last} \cdot m_{last} \tag{3.32}$$

$$\phi_{m_{last}} = \text{acos}(\cos(\phi_{m_{last}})) \tag{3.33}$$

The slant range d and the elevation angle of the reflected ray ε_r must be projected as well. It follows that:

$$d = \sqrt{x_{last}^2 + h^2} \tag{3.34}$$

$$\varepsilon_r = \frac{\pi}{2} - 2\phi_{m_{last}} \tag{3.35}$$

The variation in primary focus height of the upper and lower edge ray are now evaluated with the law of sines:

$$dh_+ = \frac{d \sin(\sigma_s)}{\sin\left(\frac{\pi}{2} - \varepsilon_r - \sigma_{sun}\right)} \tag{3.36}$$

$$dh_{-} = \frac{d\sin(\sigma_s)}{\sin\left(\frac{\pi}{2} + \varepsilon_r - \sigma_{sun}\right)} \tag{3.37}$$

From this point on, the two methods are analogous with the only difference that here all the y-components of vectors and intersection points are null.

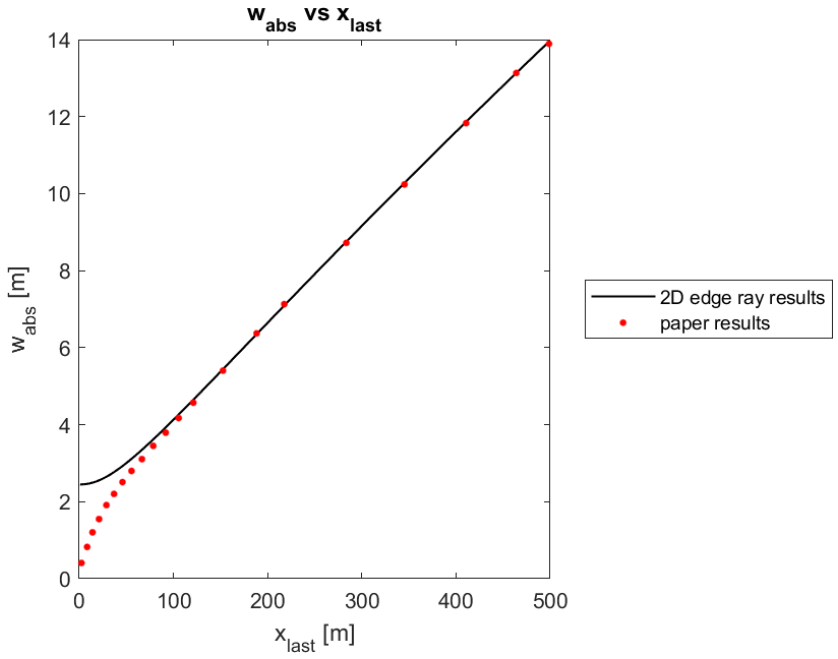

Figure 3-5 Absorber width as a function of the position of the last mirror row according to the 2D edge ray method (f=0.8, h=50).

From Figure 3-5 it can be observed that, for last mirror positions lower than 100 meters, the 2D edge ray method's results differ considerably from the ones reported in the paper.

3.2.3 Validation of GH and 2D edge ray method

A validation of the edge ray methods has been performed through a series of Soltrace simulations. The basic principle of the validation is to recreate the cone of light that leaves the centre of the last mirror row, hits first the hyperbola and then the absorber and then measure the width of the resulting ellipsis at ground level.

In these simulations the input sunshape for SolTrace is as a pillbox of semi-angular width equal to $\theta_{sun} = 0.00469\ rad$ and the sun vector is the one obtained at design point.

To simulate the effect of a cone originating from a point, the first stage of the simulation is a single small parabolic mirror put at a progressively increasing distance from the z-axis, while the centre is located on the x-axis, so that all the required rays are projected by the software on its surface alone.

The second and third stage consist of the hyperbola and the absorber, both wide enough to avoid any spillage in the transversal direction and long enough in the longitudinal one to avoid end-losses.

After tracing, the measured absorber width is computed consistently with the edge ray method logic of considering the minimum between two distances shown in Figure 3-6, T_{-}^{x} and T_{+}^{x}. T_{-}^{x} represents the

outermost ray intersection on the absorber in the half-plane of negative x-axis values, T_+^x the same but for the positive ones (in these simulations the sun rays come from this last direction). This becomes particularly important when the distance of the mirror from the centre of the system increases because, as shown in Figure 3-6, the pattern of intersections tends to elongate and become asymmetrical with respect to the y-axis. This is due to the elliptical shape of the image projected on the absorber.

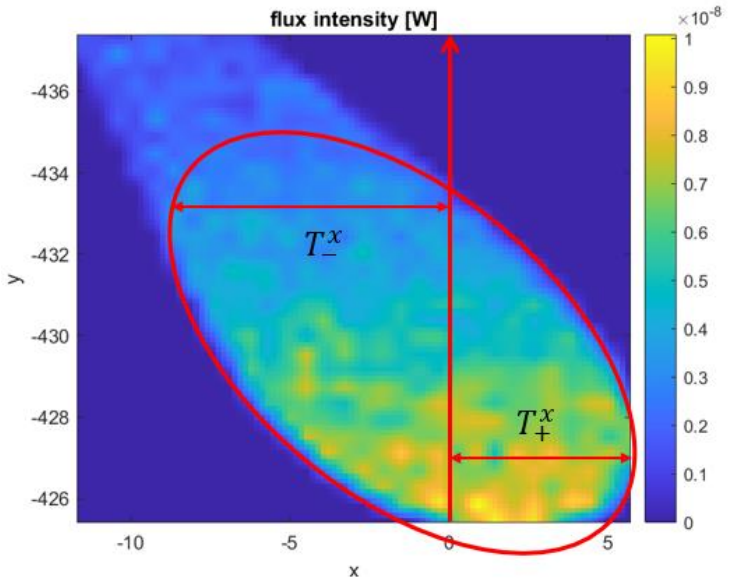

Figure 3-6 Spot size of the infinitesimal parabolic mirror.

The absorber width computed with this method is $w_{abs}^{ray\ tracing} = 2T_+^x$, in analogy to what is done with the edge ray method.

The values of absorber width obtained with this method are evaluated against the values resulting from the edge ray methods, for values of x values ranging from 0 to 500.

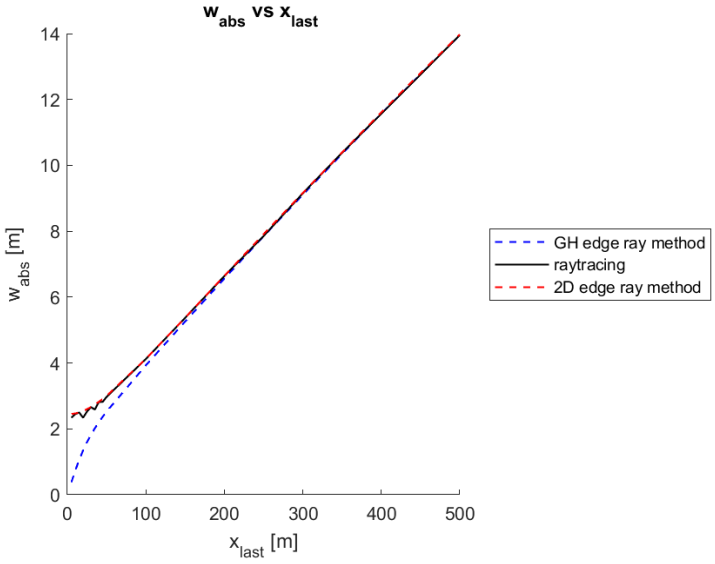

Figure 3-7 absorber width computed with edge ray method and with raytracing.

The 2D edge ray method approximates very well the real absorber width required according to the SolTrace simulation for all the value of last mirror position while the GH method fails in the region for x_{last} smaller

than 100 meters, as previously noticed. The difference between the 2D edge ray method and the raytracing method, evaluated as $\Delta w_{abs} = \frac{w_{abs}^{edge-ray} - w_{abs}^{raytracing}}{w_{abs}^{raytracing}} * 100$, is almost always less than 1% except for small values of x_{last} where the ray tracing method experiences some irregularities that, however, don't change the general trend of the curve.

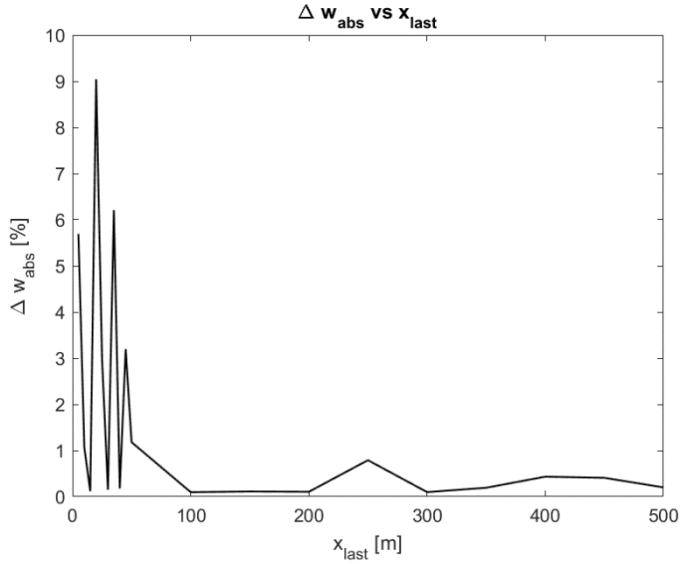

Figure 3-8 Percentage difference between the raytracing absorber width and the 2D edge ray method.

It is interesting to evaluate how much of the power impinging on the mirror would spill if in these simulations the absorber width would be set at the value estimated by the 2D edge ray method. The interception efficiency of the absorber is defined as:

$$\eta_{intercept} = \frac{P_{on\ absorber}}{P_{on\ mirror}} \tag{3.38}$$

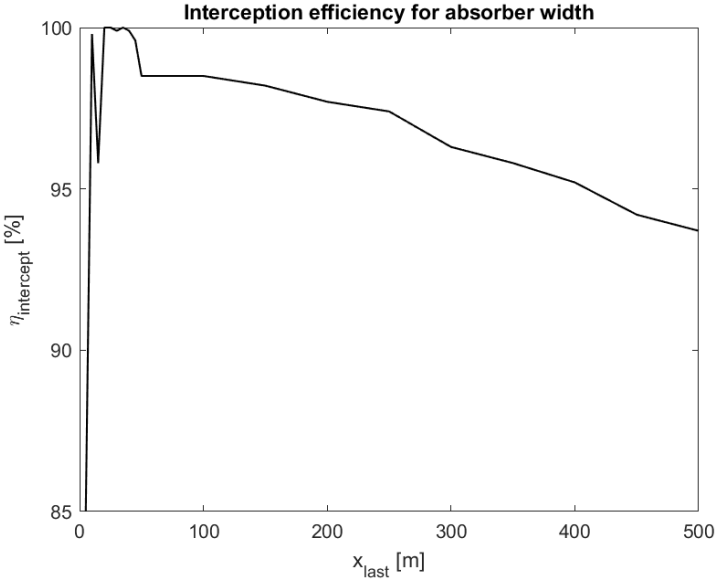

Figure 3-9 Interception efficiency for the absorber width computed with 2D edge ray method.

If the last mirror is less distant than 450 meters (a distance well beyond the state of the art for LFR systems) the interception efficiency is greater than 95%. For the range of configurations afterwards analysed the last mirror row will not be further away than 100 m, making the 2D edge ray method a valid approximation for the computation of the absorber width. The intercept factor is lower than one because the image projected on the absorber is an asymmetrical ellipse (asymmetrical with respect to the y-axis). As the mirror moves away from the z-axis, the asymmetricity of the ellipse increases and it will determine a lower intercept factor on a y-axis symmetrical absorber.

3.3 Mirror spacing for blocking avoidance

In the work by Sánchez-González et al. [6] is suggested a mirror spacing that avoids blocking at noon of the design point. Two criteria must be followed to achieve this configuration: avoidance of blocking by the previous mirror row and coordinate of the first mirror row is so that clears the space for the absorber on the ground.

The position of the first mirror is set by default at 1.5 time the width of the mirror ($x_1 = 1.5\, w_m$). The position of the second mirror is found through an iterative procedure: a first guess value for x_2 is set at a distance equal to the mirror width to avoid intersections between the two mirror rows and allow them to rotate completely around their longitudinal axis ($x_2^I = x_1 + w_m$). At this point a check for blocking is required (Chapter 3.1). If blocking is detected, then the second mirror row is moved away from the z-axis ($x_2^{II} = x_2^I + \delta$) and the process repeated until no blocking is found. Once the position of the second mirror row is determined, the position of the third can be found with the same process using as starting point $x_3^I = x_2 + w_m$.

This iterative method is necessary because the presence of blocking is related to both the mirror position and the mirror normal which, in turn, is function of the mirror position. It follows that no closed analytic form can be written to determine the position of mirror $i + 1$ once the position of mirror i is known. However, this procedure can be rendered very precise by adopting a small δ, so that even if the ray reflected off the lower rim of mirror $i + 1$ doesn't pass through the upper rim of mirror i, the error made is negligible.

Some assumptions are necessary to use this procedure: firstly, the mirror surfaces are considered as flat in shape, when it comes to establish where the upper and lower rim of a mirror are; secondly the mirrors reflect all the rays towards the primary focus point, ignoring any aberration effects.

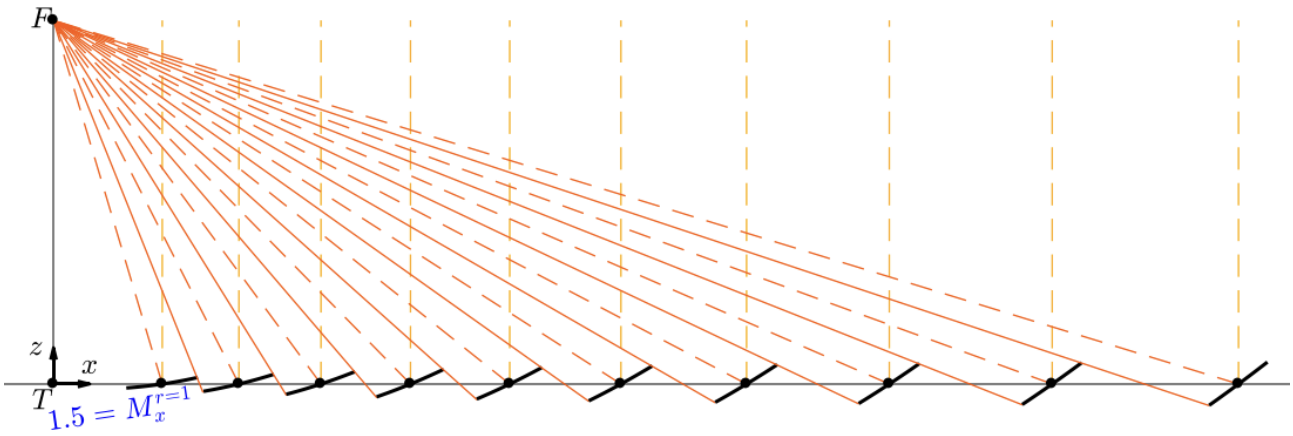

Figure 3-10 Mirror spacing for blocking avoidance [6].

Once all the position of all the mirror row has been determined, the width of the absorber is computed and interference between the first mirror row and the absorber must be checked. If such interference is found, the first mirror row must be moved to the first available position in the set $[2.5\ w_m, 3.5\ w_m, 4.5\ w_m, 5.5\ w_m, \dots.]$ and then restart the entire process since the position of the first mirror row impacts on the position of all the following ones.

In Figure 3-11, the number of the mirror row is plotted against the position of that mirror row for different primary focus heights. The result obtained from the previous procedure are plotted and compared with the results reported by Sánchez-González et al.

It is interesting to notice how the space between two mirror row increases as the number of row increases.

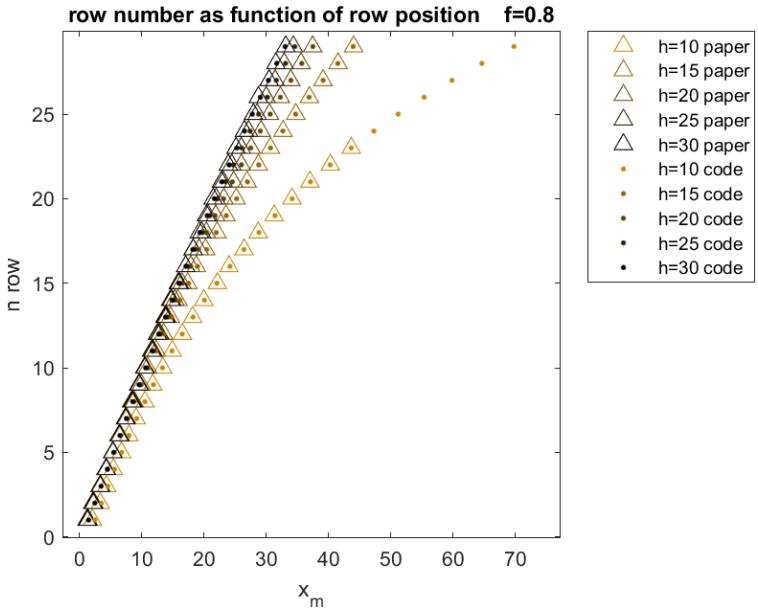

Figure 3-11 Mirror row number vs row position for different primary focus points heights.

From this point on, this particular spacing will be referred to as noon-optimized spacing.

3.4 Effects of the different geometrical parameters on w_{abs}

A number of relevant geometrical parameters have been introduced in the previous chapters such as number of mirror rows, hyperbola shape factor and primary focus height. It is of interest to observe the effect that these parameters have on the width of the absorber and to find, if possible, the best possible configuration that minimized the w_{abs}, since this would also imply the minimum radiative losses to the environment.

3.4.1 Absorber width as function of primary focus height

Firstly, it can be observed that, for a fixed value of f,the value of the absorber width reaches a minimum for a certain primary focus height (Figure 3-12). The curves are reported for different numbers of rows N_r ($N_r = N_m/2$).

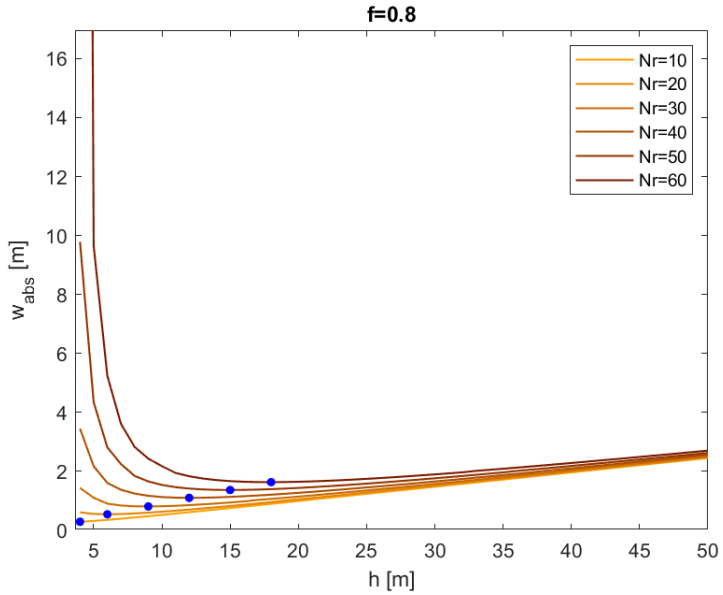

Figure 3-12 Absorber width as a function of primary focus point height.

In each w_{abs}-h curve, a value of h can be found that minimizes the absorber width.

The presence of such minimum can be better understood considering the results reported in Table 3-1.

	$\mathbf{h < h_{opt}}$	$\mathbf{h = h_{opt}}$	$\mathbf{h > h_{opt}}$
$\mathbf{h\ [m]}$	5	9	33
$\mathbf{x_{last}\ [m]}$	37.68	20.764	16.213
image size on hyperbola [m]	0.714	0.3286	0.3793
$\mathbf{i.s. increase\ hyperbola - absorber}$	1.6745	2.5608	4.5511

final image size [m]	1.1956	0.8415	1.7262
$\mathbf{w_{abs}}$ **[m]**	1.1046	0.8108	1.7117

Table 3-1 Image size increase for different values of h considering f=0.8 and Nr=30.

For different values of primary focus height, the position of the last mirror row, the image size on the hyperbola and the increase of the image size through the reflection from hyperbola to absorber are shown.

The image size on the hyperbola is computed as the distance between the points I_+ and I_- highlighted in Figure 3-1 Absorber and hyperbola width defined with the edge ray method [6]. ($image\ size\ on\ hyperbola = \overline{I_+I_-}$). Similarly the increase in image size due to the reflection on the hyperbola is defined as the ratio between the distance between T_+ and T_- and the image size on the hyperbola ($image\ size\ increase\ hyperbola - absorber = \frac{\overline{T_+T_-}}{\overline{I_+I_-}}$). The final image size is the product of the first two quantities and, therefore corresponding to the distance $\overline{T_+T_-}$.

The previously mentioned influence of h on the field size can be recognized in the position of the last mirror row: as h increases from values below the optimal height to values well above, the last mirror row (and consequently the rest of the mirror field) moves closer to the origin of the x-axis.

The image spread on the hyperbola is minimum for the configuration for optimized h. In the configuration $h < h_{opt}$ this value is more than double the one with optimal h due to the long distance of the last mirror row from the hyperbola that allows the image size to grow. In the case of $h > h_{opt}$ instead, even if the last mirror is close to the x-axis origin, the distance from the hyperbola is greater than the optimal h as the primary focus height increase effect on the image size overcomes the one of reduction due to the approaching of the last mirror row.

As for the increase in image size due to the reflection, the configuration with $h < h_{opt}$ is the one that increases the least the size of the image because of the small distance that the edge rays have to cover to reach the ground. This distance will be the maximum for the case $h > h_{opt}$ and so it will be the image size increase.

Overall, the configuration $h = h_{opt}$ creates the minimum spot size on the ground after the series of reflections, which also translates into a smaller absorber width.

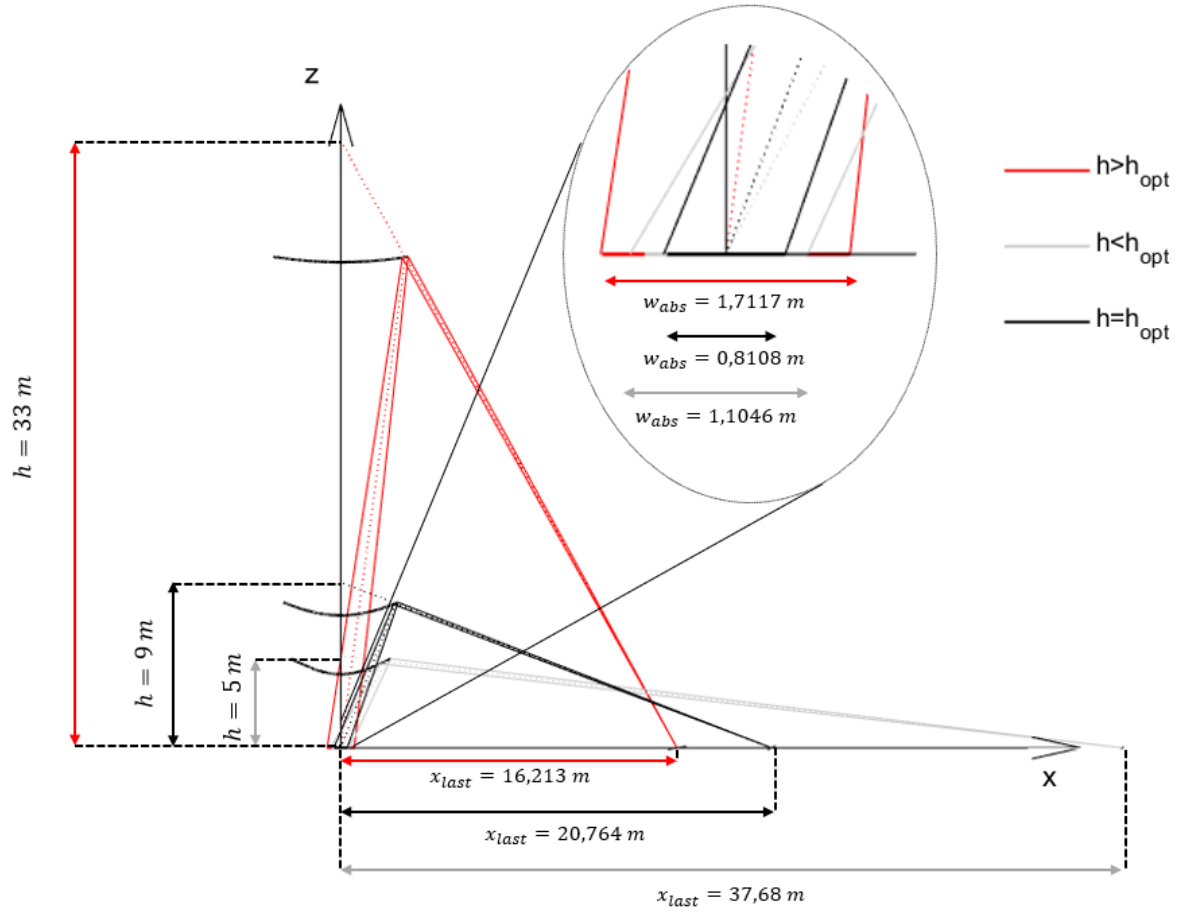

Figure 3-13 Change of layout moving along a w_{abs}-h curve for a constant number of rows and hyperbola shape factor (Nr=30, f=0.8).

Figure 3-13 shows the difference in system layout for the three points analysed in *Table 3-1*.

3.4.2 Minimum absorber width curves

The values of h, for every number of N_r, found in the previous paragraph that minimize the absorber width, and the resulting w_{abs} and w_{hyp} can be plotted against the number of rows for which they have been obtained.

In the results shown in Figure 3-14 through Figure 3-16, all quantities present linear trends. The behaviour of h_{opt} with respect to the number of rows is explained referencing to what has been said while commenting Table 3-1: as N_r increases the last mirror row will move further away from the x-axis origin and if h were to remain the same, the configuration would fall in the case $h < h_{opt}$. The effect of f on h_{opt} (the second decreases as the first increases considering the same number of mirror rows) can be explained considering that the higher the hyperbola shape factor, the higher is the magnification effect of the hyperbola, causing smaller h to be preferred to mitigate this effect.

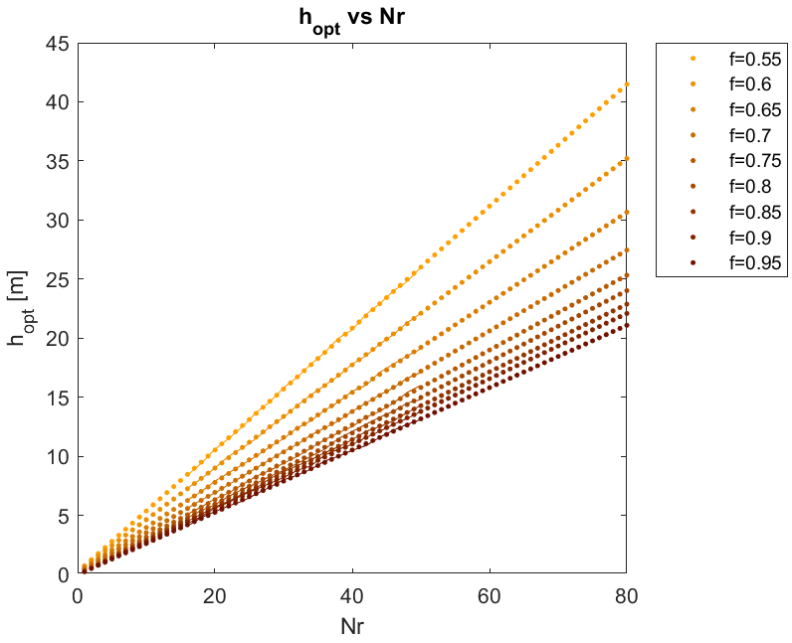

Figure 3-14 Optimal primary focus height as a function of the number of rows for different values of f.

This can also be noticed looking at the results shown in Figure 3-15 by fixing the number of rows. The value of $w_{abs\ opt}$ increases with N_r as the last mirror rows moves away from the x-axis origin, generating a bigger spot size both on the hyperbola and on the ground even if the primary focus height increases.

The same explanation can be used to justify the behaviour of $w_{hyp\ opt}$ with N_r. The effect of the hyperbola shape factor is best explained by looking at Figure 1-12. It is clear that as f increases the hyperbola width decreases and is set close to the primary focus point: the cone defined by the edge rays "cut" the hyperbola later and closer to its vertex, reducing the needed width.

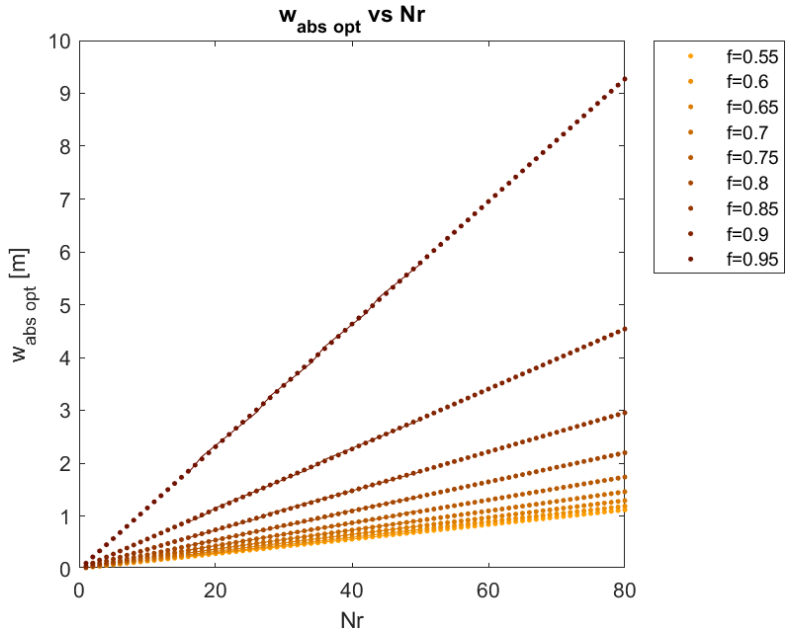

Figure 3-15 Optimal absorber width as a function of the number of rows for different values of f.

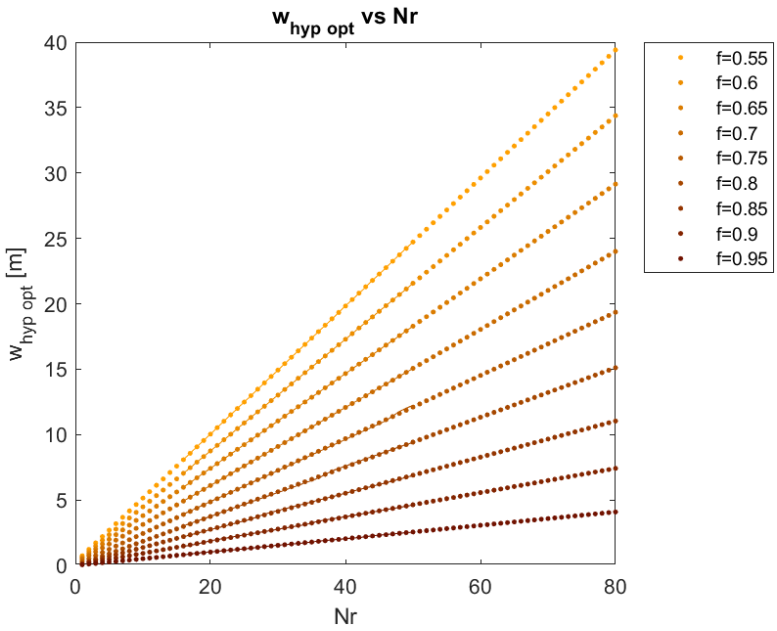

Figure 3-16 Optimal hyperbola width as a function of the number of rows for different values of f.

The change in layout geometry, moving along a $h - N_r$ curve at constant f factor in *Figure 3-14* is shown in *Figure 3-17*. The system configurations shown in this picture are realised for the same hyperbola shape factor so the shape of the hyperbola remains the same but the component rises as the primary focus point height is increases with the number of mirror rows. This fact, coupled with the increase of distance of the last mirror row (since the number of rows increases), result in a higher absorber width.

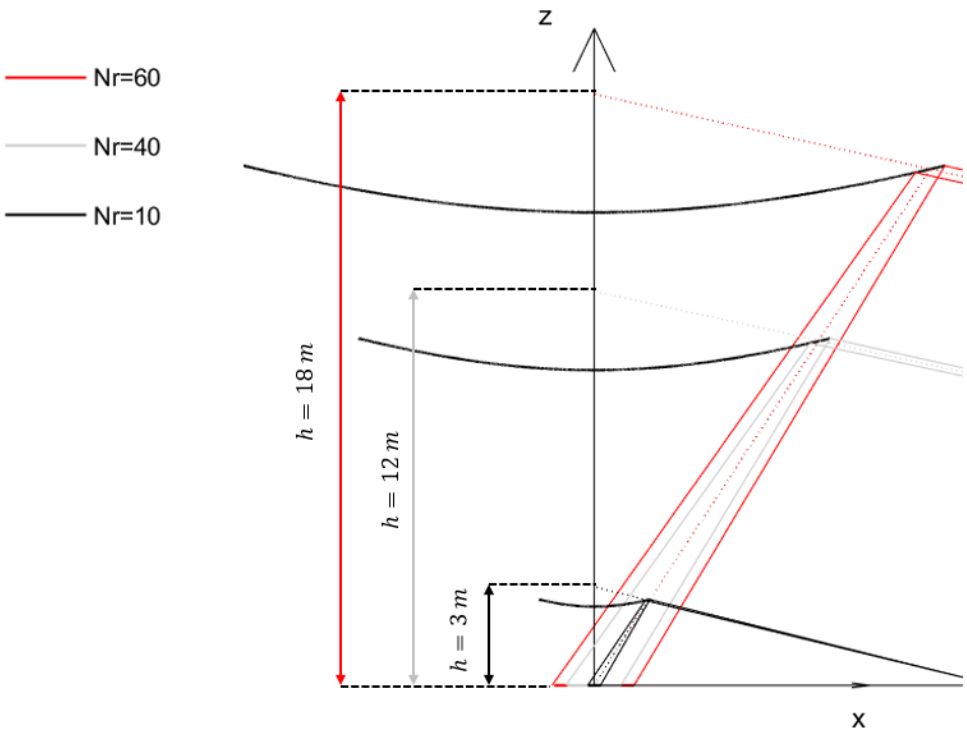

Figure 3-17 Change of system geometry moving along a h-Nr line with constant f factor (f=0.8).

The choice of an optimal configuration that minimizes radiative heat losses to the environment would fall on the configuration with the smaller absorber width. However, considering only this aspect can be

reductive. It is necessary to size the entire system taking into consideration also the power actually conveyed on the absorber, its daily efficiency (in terms of energy conveyed on the absorber compared to the one ideally available to the mirror field) and the coupling with the pyrolysis process.

Some practical observations can however be made considering these geometrical results.

Selecting a small value of f (e.g., 0.55) and a mirror field of 40 + 40 rows the corresponding values of w_{abs}, w_{hyp} and h would be respectively 0.56, 19.84 and 20.07 m. Even if the absorber width is small and has small radiative losses, the hyperbola results very large. A large hyperbolic mirror can be difficult to both manufacture and install at the 11 m required by this configuration, also considering its longitudinal length. In the optics of reducing costs and simplifying the construction of the beam-down reflector, Taramona et al. [9] have proposed a different beam-down reflector, made of several smaller flat mirrors all installed at the same height. This system can reach peaks of 60% optical efficiency and concentration ratios of 31.

To resolve this problem, a higher value of f could be chosen (e.g., 0.9). The resulting values of w_{abs}, w_{hyp} and h would be respectively 2.28, 3.72 and 11 m. While the hyperbola would be placed at around the same height (9.9 m), its width is much more manageable. On the contrary, the width of the absorber increases by a factor of about 4. This clearly detrimental to the efficiency of the system. A possible solution mentioned by Sánchez-González and Gómez-Hernández [1] is to introduce a Compound Parabolic Collector (CPC) to reduce the absorber area and maintaining at the same time the low height and hyperbola width obtained with this configuration.

It is also worth mentioning that most LFR systems work with focus height ranging from 4 to 6 meters, while the primary focus heights reported in this analysis can reach much higher values. Higher beam-down reflectors entail higher costs for the support structure. A techno-economic analysis would probably shift the best solution towards lower values of h for this reason.

3.5 Effect of a CPC on the absorber width

As mentioned in the previous Chapter, a CPC is a useful tool for the optimization of a BDLFR system since it allows to contain the image spread caused by the hyperbola.

A CPC are non-imaging concentrators whose potential was highlighted by Winston R. [10]. These concentrators convey the radiation incoming radiation to the receiver, usually set at the bottom of the concentrator, via multiple reflections. Their core strength is the ability con correctly concentrate rays coming within a wide acceptance angle on the receiver.

CPCs generally consist of 2 branches of parabolas whose foci lie on each other's endpoint. Different kinds of absorbers are possible as shown in Figure 3-18: flat, bifacial and wedge or tubular. The fin of which the absorber is comprised of can be either one single tube or an array of them.

Especially for the first three kinds of absorber, a gap is recommended between the absorber and the concentrator so that this doesn't turn into an added fin to the absorber, increasing the area available for heat exchange of the absorber itself. This gap should be small, as to reduce the loss of radiation impinging on the absorber.

As demonstrated Rabl A. et al. [4], there is a limit to the maximum concentration ratio achievable by any solar concentrating system: an infinitely high concentration ratio would imply that once the equilibrium is

reached, the temperature of the absorber could be higher than the superficial temperature of the sun, therefore contradicting the second principle of thermodynamics.

For a CPC the thermodynamic limit on the concentration ratio for a line focus system can be analytically computed as:

$$C_{CPC}^{limit} = \frac{1}{\sin \theta_{ap}} = \frac{w_{abs}^{no\ CPC}}{w_{abs}^{CPC}} \tag{3.39}$$

where θ_{ap} is the acceptance angle of the concentrator. This is defined as the maximum angle at which the radiation can the concentrated on the absorber by the CPC. The rays that enter the concentrator with a higher angle are not conveyed on the absorber (Figure 3-19 (B)).

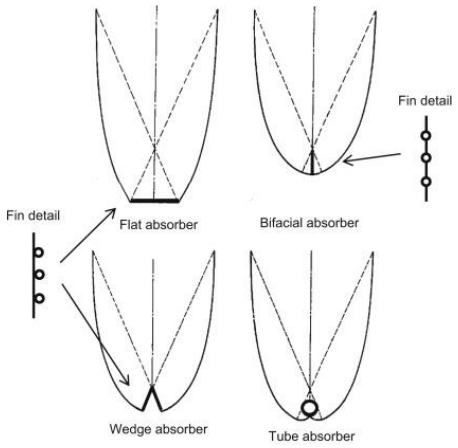

Figure 3-18 CPC absorber types [11].

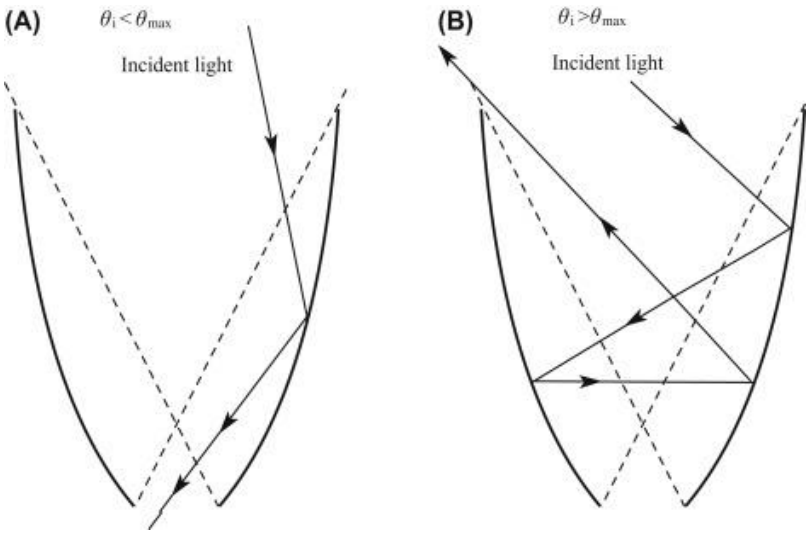

Figure 3-19 Figure A: correct reflection of ray as the incidence angle is lower than the maximum acceptance angle. Figure B: lack on conveyance to the absorber due to incidence angle greater than maximum acceptance angle. [11]

This is only one of the many sources of loss introduced by the CPC. As a real reflective element, the compound parabolic concentrator is affected by the optical errors discussed in Chapter 4.2 and by a reflectivity lower than 1. Simply applying the reflectivity to the real concentration ratio is not effective to

account for the absorption that occurs in the CPC as more than one reflection can occur before the incident ray is captured by the absorber.

For this analysis, the CPC adopted will have a flat absorber and the upper entrance will coincide with the w_{abs} computed in the previous Chapters.

The CPC considered is ideal, meaning $\rho_{CPC} = 1$, no optical errors are introduced by the component. Furthermore, every ray that hits the upper aperture of the CPC will be considered as redirected on the absorber, without considering the effects of its incidence angle.

The acceptance angle considered by Sánchez-González and Gómez-Hernández [6] is the one represented in Figure 3-20. The mathematical expression of this acceptance angle is:

$$\theta_{ap} = \tan^{-1} \frac{w_{hyp}}{2 * I_z} \tag{3.40}$$

where:

$$I_z = \frac{a}{b} \sqrt{\left(\frac{w_{hyp}}{2}\right)^2 + b^2} + c \tag{3.41}$$

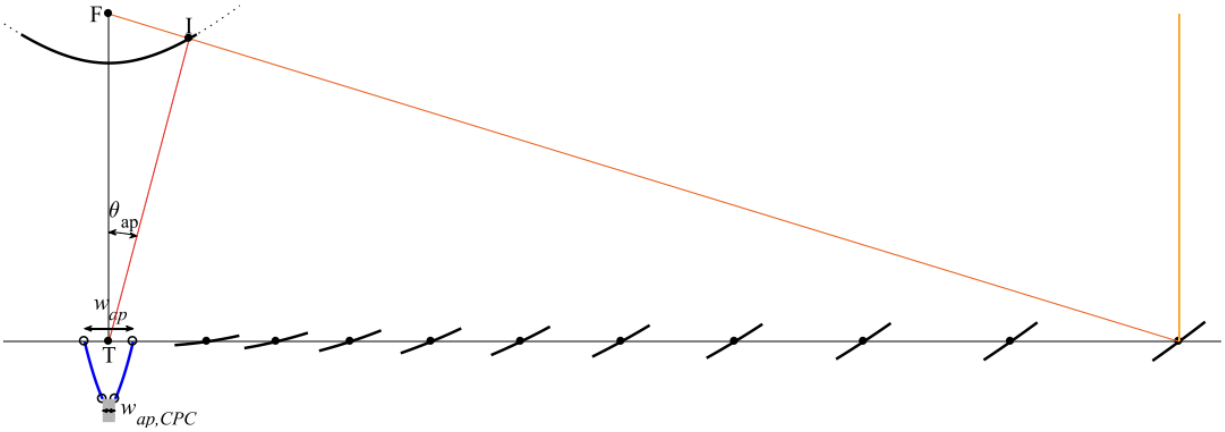

Figure 3-20 Representation of the acceptance angle as defined in [6].

For the configurations that minimize the absorber width (without the CPC) described in the previous Chapter, the concentration ratio of the CPC and the consequent absorber width are reported in Figure 3-21 and Figure 3-22.

The Concentration ratio is only a function of the hyperbola shape factor. In fact, as the acceptance angle would increase with the number of rows (since the position of the last mirror row would move further and further away from the absorber), it is kept constant by the concurrent increase of the primary focus point height (Figure 3-14). If the acceptance angle is constant, so is the concentration ratio. The highest concentration ratios are achieved by the configurations with high f since they will have a smaller w_{hyp} (Figure 3-16). As a result they will benefit more from the introduction of the compound parabolic collector than the other configurations: the difference between the absorber width lines shown in Figure 3-22 is much lower than the one shown in Figure 3-15 obtained without the CPC.

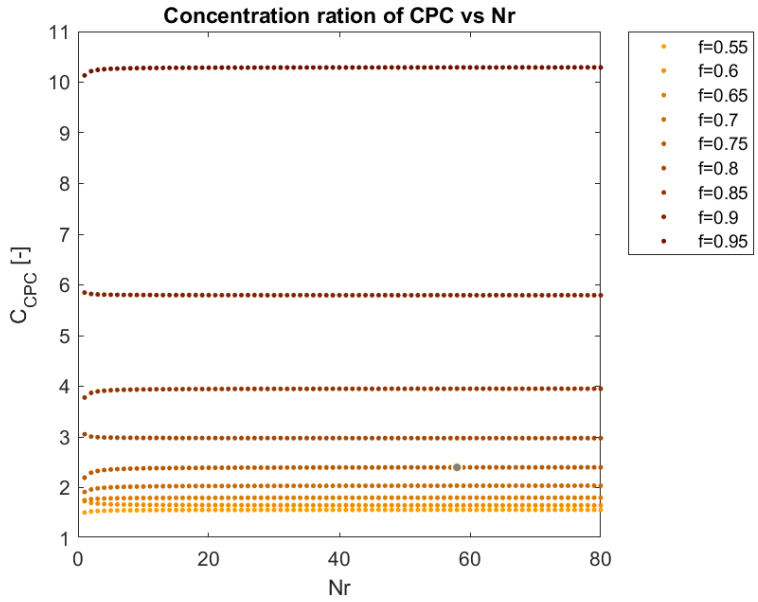

Figure 3-21 Concentration ratio for the configurations that minimized the absorber width in Chapter 3.4.2.

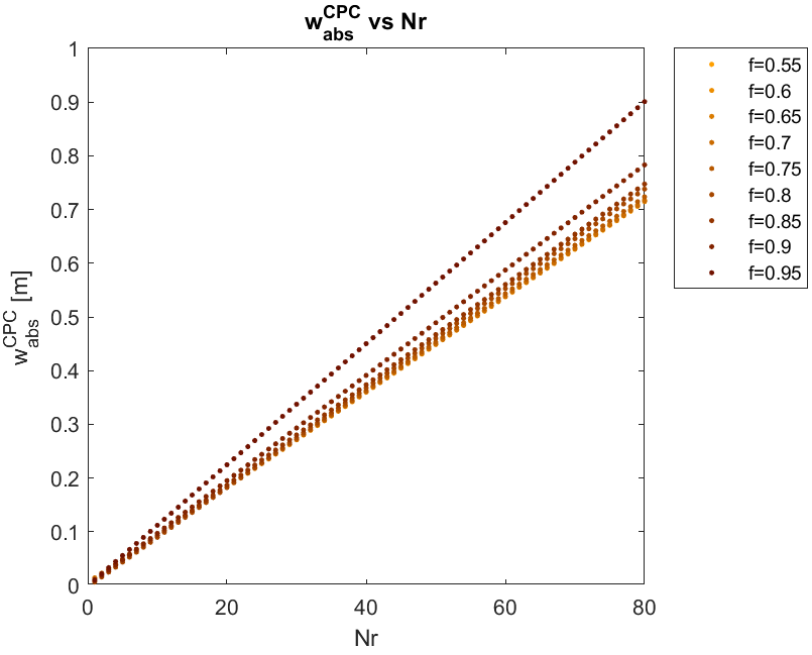

Figure 3-22 Absorber width after the application of the CPC for the configurations that minimized the absorber width in Chapter 3.4.2.

4 Non-ideal BDLFR model

The non-ideal BDLFR model uses the same geometrical mirror positioning and orientation method described in the previous Chapter but is developed in SolTrace and requires some other input parameters such as the sunshape and the definition of the different elements. The main trait of this model is the introduction of optical errors besides the sunshape and the possibility to define different focal lengths for the mirror field.

4.1 Sun definition

To function, SolTrace also requires the sun to be defined in terms of position and sunshape.

The position of the sun is defined by providing the software with a triplet of values (x, y, z) that determine a point in the global reference system. The vector connecting said point to the origin of the global reference system will be the sun vector.

SolTrace allows to determine the sunshape in three ways: as a pillbox, a Gaussian or any other user-defined shape. For this thesis, the sunshape considered will be a pillbox with halfwidth equal to $\theta_{sun} = 0.00469\ rad$ as shown in Figure 4-1.

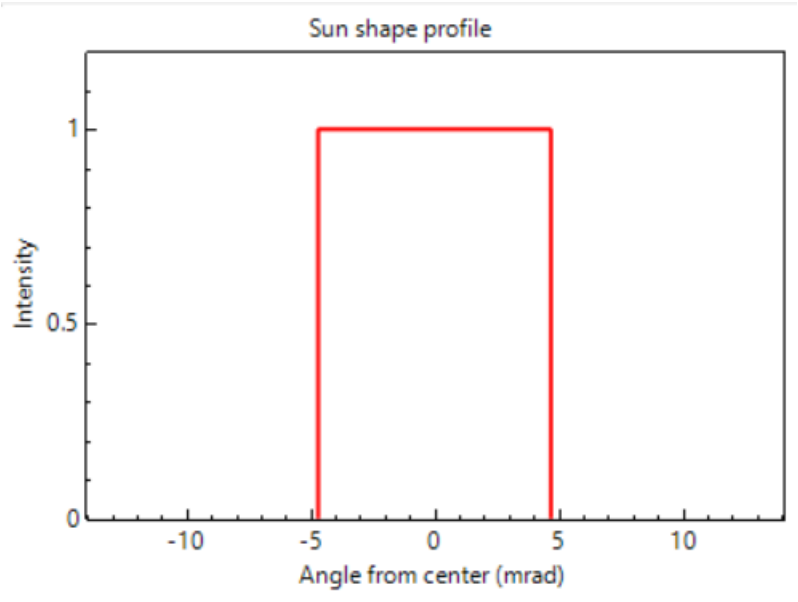

Figure 4-1 Pillbox sunshape considered.

4.2 Optics definition

The optical characteristics of the elements in SolTrace are defined by means of reflectivity, transmissivity and optical errors.

The values of reflectivity and transmissivity can be set for both front and back of the element. The value of reflectivity for the reflective side of an element is set at 0.93 while for its opaque side is set at 0. The value of the transmissivity is set at 0 for both reflective and opaque side.

The values of slope and specularity errors are based on the work by Bonanos A. (2012) [12]. The total optical error due to slope error and specularity (roughness) error is estimated to be between 1 and 3 mrad and that the specularity error is four times the slope error.

Considering that the total optical error is computed as:

$$\sigma_{optical} = \sqrt{\sigma_{spec}^2 + 4\sigma_{slope}^2} \tag{4.1}$$

The value of the specularity error can be evaluated at 0.248 mrad and the and the slope error at 0.992 mrad by assuming a total optical error equal to 2 mrad.

The chosen statistic distribution for the errors is a Gaussian of standard variation equal to σ_{spec} and σ_{slope} respectively.

4.3 Geometry definition

The SolTrace model takes as input the geometry of the system from the Matlab model, in terms of mirror position and orientation, position and shape and width of the hyperbola and width of the absorber on the ground.
The first stage is comprised of the field mirrors, the hyperbola structure and the absorber. The absorber can be put in a second stage if the analysis requires to ignore the contribution of the radiation directly impinging on the receiver. The final stage is comprised of two wide surfaces: one above the hyperbola and one below the absorber to capture every ray that doesn't intersect these two elements.
All stages' reference systems coincide with the global reference system of SolTrace.
The field mirrors are defined as parabolic elements whose focal length can be set at different values by the user. The front surface of the mirrors is the one facing upwards in the direction of the z-axis and it is the reflective one while the other is the opaque one. The aperture of the element is set equal to w_m.
The element reference system is set at a distance equal to the mirror position along the x-axis ($[x_m, 0,0]$).
The aim point is defined as:

$$[x_m + m_x, 0, m_z] \tag{4.2}$$

where x_m is the mirror position and m is its mirror normal.

The hyperbolic cylinder is divided into two parts: the one on the right of the z-axis is realised as a spline interpolation of 10 couples of points $[x_{hyp}, z_{hyp}]$ (where z_{hyp} is the value obtained inserting x_{hyp} in the equation of the hyperbola); the one on the left is obtained by rotating by 180° degrees the element on the right.
The interpolation is carried out for values of x_{hyp} ranging from 0 to $w_{hyp}/2$. A small gap is left between the two parts to avoid any issues arising from expanding the spline interpolation over the range of x_{hyp} values set as input.
The upper side of the two parts of the hyperbolic cylinder is opaque while the lower part is the reflective one.

As SolTrace generates problems when tracing rays on a spline-defined element (the incident rays sometimes pass through the element even if the transmissivity is set to 0), a third flat element, w_{hyp}wide and as long in the longitudinal direction as the first two elements, is added over the hyperbolic cylinder. This "cover" is a completely opaque element that prevents all rays from passing through.
The longitudinal length of the hyperbolic cylinder is usually set using the analysis carried out in Chapter 3.2.1, so that no end-loss occurs in the second reflection stage.

The absorber is modelled as a flat opaque element centred in the origin whose width is set at w_{abs}. The longitudinal length is computed with the same principles of the one of the hyperbolic cylinder.

4.4 Auxiliary stage

The auxiliary stage is the last stage of the model and consists of two flat opaque elements: one is put above the primary focus point to intercept any ray that may not be caught by the hyperbolic cylinder and the other below the x-axis to intercept any ray that is not caught by the absorber.
These two elements are set as the final stage so that they don't interfere with the path of the rays until these have left the reflective stages of the model.

4.5 Different options of focal length for BDLFR systems

Up to this point, the mirrors have been considered to be parabolic (in the edge ray analysis of Chapter 3.2) with a focal length equal to their slant range.
In a commercial LFR system, the mirror either have a small curvature, constant for all the mirror, or no curvature at all. This is done in the effort to reduce the investment cost of the plant: flat mirrors are much cheaper than curved ones; if a parabolic curvature is introduced, it is surely more convenient to order Nm mirrors with the same curvature than Nm mirror with Nr different curvatures.
It is interesting to analyse the effects of different curvature options (and therefore of different focal lengths) on the optical efficiency of the system.
A similar analysis has been conducted by Boito P. et al. (2016) [14] for LFR systems. Position of the mirrors, mirror widths and focal distances have been analysed for different optimization methods. As a result, the introduction of the focal length as function of the mirror position generates an increase in optical efficiency of about 4.46% with respect to a configuration with a single focal length for all mirrors.
It is then worth exploring the effects of the focal length on the optical efficiency on a BDLFR system.

Four different optical lengths options are taken into consideration:

1. focal length of each mirror equal to its slant range
2. focal length of each mirror equal to the average slant range of the mirror
3. flat mirrors
4. focal length as proposed by Boito P. et al. (2017) [15].

where the slant range of each mirror is defined as $d = \sqrt{x_m^2 + h^2}$.

In 2017 Boito et al. analysed further the effects of the focal length on the annual geometric efficiency of a LFR system obtained by integrating the pointwise efficiency (i.e., the efficiency given the sun position) over the distribution of the sun position during the year [15]. The pointwise efficiency is computed by calculating

numerically with high precision the fraction of the mirror that projects the reflected rays within the receiver opening.

The layout considered (Figure 4-2) consists of a single mirror (all shading and blocking effects are then ignored) 2W wide put ad a distance x_m from the middle section of the receiver and that has a certain focal length Z. The mirror reflects radiation towards a flat receiver 2L wide and put at a height of H. Since all the quantities visible on the transversal plane are adimensionalized with respect to the receiver height, $h = \frac{H}{H}$ is set to 1 and the adimensional quantities are defined as $x = \frac{x_m}{H}$, $l = \frac{L}{H}$, $z = \frac{Z}{H}$, and $w = \frac{W}{H}$.

The aim of the paper is to find the functional form G of the equation that gives the optimal focal length of the mirror given the values of x, w, l and ψ (latitude, for this part only): $z = G(x, l, w, \psi)$.

After introducing some constraints for the different values of mirror and receiver widths, it becomes clear that the optimal focal length is not a function of the receiver and mirror width, that can be eliminated from the equation. The functional form of G is then only a function of the position of the mirror and of the latitude.

The functional form selected by the study is the power law

$$G_\psi(x) = z(x) = a_\psi + b_\psi \, x^{1.6} \tag{4.3}$$

Both coefficients are function only of the latitude.

The analytical form of both coefficients is also reported:

$$a_\psi = 1.0628 + 0.0467\psi^2 \tag{4.4}$$

$$b_\psi = 0.7448 + 0.1394\psi^2 \tag{4.5}$$

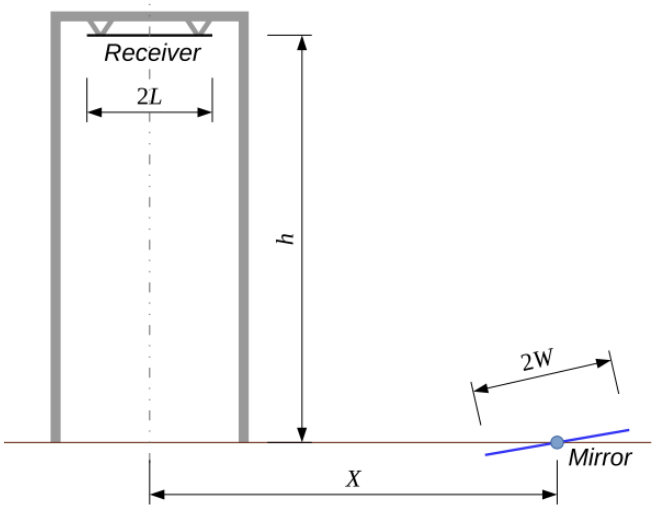

Figure 4-2 Set up used by Boito et al. to find the optimal focal length for a mirror of a LFR system[15].

To adapt these results to a BDLFR system the parameter by which all others are rendered dimensionless will be the height of the hyperbola corner I_z as defined in equation (3.41). This equals to state that this type of focal length approach aims to maximize the intercept factor on the hyperbola.

The different dimensional focal length options represented in Figure 4-3 are obtained for a noon optimized configuration (h=10, f=0.8 and Nr=10).

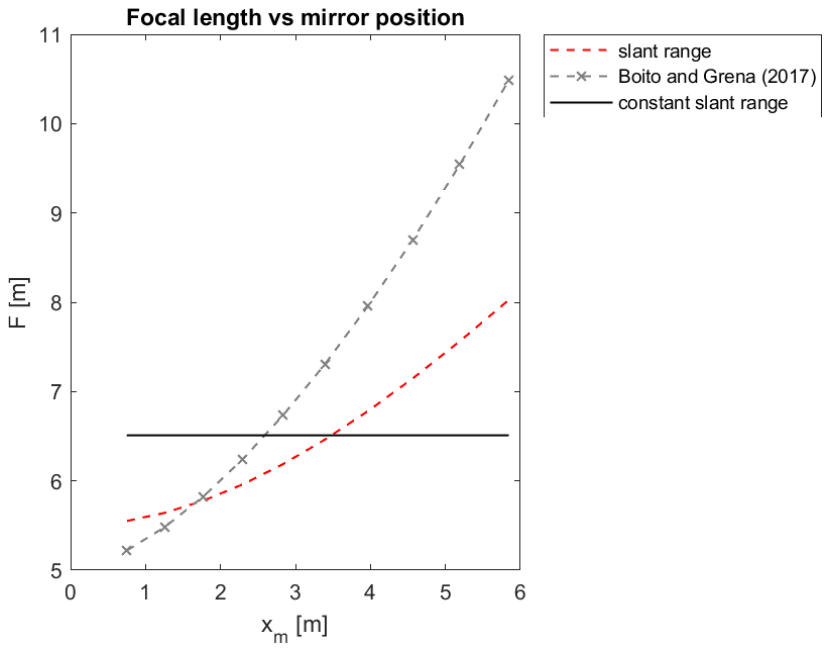

Figure 4-3 Dimensional focal length as a function of mirror position for a noon optimized configuration with geometrical parameters: f=0.8 h=5.5 and Nr=10.

The focal length option defined by Boito and Grena will be, from now on, be referred to as optimal focal length.

It is now interesting to evaluate the influence on the performance of the different focal length options. To this end, the optical efficiency on the day of the spring equinox of the systems are compared. The geometrical parameters of the simulations are the same used to define the focal length in *Figure 4-3*. The time step adopted is of 1 hour starting from the first hour of daylight.

Figure 4-4 shows the optical efficiency of the system for different solar times.

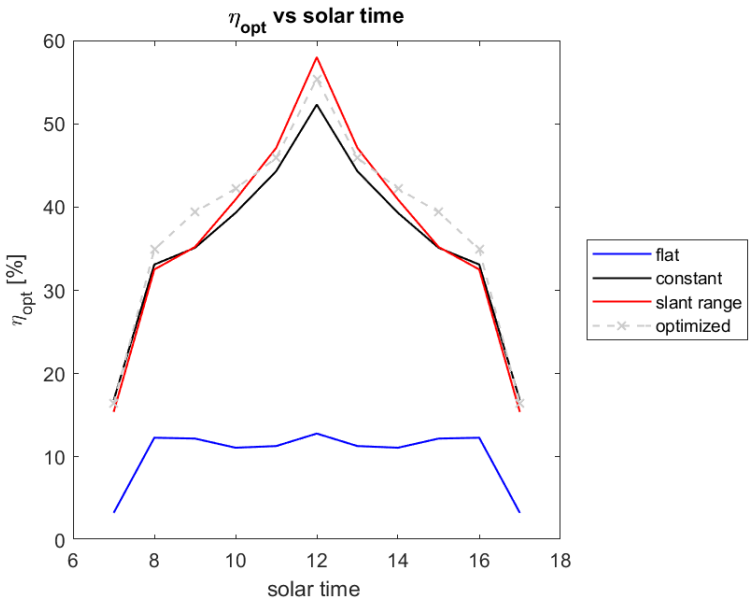

Figure 4-4 Most influential optical efficiency components for the different focal options (Nr=10, f=0.8, h=5.5 m).

The optical efficiency of the system will the defined more in detail in Chapter 5. For this analysis it is sufficient to define it as the ratio between the power impinging on the absorber and the one that would be collected by the mirror if they were to face the sun with an incidence angle between their normal and the sun vector equal to 0°.

The trend highlighted seems to prove that the optimized focal length guarantees a high optical efficiency when the sun is lower on the horizon, while the slant range is the best option during the centra hours of the day. The constant curvature configuration is competitive in all the daylight hours but comes up short in the middle region of the day. The flat-mirrored configuration instead is clearly the worst of the four possible options.

From this analysis can be derived that configurations with a constant curvature of the mirrors are a good alternative to individually curved mirrors, since in a techno-economic analysis they would be favoured by the lower plant cost. The flat mirrors sometimes used in LFR systems, instead, are highly ineffective in a BLDFR system.

5 Optical losses and efficiency evaluation

The optical losses of a BDLFR system can be divided in: cosine loss, hyperbola shading loss, shading loss (mirror on mirror), blocking loss, lack of interception on hyperbola and lack of interception on the absorber.

The cosine loss is the loss of power due to the existence of an incidence angle ϕ between the incoming sun rays and the normal to the primary reflector surface: the power impinging on the mirror is decreased by a factor equal to the cosine of the incidence angle ϕ .

The hyperbola shading loss is the loss of power due to the shadow that the hyperbola casts on the mirror field, impeding the light from reaching one mirror or another.

The shading loss is instead shading acted by one mirror row on the next.

The blocking loss occurs when the light does reach the surface of a mirror, but it's reflected onto the back of the previous one and it is unable to reach the second stage of reflection.

As for the lack of interception of hyperbola and absorber, both include spillage losses (the sun rays pass on the side of the hyperbola and of the absorber) and end-losses (sun rays miss the hyperbola or the absorber because these elements are too short in the longitudinal direction). The distinction is made because the causes of these two types of loss are different: the first is due to aberration of the primary reflectors while the second is mainly due to the longitudinal angle of the sun. As θ_l increases the reflection of the sun beams will take place further along the longitudinal direction and if the absorber (or hyperbola) is not long enough part of the energy collected by the field mirrors is lost.

Two ways to evaluate the first four losses have been studied: geometric method and SolTrace simulation. For both methods, the intercept factors are computed directly with Soltrace simulation taking as inputs the power leaving the mirror field computed geometrically in the first method and through previous simulation in the second.

5.1 Losses evaluation through geometric method

In the geometric method the loss of power is associated to the loss of useful area of a mirror. If no losses occurred, the area available for solar energy collection would be given by the equation:

$$A_{id} = w_m * L_f * N_m \tag{5.1}$$

where w_m is the width of each mirror, L_f the longitudinal length of the mirror field and N_m the number of mirrors (left and right of the z-axis).

The ideal power that can be intercepted by the mirror field is given by:

$$P_{id} = DNI * A_{id} \tag{5.2}$$

where DNI is the direct normal irradiance in the day, hour and latitude considered.

To simplify calculations all the mirrors are modelled as flat, i.e. as a straight line passing through the mirror centre. Their interaction with the sun rays however is considered to be the one of a parabolic mirror that concentrates the rays to the primary focus point, ignoring the aberration effects.

Furthermore, all the losses, except for the cosine loss, are computed considering the projection of the sun vector on the transversal plane. This method is recommended when a quick and time-saving estimation of the losses is required or in cases is which the qualitative trend of the loss is the main focus of the analysis. The method of the Soltrace simulations instead is accurate both when the sun vector is exactly on the transversal plane and when the real position of the sun is considered ($\theta_l \neq 0$).

This method doesn't account for irregularities of the reflective surfaces such as slope and specularity errors. The only aspect of realism introduced is the presence of a mirror reflectivity ρ_m lower than 1.

5.1.1 Cosine loss

As stated before, the cosine loss is given by the presence of an incidence angle between the normal to the mirror and the sun vector.

This loss can be seen as a reduction of useful area for the collection of the sunlight due to the projection of the mirror area in the direction of sun vector. The reduction factor is the scalar product of the mirror normal and the sun vector, both considered as three-dimensional vectors. For the i-th mirror:

$$\cos(\Phi_i) = m_i \cdot s \tag{5.3}$$

Where m_i and s are:

$$m_i = [m_{i_x}, 0, m_{i_z}] \tag{5.4}$$

$$s = [s_x, s_y, s_z] \tag{5.5}$$

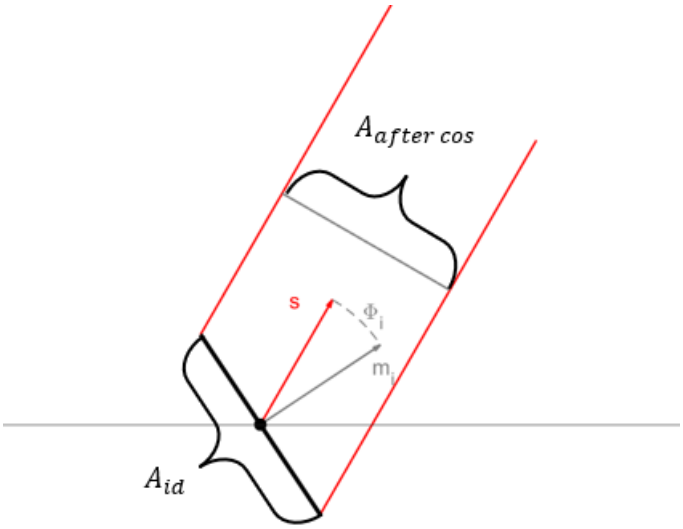

Figure 5-1 Effect of the incidence angle between mirror normal and sun vector on the actively receiving area of the mirror.

After considering the cosine effect for each mirror, the area truly available for power collection is:

$$A_{after\ cos} = \sum_i w_m * L_f * \cos(\Phi_i) = w_m * L_f * \sum_i \cos(\Phi_i) \tag{5.6}$$

The cosine efficiency for the entire mirror field is defined as:

$$\eta_{cos} = \frac{A_{after\ cos}}{A_{id}} = \frac{w_m * L_f * \sum_i \cos(\Phi_i)}{w_m * L_f * N_m} = \frac{\sum_i \cos(\Phi_i)}{N_m} = \overline{\cos(\phi)} \tag{5.7}$$

So geometrically the cosine loss for the system can be computed as the average cosine of the incidence angle of the field.

The power available to the system, i.e. that can still be directed towards the absorber, is given by:

$$P_{after\ cos} = P_{id} * \eta_{cos} \tag{5.8}$$

5.1.2 Hyperbola shading loss

Depending on the hour of the day, the shadow cast by the hyperbola can cover one part or another of the mirror field: those mirrors will not contribute to the power collection and they represent a loss for the system.

Every mirror can be completely shaded or only partially: in the second case the intersection of the hyperbola shadow and the mirror surface must be computed, also considering that at most two mirrors can be partially shaded: one by the projection the left hyperbola corner and one by the right. These two mirrors are hereafter referred to as extreme left and right intersected mirrors.

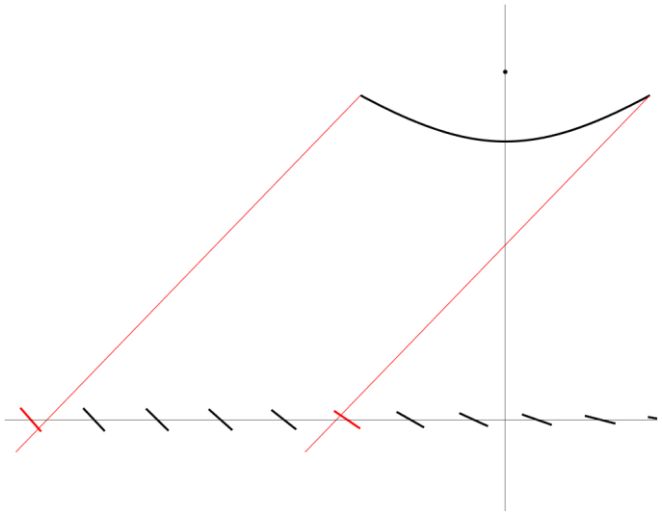

Figure 5-2 Left and right extreme mirrors intersected by the shadow cast by the hyperbola.

The lost area for the two mirrors highlighted in *Figure 5-2* can be evaluated as follows. For the left-side mirror:

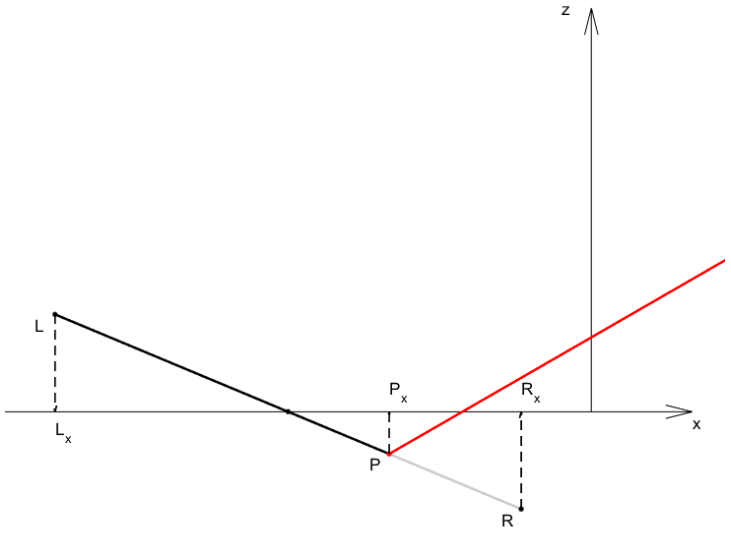

Figure 5-3 Extreme left mirror shaded by the hyperbola (grey area).

$$A_{sh_{left}} = \frac{R_x - P_x}{\cos \beta_{left}} * \cos \Phi_{left} * L_f \tag{5.9}$$

The subscripts shown for the incidence and tilt angles refer to the mirror that intersects the projection of the left corner of the hyperbola on the ground level.

The factor $\frac{1}{\cos \beta_{left}}$ allow to pass from the distance $\overline{P_x R_x}$ to the distance $\overline{PR}$, and the factor $\cos \Phi_{left}$ takes into account that not all the area of the mirror was available to begin with for the cosine effect.

For the right-side mirror instead:

$$A_{sh_{right}} = \frac{P_x - L_x}{\cos \beta_{right}} * \cos \Phi_{right} * L_f \tag{5.10}$$

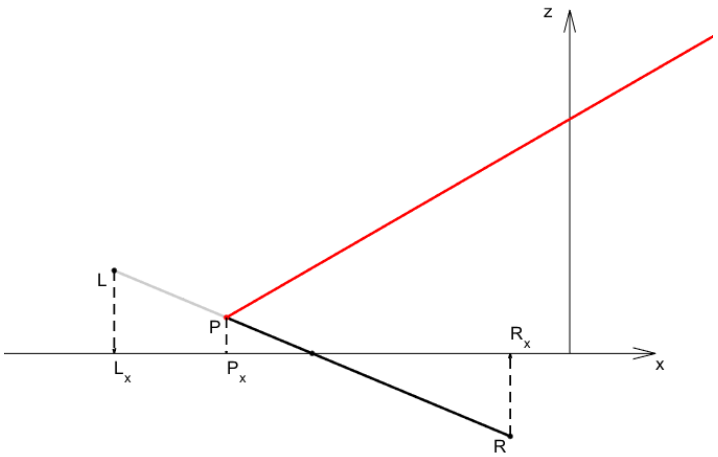

Figure 5-4 Extreme right mirror shaded by the hyperbola (grey area).

Lastly, for a completely shaded mirror the lost area will be computed as:

$$A_i^{sh_{hyp}} = w_m * L_f * cos(\Phi_i) \tag{5.11}$$

The total area lost due to hyperbola shading will be the sum of the three areas:

$$A_{tot}^{sh_{hyp}} = A_{sh_{right}} + A_{sh_{left}} + \sum_{i=left+1}^{right-1} A_i^{sh_{hyp}} \tag{5.12}$$

The area still available for power collection is:

$$A_{after\ hyp} = A_{after\ cos} - A_{tot}^{sh_{hyp}} \tag{5.13}$$

Similarly to the cosine loss the hyperbola shading efficiency is computed as:

$$\eta_{hyp} = \frac{A_{after\ hyp}}{A_{after\ cos}} \tag{5.14}$$

The power available to the system is:

$$P_{after\ hyp} = P_{after\ cos} * \eta_{hyp} \tag{5.15}$$

5.1.3 Shading and blocking loss

These two losses must be evaluated together as they are not independent from one another. In fact, in some cases, the presence of shading limits or prevents the occurrence of blocking on the same mirror. It follows that four different interactions between these two phenomena are possible on a single mirror: pure shading, pure blocking, coexistence of shading and blocking and finally the case in which shading completely trumps blocking.

It is important to consider that only mirrors not shaded from the hyperbola can be interested by mirror to mirror shading, so the following analysis only applies to the mirrors not interested by hyperbola shading.

Pure shading occurs when the previous mirror row (that precedes the analysed mirror in the direction of arrival of the light, mirror i+1 in *Figure 5-5*) casts a shadow (grey area in *Figure 5-5*) on the surface of the following mirror row, therefore limiting the surface available for power collection. To compute the shaded area the intersection point P must be computed as the solution of the following system:

$$\begin{cases} P_z - L_{i+1,z} = \dfrac{s_z}{s_x} * \left(P_x - L_{i+1,x}\right) \\ P_z = -\dfrac{m_{i,x}}{m_{i,z}} * (P_x - x_i) \end{cases} \tag{5.16}$$

The first equation is the line having slope given by the sun vector that passes through the left rim of the previous mirror row, the second is the equation that describes the i-th mirror, according to the hypothesis of considering the mirrors as flat elements.

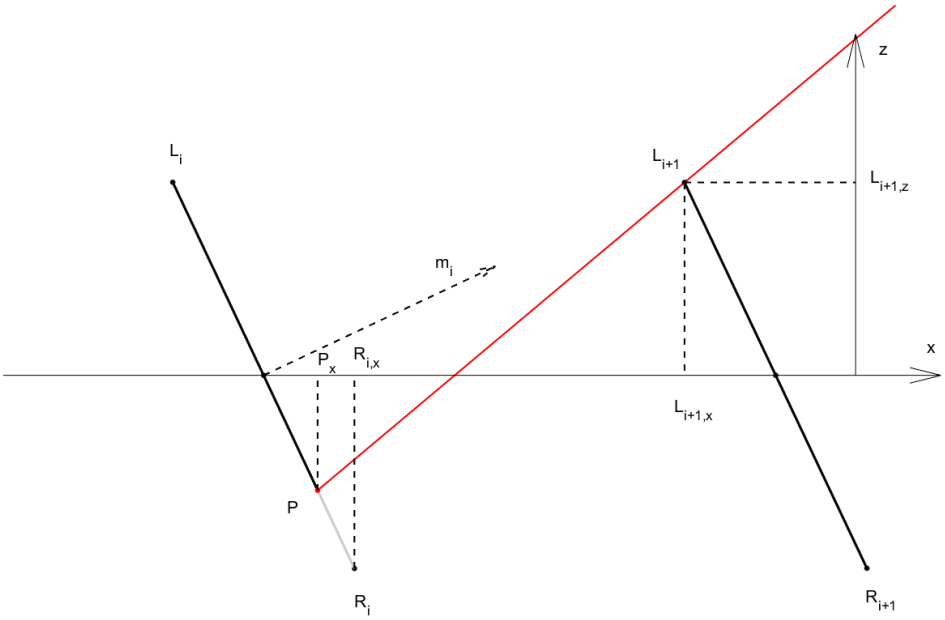

Figure 5-5 Pure shading scheme.

Once the intersection the point P is found the shaded area can be computed as:

$$A_i^{sh} = \frac{R_{i,x} - P_x}{\cos \beta_i} * \cos \phi_i * L_f \tag{5.17}$$

Pure blocking occurs when a sun ray correctly hits the surface of a mirror but, in being reflected, is stopped by the back of the previous row and is therefore unable to reach the hyperbola to be redirected towards the absorber. The portion of mirror interested by this phenomenon represents a loss of useful collection area.

As previously mentioned, the mirrors themselves are represented as lines passing through the mirror centre instead of parabolas. The behaviour of the reflected rays, however, is the one of parabolically reflected rays, i.e. they converge towards the primary focus point, ignoring aberration effects. The first point of the surface of the i-th mirror that will be interested by blocking can then be found geometrically as the intersection between the i-th mirror line and the line that connects the left rim of the previous mirror (i+1 mirror) to the primary focus point (dashed red line in *Figure 5-6*). The intersection is point T. Mathematically this translates into the resolution of the following system:

$$\begin{cases} T_z = T_x * \dfrac{L_{i+1,z} - h}{L_{i+1,x}} + h \\ T_z = -\dfrac{m_{i,x}}{m_{i,z}} * (T_x - x_i) \end{cases} \tag{5.18}$$

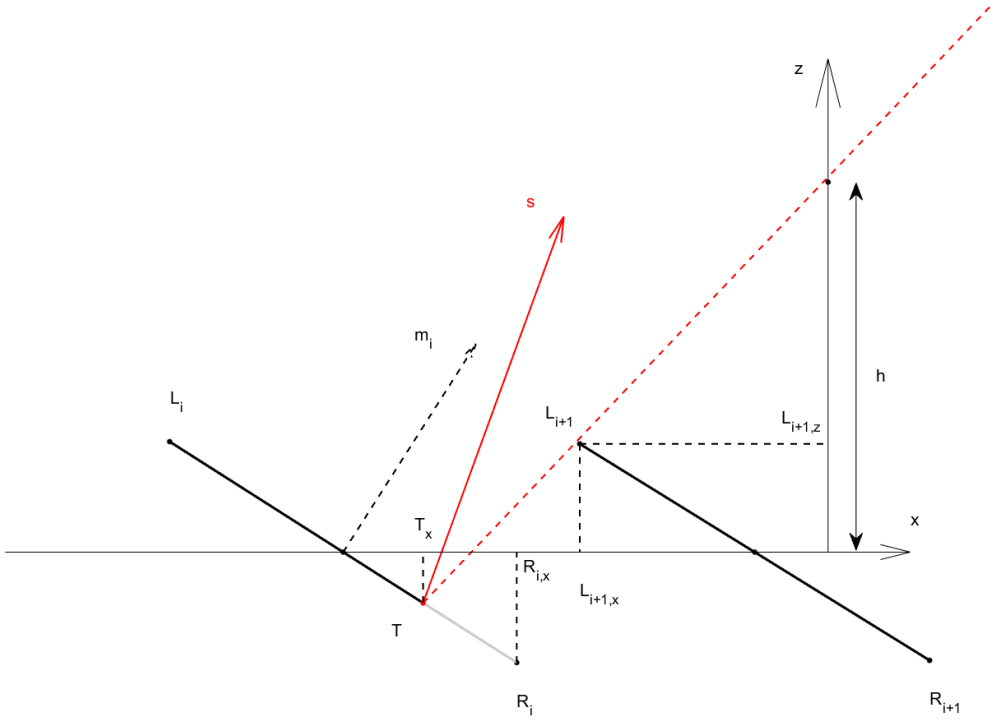

Figure 5-6 Pure blocking scheme.

In analogy to the area loss for shading, the lost area due to blocking in this case is evaluated as:

$$A_i^{block} = \frac{R_{i,x} - T_x}{\cos \beta_i} * \cos \phi_i * L_f \tag{5.19}$$

As before mentioned, blocking and shading can coexist on a single mirror as exemplified in Figure 5-7.

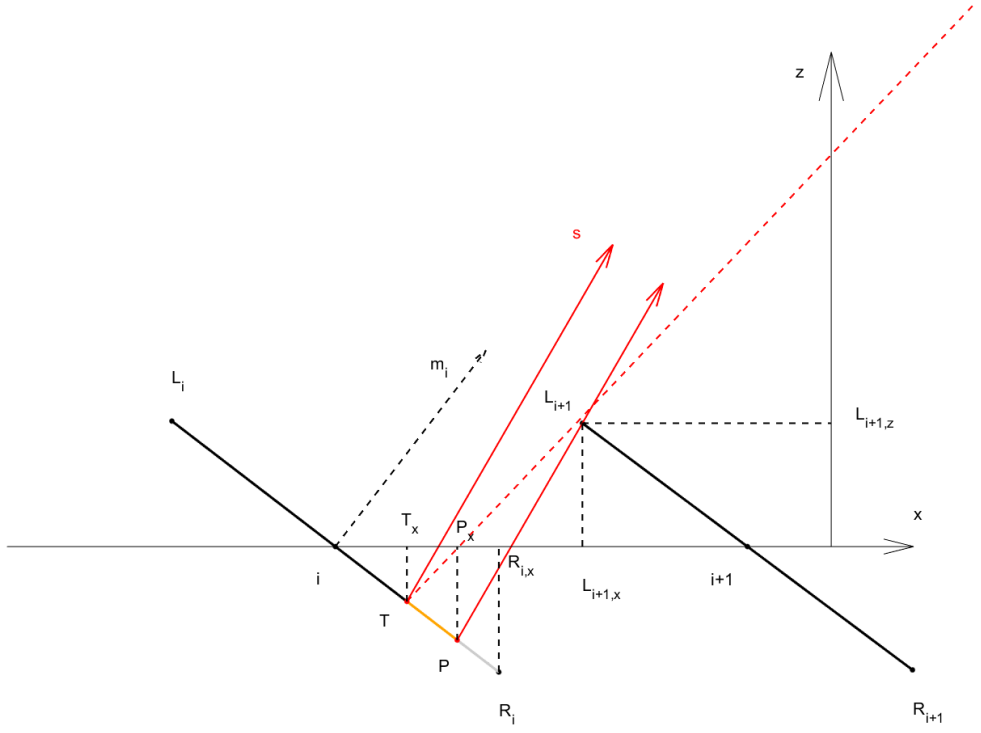

Figure 5-7 Simultaneous presence of shading and blocking on a mirror.

In this case, the shaded area is computed exactly as in the case of pure shading; the blocked area instead is only the area between the points T and P (orange area in Figure 5-7) and not, as in the case of pure blocking, between T and R_i. This derives from the fact that since no light reaches the shaded area, no blocking can occur (since blocking is the reflection of a ray on the back of another mirror row).

The blocked area is the computed as:

$$A_i^{block} = \frac{P_x - T_x}{\cos \beta_i} * \cos \phi_i * L_f \tag{5.20}$$

The case in which the presence of shading impedes the occurrence of blocking is just a particular case of the previous one: in case of coexistence, in fact, the intersection point of the shading (P) falls between the intersection point of the blocking (T) and the right rim of the i-th mirror (R_i). If, instead, the intersection point of the blocking falls between the shading one and the right rim, then the entire area subjected to blocking is shaded from the previous mirror row: since no rays can arrive, no rays can be reflected on the back of the previous mirror row (Figure 5-8).

The blocked area is then null, while the shaded area is computed as in the case of pure shading.

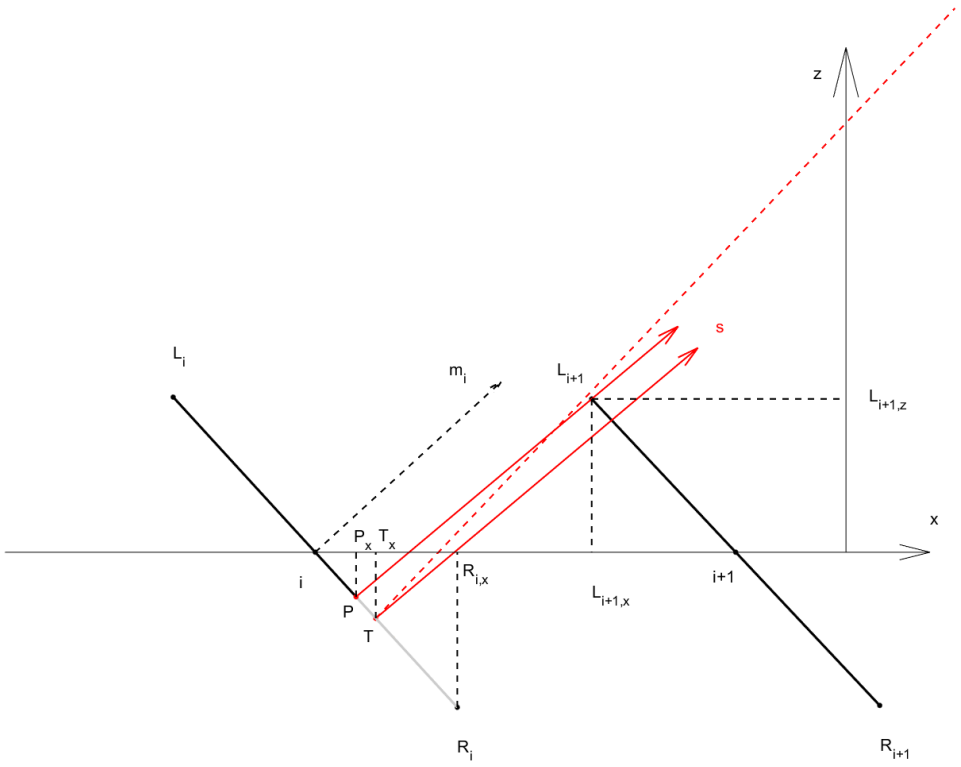

Figure 5-8 Shading prevents blocking.

The total area lost due to shading mirror to mirror is computed as:

$$A_{tot}^{sh} = \sum_{i=1}^{N_m} A_i^{sh} \tag{5.21}$$

The area still available for power collection after the shading loss is:

$$A_{after\ sh} = A_{after\ hyp} - A_{tot}^{sh} \tag{5.22}$$

The shading efficiency is computed as:

$$\eta_{sh} = \frac{A_{after\ sh}}{A_{after\ hyp}} \tag{5.23}$$

The power still available to the system is:

$$P_{after\ sh} = P_{after\ hyp} * \eta_{sh} \tag{5.24}$$

The total area lost due to blocking is computed as:

$$A_{tot}^{block} = \sum_{i=1}^{N_m} A_i^{block} \tag{5.25}$$

The area that successfully reflects the light towards the hyperbola is then:

$$A_{after\ block} = A_{after\ sh} - A_{tot}^{block} \tag{5.26}$$

The shading efficiency is computed as:

$$\eta_{block} = \frac{A_{after\ block}}{A_{after\ sh}} * \rho_m \tag{5.27}$$

The power still available to the system is:

$$P_{after\ block} = P_{after\ sh} * \eta_{block} \tag{5.28}$$

5.1.4 Intercept factors

The intercept factors evaluate losses due to aberration effects and end-loss (in case a finite length of the absorber is considered). The geometrical analysis of the aberration is carried out only through the SolTrace simulation, providing as input the power available after blocking computed in equation (5.28). The procedure will be explained in Chapter 5.2.5

5.2 Losses evaluation through SolTrace simulations

To evaluate the different losses a series of Soltrace simulations aiming to evaluate the power loss due a particular loss are performed.

The ideal power collected by the mirror field is computed as beforementioned in the geometric method and it is again the starting point of the method.

To perform a Soltrace simulation a certain number of intersections with the first stage must be set. As this number increases the simulation becomes more and more representative of the power impinging on the mirrors and so of the optic loss in question.

Differently from the geometric method, here the optical errors are taken into account. Their values are the one specified in Chapter 4.2. The reflectivity of the mirror is also accounted for ($\rho_m = 0.93$).

5.2.1 Cosine loss

To evaluate this loss only the mirror field is necessary. All the primary reflectors are generated with their correct tilt angle given by the tracking equations according to the set position of the sun.

To avoid including in this simulation also other losses (such as shading mirror on mirror) the mirrors are generated as perfectly transparent elements (transmissivity equal to 1). This way, the generated rays are allowed to pass through a mirror and, if that is the case, hit on the following mirror row as if the previous didn't exist.

Through this expedient the only source of power loss is the reduction of the area of the mirrors due to the incidence angle. It is useful to underline that this effect is rendered by Soltrace by decreasing the number of intersections on a single mirror compared to the case in which no intersection angle is present and keeping constant the power per ray parameter for each mirror.

For each mirror the number of intersections is tallied and then the total power impinging on the mirror field, and so what remains of the ideal power after the cosine loss, is computed as:

$$P_{after\ cos} = \sum_{i=1}^{N_m} n°\ of\ intersections\ (i) * ppr \tag{5.29}$$

The cosine efficiency is evaluated as:

$$\eta_{cos} = \frac{P_{after\ cos}}{P_{id}} \tag{5.30}$$

5.2.2 Hyperbola shading loss

To evaluate the hyperbola shading loss, also the hyperbolic cylinder must be included in the simulation. The hyperbola is modelled as a completely opaque body (absorptivity equal to one). This way all the rays that hit it will not pass through and will represent the loss of power due to hyperbola shading. The mirror field is modelled exactly as in the cosine loss analysis.

The geometric parameters are all specified in the tracking equations section.

The hyperbola element will be present in all following simulations.

After the simulation, the total number of rays intersections on the mirror field is again tallied and the power after the hyperbola shading loss computed as before:

$$P_{after\ hyp} = \sum_{i=1}^{N_m} n°\ of\ intersections\ (i) * ppr \tag{5.31}$$

The hyperbola shading loss is evaluated as:

$$\eta_{hyp} = \frac{P_{after\ hyp}}{P_{after\ cos}} \tag{5.32}$$

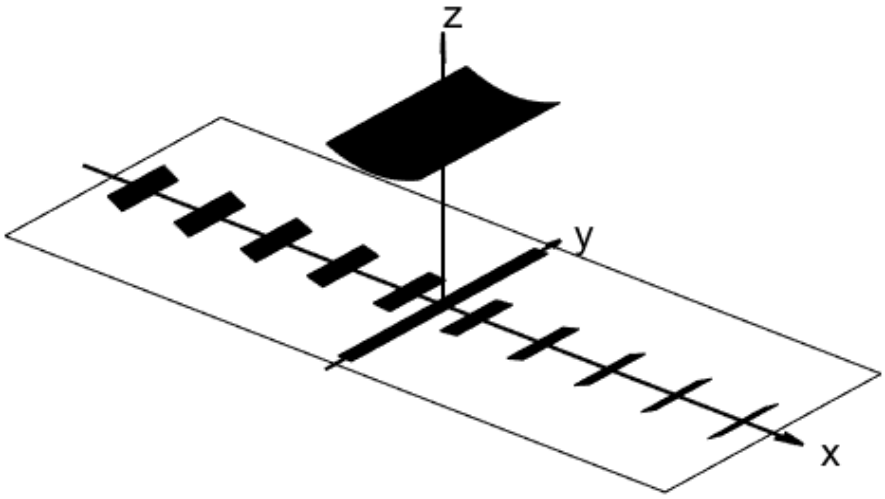

Figure 5-9 SolTrace set up for the evaluation of the hyperbola shading loss. This set up is common to all other losses, taken that the optical properties of the elements are changed accordingly.

5.2.3 Shading loss

For this loss the optical properties of the mirror field must be changed. To recreate the effect of shading all mirrors are modelled as completely opaque bodies, so that when a ray hits one mirror, it will not be transmitted and so allowed to also intersect the following mirror row, therefore recreating the effect of shading mirror on mirror. Moreover, since all the rays are absorbed, none can be reflected on the back of other mirror rows, hence avoiding to include also the blocking loss in the computation.

After the simulation, the total number of rays intersections on the mirror field is again tallied and the power after the shading loss computed as before:

$$P_{after\ sh} = \sum_{i=1}^{N_m} n°\ of\ intersections\ (i) * ppr \tag{5.33}$$

The shading loss is evaluated as:

$$\eta_{sh} = \frac{P_{after\ sh}}{P_{after\ hyp}} \tag{5.34}$$

5.2.4 Blocking loss

To recreate the blocking effect the front surface of the mirrors must be allowed to reflect the rays, while the back of the mirrors remains completely absorbent. Depending on the kind of analysis to carry out, the value of reflectivity of the mirrors can vary from one to other typical values ($\rho_m = 0.93$ is the chosen value in case of a real mirror). Also, all the options available on Soltrace to recreate a more real mirror, with slope and secularity errors, are activated.

To evaluate the power effectually leaving the mirror field (i.e. not blocked by the back of other mirrors), first the number of intersections on the back of each mirror is tallied and then the amount of power blocked is evaluated:

$$P_{blocked} = \sum_{i=1}^{N_m} n° \; of \; intersections \; "back" \; (i) * ppr \tag{5.35}$$

Then the power still available to the system after the blocking loss is obtained as:

$$P_{after\ block} = P_{after\ sh} - P_{blocked} \tag{5.36}$$

The blocking loss is evaluated as:

$$\eta_{block} = \frac{P_{after\ block}}{P_{after\ sh}}$$

5.2.5 Intercept factors

To compute both intercept factors the rays must be allowed to travel until they reach the hyperbola and then the absorber. For this purpose, the back of the hyperbolic cylinder (the side facing the ground) is converted to a reflective body, with the same characteristic of the mirror field.

The absorber is generated as a rectangular body of at the centre of the reference system and with absorptivity equal to 1.

Two auxiliary surfaces are also introduced in the simulation but belonging to a second stage, so that the rays will first interact with the field, initially bypassing them and only at the end they will be collected by the auxiliary stage.

These two flat surfaces are put one above the hyperbolic cylinder and one below the absorber. Both are generated wide enough, transversally and longitudinally, to collect all the rays that may miss the hyperbola or the absorber. The one above the hyperbola is denominated as upper auxiliary surface, the one below the absorber as lower auxiliary surface.

The power impinging on the two auxiliary surfaces is obtained as:

$$P_{aux\ up} = n° \; intersections \; upper \; auxiliary \; surface * ppr \tag{5.37}$$

$$P_{aux\ low} = n° \; intersections \; lower \; auxiliary \; surface * ppr \tag{5.38}$$

The following powers are defined:

$$P_{after\ \gamma_{hyp}} = \left(P_{after\ block} - P_{aux\ up}\right) * \rho_{hyp} \tag{5.39}$$

$$P_{after\ \gamma_{abs}} = P_{after\ \gamma_{hyp}} - P_{aux\ low} \tag{5.40}$$

$P_{after\ \gamma_{hyp}}$ is the power still available to the system after considering both the lack of impact on the hyperbolic cylinder by some rays and its absorption of power due to an eventual $\rho_{hyp} < 1$.

$P_{after\,\gamma_{abs}}$ is the power that finally hits the absorber, considering that some rays may not be directed correctly by the hyperbola and miss the absorber on the ground. This is the useful power output of the system.

However, this is not the only power that impinges on the absorber: in some configurations some of the rays may directly hit the absorber without being intercepted first by the mirror field.

This power is evaluated by obtaining the total power hitting the absorber and then subtracting the one that comes from the mirror field:

$$P_{abs\,tot} = n°\ intersections\ on\ the\ absorber * ppr \tag{5.41}$$

$$P_{abs\,dir} = P_{abs\,tot} - P_{after\,\gamma_{abs}} \tag{5.42}$$

If only the power coming from the mirror field is of interest, a smarter solution is to set the absorber as part of the second stage: this way only the rays that have been collected first by the mirror field will be counted and the $P_{after\,\gamma_{abs}}$ can be directly obtained and the direct power computed as difference between the power measured with the absorber in the first stage and the one measured with the absorber in the second.

The intercept factors are computed as:

$$\gamma_{hyp} = \frac{P_{after\,\gamma_{hyp}}}{P_{after\,block}} \tag{5.43}$$

$$\gamma_{abs} = \frac{P_{after\,\gamma_{abs}}}{P_{after\,\gamma_{hyp}}} \tag{5.44}$$

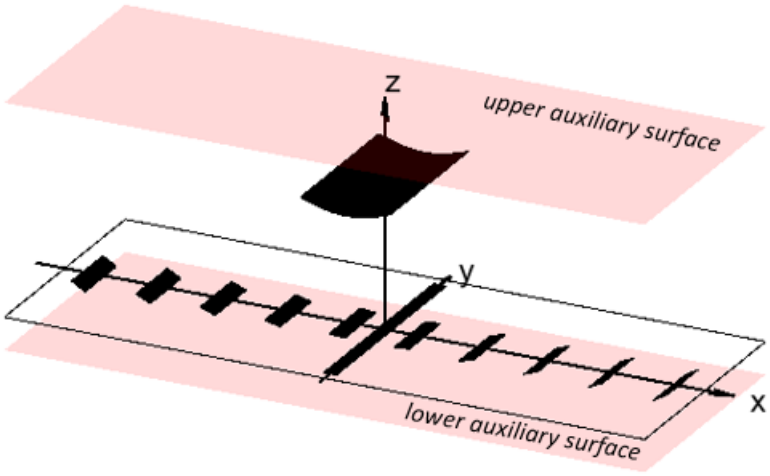

Figure 5-10 Introduction of the upper and lower auxiliary surfaces for the evaluation of the intercept factors on the hyperbola and absorber.

5.3 Instantaneous total and optical efficiency of the system

The total efficiency includes the contribution of the direct radiation hitting the absorber as part of the useful output, while the optical one considers as useful radiation only the one arriving on the absorber after being

reflected by the field. The latter is more interesting as in most cases the reflected radiation and the direct one hit the absorber in different regions: the first will move from the centre of the system towards North during the morning and back towards the centre in the afternoon; the opposite is true for the direct radiation. At noon the two will be completely disjointed and therefore not summable.

For the sake of completeness, both are shown:

$$\eta_{opt} = \eta_{cos} * \eta_{hyp} * \eta_{sh} * \eta_{block} * \gamma_{hyp} * \gamma_{abs} = \frac{P_{after\,\gamma_{abs}}}{P_{id}} \tag{5.45}$$

$$\eta_{tot} = \eta_{opt} + \frac{P_{abs\,dir}}{P_{id}} \tag{5.46}$$

A more direct and precise way of computing the optical efficiency is to place the absorber in the second stage of the

5.4 Comparison between the geometrical and SolTrace simulation methods

The values of the losses computed geometrically and the ones resulting from the series of SolTrace simulations are compared with two different tests: in the first the sun will be set on the transversal plane and will only spun transversal angles from 0° to 85°, in the second the sun will be set in the actual positions that it would occupy in the day of the equinox from sunrise to sunset. In the second test the position of the sun will be described by a non-null longitudinal angle.

In both simulations all optical errors and mirrors reflectivities are considered.

The geometrical parameters defining the system used for this comparison are summarized in Table 5-1.

Number of mirror rows, Nm	20
Primary focus height, h [m]	5.5
Hyperbola shape factor, f	0.8
Focal length	slant range of each mirror
Mirror spacing	noon-optimized
Primary reflectors longitudinal length [m]	1
Hyperbolic cylinder longitudinal length[m]	2
Absorber longitudinal length [m]	2
Position of first mirror row [m]	0.75
Hyperbola width, w_{hyp} [m]	2.063
Absorber width, w_{abs} [m]	0.358

Table 5-1 Geometrical parameters for comparison tests between geometrical and SolTrace simulations efficiency evaluation.

5.4.1 Transversal plane comparison

As the sun is set on the transversal plane, the sun vector is defined as $s = [\sin(\theta_t), 0, \cos(\theta_t)]$. By so defining the solar vector, the sun moves from the zenith position towards East remining on the transversal plane.

The average difference between the geometrically obtained and SolTrace simulations obtained curves reported in Figure 5-11 and Figure 5-12.

The delta reported in Figure 5-11 and Figure 5-12 is the average error committed in estimating the efficiencies and intercept factors geometrically with respect to the SolTrace simulations that are considered to be the real value. For all the different factors of loss, the geometrical computation of the losses is in agreement with the SolTrace simulations, with negligible average errors.

The slightly erratic behaviour of the SolTrace evaluated efficiencies is due to the random nature of the ray generation in SolTrace. As the number of hits on the first stage increases, so will the accuracy of the measurement of powers impinging on the different elements and so of the efficiency evaluation that will tend more and more to the value computed geometrically.

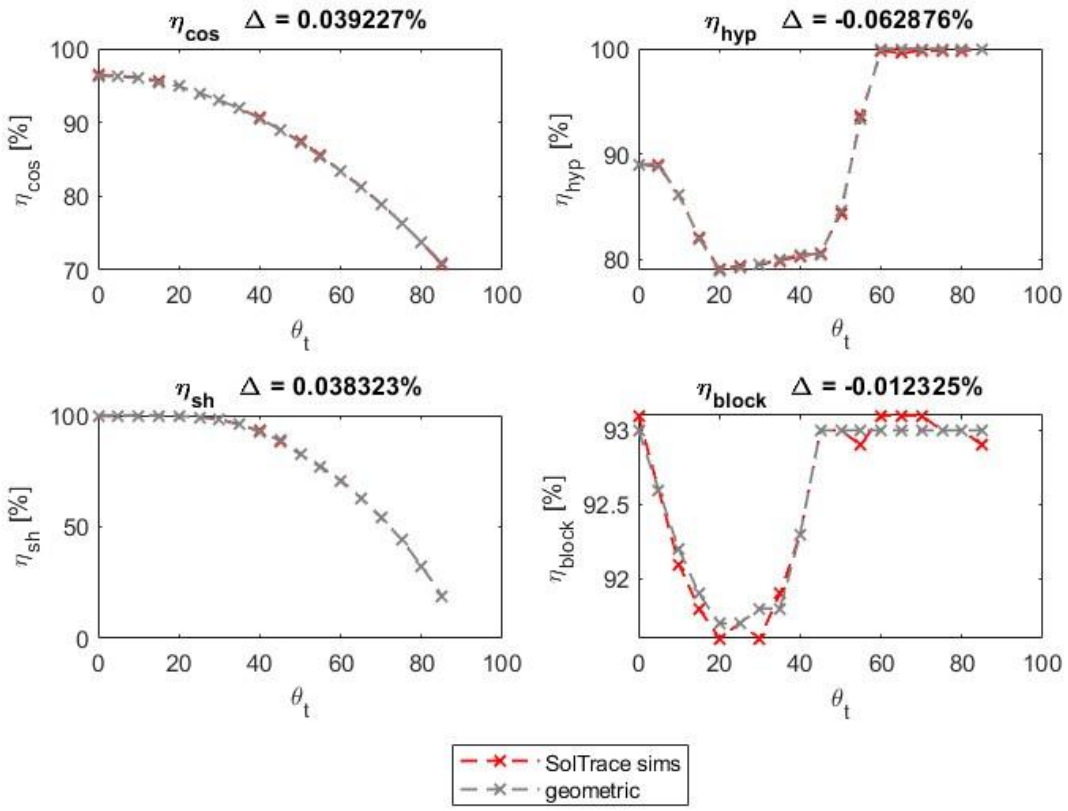

Figure 5-11 Comparison between the cosine, hyperbola shading, shading, and blocking efficiencies computed with the geometric method and with the SolTrace simulations obtained with the sun on the transversal plane.

The cosine efficiency decreases as the transversal incidence angle increases, mainly due to the average increase of incidence angle on the mirrors and consequent decrease of its average cosine. It is interesting to notice that the cosine efficiency is lower than 100% even for $\theta_t = 0°$. This is main point of difference between the PTC and LFR technologies. Considering an East-West tracking PTC, the incidence angle between the mirror normal and the sun vector exists only in the longitudinal plane because the receiver moves together with the parabolic mirror. In the LFR technology, instead, the receiver (primary focus point for a BDLFR) is fixed and even at noon ($\theta_t = 0°$ even if the sun weren't on the transversal plane) the mirrors must have a tilt with respect to the normal direction to correctly reflect the rays towards the focus point. An incidence angle on the mirror is then formed between the mirror normal and the sun vector, even in this test where the sun is on the transversal plane.

The hyperbola shading efficiency itself doesn't reach a value of 100% for $\theta_t = 0°$ because the first mirror row is shaded by the hyperbola. The efficiency then decreases as the hyperbola shadow moves through the mirror field, covering a larger number of mirrors and that have a low incidence angle. For values of θ_t ranging from 20° to 40° the efficiency increases slightly because, even if the number of mirrors interested by hyperbola shading remains almost constant, the cosine of their incidence angle is slightly lower. The hyperbola shadow then starts to move out of the mirror field (θ_t from 40° to 60°) decreasing the number of mirrors involved in the hyperbola shading loss. Once the shadow has moved outside the mirror field, the efficiency remains constant at 100%.

There appears to be almost no shading up until values of $\theta_t = 40°$. Afterwards, the mirrors begin to casts shadows on each other as their tilt angle has to increase to redirect correctly the sun rays.

The blocking loss at noon registers a value of about 93% not because of the presence of blocking, but because is this loss is included the reflectivity of the mirrors, set precisely at 0.93. Almost immediately the blocking efficiency decreases reaching a minimum for $\theta_t = 25°$. At this point, blocking becomes more and more difficult as shading takes hold on almost every mirror, hence again the increase of the efficiency up to the value of 0.93.

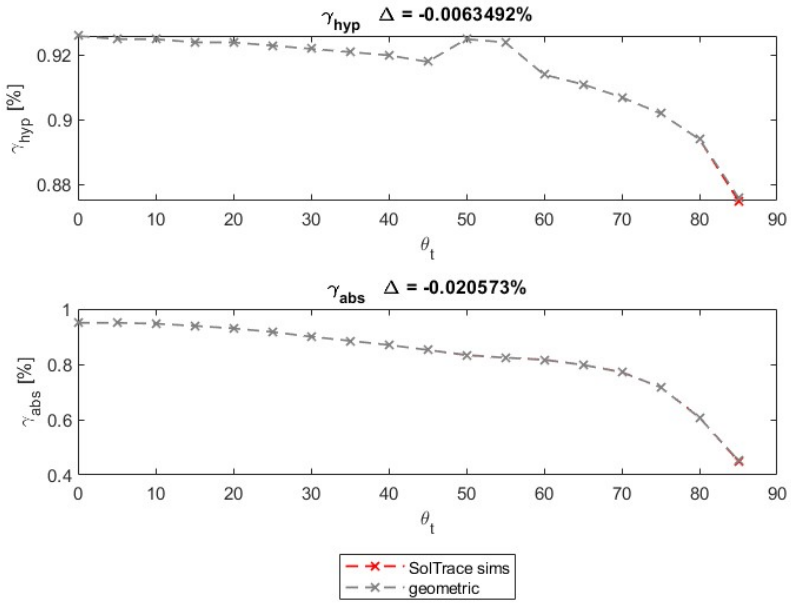

Figure 5-12 Comparison between the hyperbola and absorber intercept factors computed with the geometric method and with the SolTrace simulations obtained with the sun on the transversal plane.

The general trend of both intercept factors is to decrease as the transversal incidence angle of the sun increases. This is due to the higher incidence angle of the mirrors, especially those on the East side of the field, that accentuates the aberration effects of the parabolic mirrors. The incorrect reflection off the primary reflectors causes a decrease of the intercept factor on the hyperbola.

Even if the aberration-effected ray hits and is reflected off the hyperbola, his reflection angle will be different from the optimal one that would see it hit the absorber. As a result, the intercept factor on the absorber decreases consistently with the increase of θ_t.

Finally, a comparison between the two optical efficiencies obtained through the multiplication of all the efficiencies and intercept factors without the contribution of the radiation directly impinging on the absorber is presented. The values are also compared with the total efficiency computed directly on the absorber computed as:

$$\eta_{opt\,real} = \frac{n°\ intersections\ on\ abs * ppr}{P_{id}}$$

placing the absorber in the second stage, preventing it from receiving any direct radiation. This last formulation of the efficiency is the most accurate and therefore used as reference to evaluate the error introduced by each method.

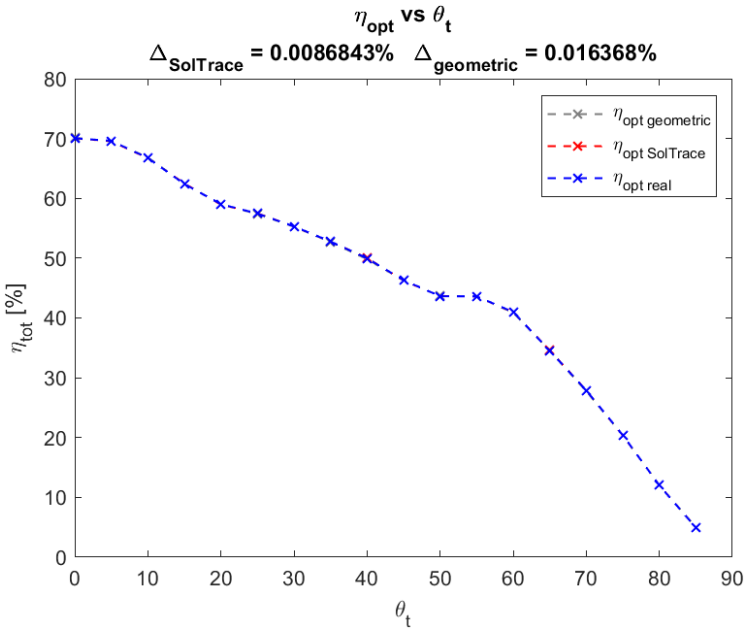

Figure 5-13 Comparison between the total efficiencies values computed with the SolTrace simulation method, geometric method and direct method.

Once again, the difference between the different curves is negligible, even if the SolTrace simulations method is slightly more precise.

It can be concluded that, if the analysis is carried out on the transversal plane, the geometric method offers a valid alternative to the time-consuming method of the consecutive SolTrace simulations. This simplified type of analysis, even if not very representative of the actual behaviour of the system during a particular day on the year, offers useful information on the main sources of loss of a certain configuration, and so

where to act to reduce them, without having to deal with all the three-dimensional complications that arise from considering the real position of the sun in a typical day of the year (i.e., correct computation of the hyperbolic cylinder and absorber longitudinal length, effects of the 3D-shading mirror on mirror, etc…).

As a last comment, the relative weight of the different losses is plotted against the transversal incidence angle for this test (Figure 5-14). The different contributions to the total power loss are plotted to show which one is the most relevant.

The contribution of the radiation hitting directly the absorber is shown as a surplus of power in the negative part of the y-axis. There is no direct radiation impinging on the absorber until θ_t reaches values of around 15-20° because the hyperbolic cylinder casts its shadow on the absorber. The direct contribution then decreases regularly because the first East mirror row gradually casts its shadow in the absorber, preventing it from receiving any direct radiation.

The power lost to cosine effect increases with θ_t, in accordance with the behaviour of η_{cos}, until it becomes one of the main sources of power loss for the system.

Reversely, the power lost to hyperbola shading is one of the main sources of loss when the sun is almost at the zenith, to then decrease and disappear when the hyperbola shadow leaves the mirror field.

Shading loss is almost inexistent for θ_t<30° but then it increases quickly and it represents the main source of loss of the system for high values of θ_t.

The blocking loss represents almost always a small part of the overall loss; however its value seems to change much more than the value of the blocking efficiency. This is due to the different denominator used to compute the two quantities. The value of η_{block} is referred to the power still available to the system prior to the blocking loss, the height of the segment in Figure 5-14 is lost power referred to the fixed ideal power. This implies that, as the optical efficiency of the system decreases, less power is already available to the system by the time the blocking stage is reached in the efficiency cascade. Considering almost constant the value of the blocking loss at about 0.93, the absolute contribution to the power loss will decrease. This mechanism is active in all losses but it becomes more important the more “downstream” the loss is.

This is also visible in the power lost to hyperbola and absorber intercept factors: both values decrease with the transversal incidence angle and yet their contribution to the overall power loss decreases.

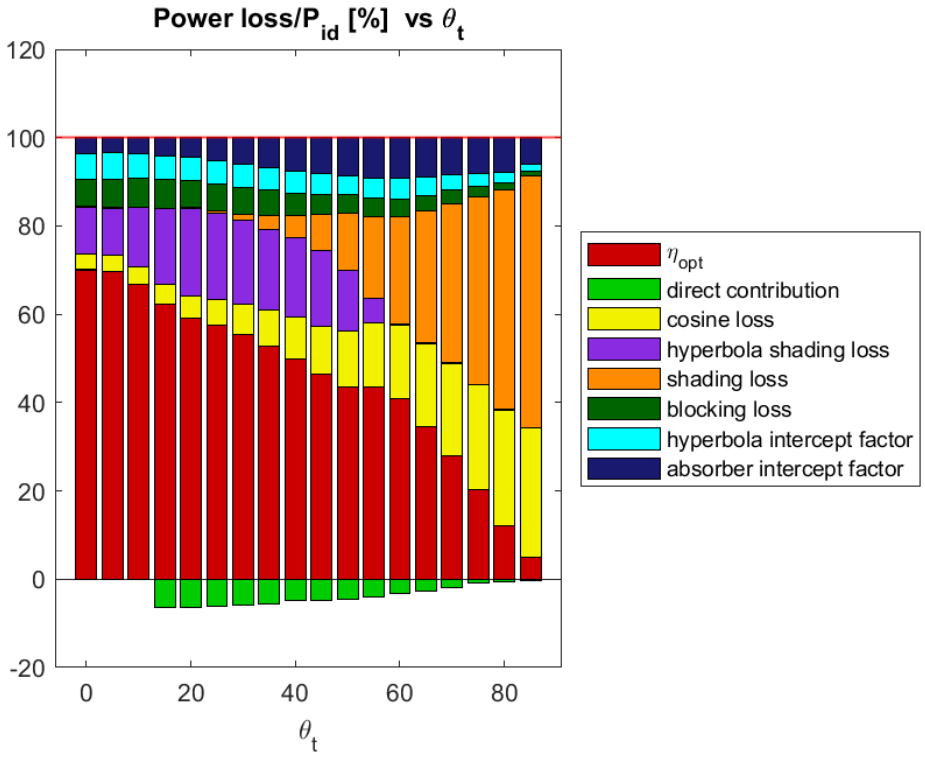

Figure 5-14 Percentage power losses on the ideal power as function of θ_t.

This plot is useful to understand on which source of loss of optical efficiency to act. It becomes clear that, for a noon-optimized configuration, the shading loss will be the most important loss entry. To reduce it the spacing between the mirror can be increased, keeping in mind that this will increase the losses for cosine effect as the mirrors will move further away from the z-axis.

5.4.2 Equinox day comparison

To perform this test, the longitudinal length of absorber and hyperbolic cylinder must be adjusted to be able to intercept rays that also have a longitudinal component. For each position of the sun analysed the longitudinal length of these components is set so that no end-loss occurs, as the same was true for the transversal plane test.

The comparison is carried out at the equinox day with solar time ranging from 6:20 AM to 12:00 AM in twenty minutes time steps. It is important to remember that in the early hours of the morning the transversal angle is at its greatest while it declines as the sun approaches midday. The opposite is true for the longitudinal angle.

The sun vector considered to apply the geometric method is the projection of the three-dimensional sun vector on the transversal plane.

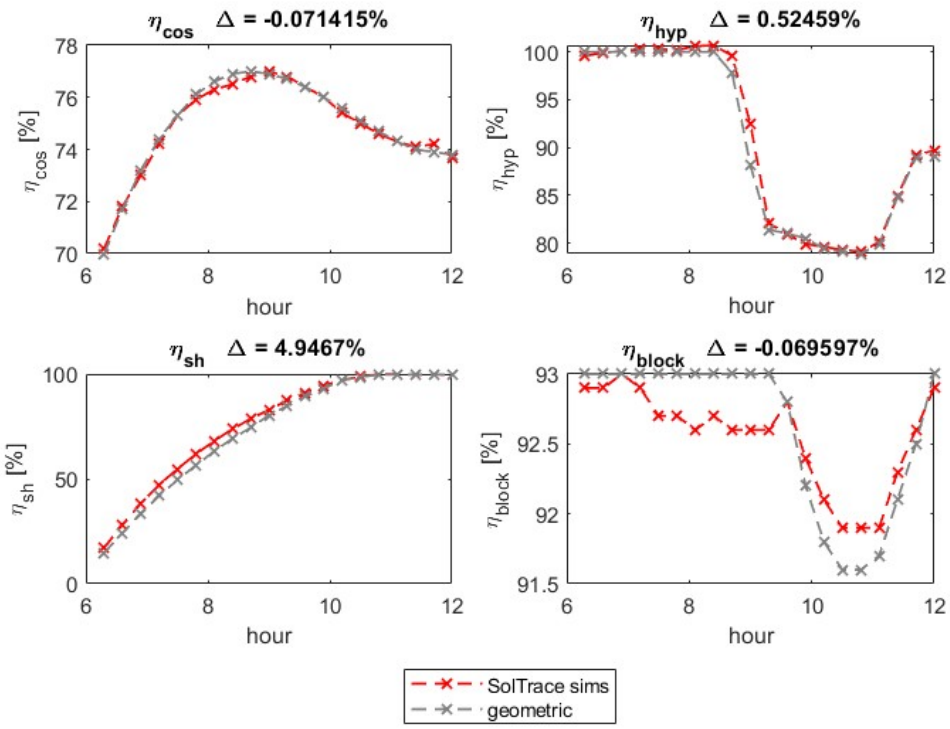

Figure 5-15 Comparison between the cosine, hyperbola shading, shading, and blocking efficiencies computed with the geometric method and with the SolTrace simulations obtained at the equinox day for a latitude of 40°N.

The behaviour of the cosine efficiency is quite different from the one obtained in the previous test, even if the two methods are in accordance. The cosine efficiency as the sun rises is very low due to the large transversal incidence angle of the sun. As the sun rises on the horizon, the cosine effect is reduced like in the transversal plane test. However here the curve reaches a maximum at around 9 AM to then fall again. Simultaneously, the longitudinal incidence angle of the sun vector increases and eventually, becomes the main actor in the determination of the cosine loss. As a result, the cosine efficiency at noon is not maximum. The cosine efficiency for the geometric method considers the incidence angle existing between the solar vector and the mirror normal according to the method defined in Chapter 5.1.1.

The general trend of the hyperbola shading loss is confirmed for both methods. The difference between the two curves is greater than the one in the previous test but still acceptable.

The first real discord between the two methods can be seen in the shading loss. While the trend is the same, the geometric method tends to underestimate the efficiency. This can be explained by looking at the view of the mirror field from above in Figure 5-16. The L-shaped mirrors are characterized by a three-dimensional shading pattern that cannot be rendered with the geometric method: the mirror area delimited by the points P and R_i in Figure 5-5 is considered shaded for the entire longitudinal length of the mirror while this may not actually be the case. Hence the overestimation of the shading loss by the geometrical method.

The blocking efficiency is slightly affected by the 3D path of the rays as well but given the range spun by the curve is small, the differences are still small. The general behaviour is the same of the previous analysis and the absence of blocking at midday is confirmed.

As for the intercept factors, their values increase as the sun moves towards the noon position. The underestimation of the geometric method is probably due to the value of $P_{after\ block}$ in input, miscalculated for the error on the shading efficiency.

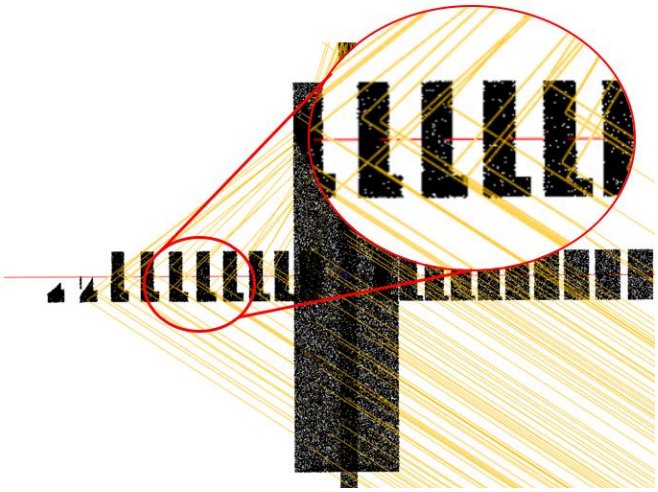

Figure 5-16 View from above of the BDLFR system.

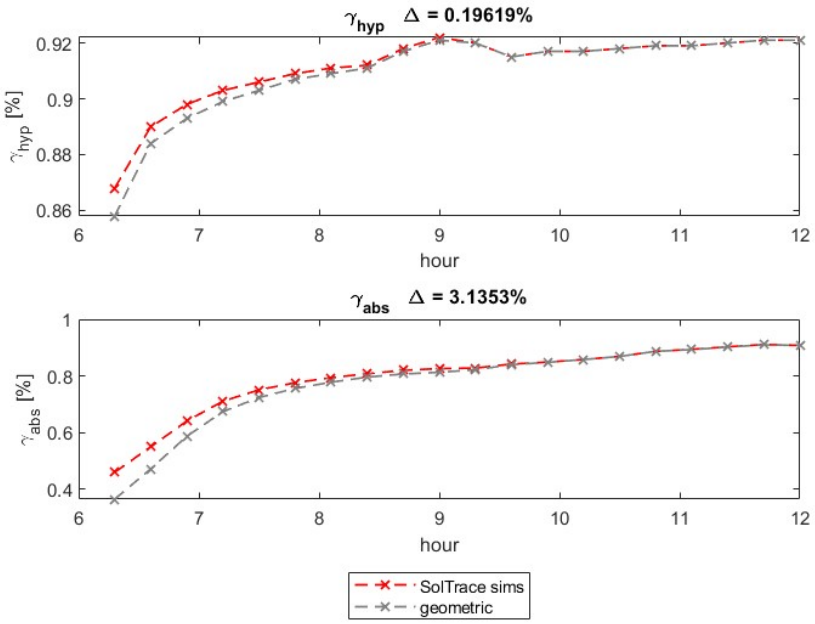

Figure 5-17 Comparison between the hyperbola and absorber intercept factors computed with the geometric method and with the SolTrace simulations obtained at the equinox day for a latitude of 40°N.

As for the transversal plane analysis, the value of the optical efficiency computed with both methods is compared with the one obtained from the direct measurement of the power impinging on the absorber.

In this case the SolTrace simulations method is clearly the best way to compute the different losses of the system, while the geometric method falls short especially during the early hours of the morning due to effects described commenting the shading loss.

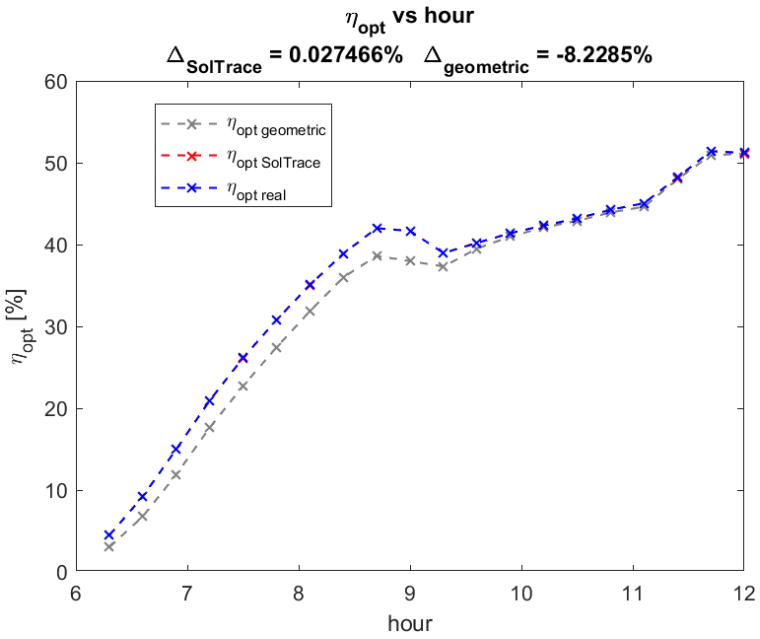

Figure 5-18 Comparison between the total efficiencies' values computed with the SolTrace simulation method, geometric method and direct method obtained at the equinox day for a latitude of 40°N.

The optical efficiency presents a maximum at noon with a value little over 50% to then reach a average value of 40% between 11:00 AM and 8:00 AM. Before this time the efficiency of the system is very low.

The power losses computed with the three-dimensional simulation follow the same trends already commented for the previous analysis. The main difference is the presence of a greater percentage of direct radiation due to the longer absorber needed to intercept the sun rays.

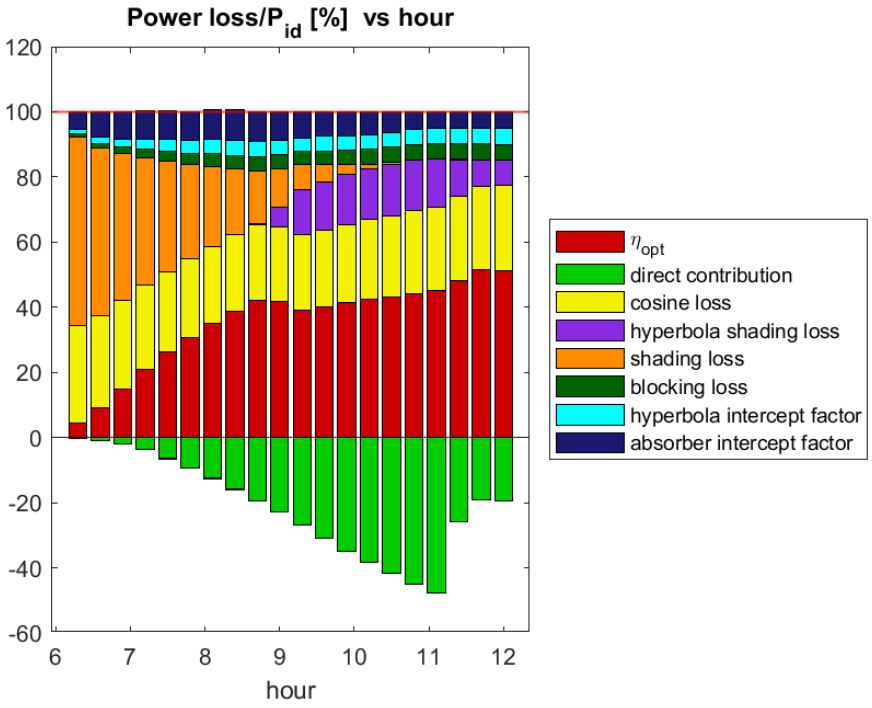

Figure 5-19 Percentage power losses on the ideal power as function of the solar hour.

5.5 Daily and annual optical efficiency of the system

The efficiency computed in Chapter 5.3 is only an instantaneous efficiency, meaning evaluated when the sun in a certain position in the sky. This value, as the values of all the different efficiencies described in the previous Chapter, varies widely with the sun position in the sky.
It is useful to have a tool to determine the performance of a system and to be able to compare it to others. For this reason, the definition of daily and annual efficiency of a system are introduced.

The daily efficiency is defined as the ration between the total energy collected on the absorber (without considering the direct contribution) and the total energy available to the system during the day-light hours of the selected day. Day-light hours are those for which the zenith angle is lower than 90°. This efficiency can be mathematically expressed as:

$$\eta_{day}^{opt} = \frac{\int_{\theta_z<90^\circ} P(h) \cdot dh}{\int_{\theta_z<90^\circ} P_{id}(h) \cdot dh} \tag{5.47}$$

Similarly, the annual efficiency of a system can be defined as the ratio between the total energy collected by the absorber and the total energy available to the system:

$$\eta_{year}^{opt} = \frac{\sum_1^{365} \int_{\theta_z<90^\circ} P(h) \cdot dh}{\sum_1^{365} \int_{\theta_z<90^\circ} P_{id}(h) \cdot dh} \tag{5.48}$$

While it is possible to compute the exact time at which the sun rises over the horizon line, a discretization of the day is introduced and the first time-step for which the day-time condition is met will be the first for which the computation of the efficiencies will be meaningful. Considering a smaller time step is always possible and it would be beneficial to the accuracy of the analysis; smaller time-steps however imply a

higher number of simulations. It follows that a practical choice of time-step must be taken, without compromising the precision of the calculation. For the evaluation of daily and annual efficiencies a time step of 0.3 hours (18 minutes) is adopted. Equations (5.47) and (5.48) are then rewritten as:

$$\eta_{day}^{opt} = \frac{\sum_{h:\,\theta_z(h)<90^\circ}^{h=12} P(h) \cdot dh}{\sum_{h:\,\theta_z(h)<90^\circ}^{h=12} P_{id}(h) \cdot dh} \tag{5.49}$$

$$\eta_{year}^{opt} = \frac{\sum_{1}^{365} \sum_{h:\,\theta_z(h)<90^\circ}^{h=12} P(h) \cdot dh}{\sum_{1}^{365} \sum_{h:\,\theta_z(h)<90^\circ}^{h=12} P_{id}(h) \cdot dh} \tag{5.50}$$

In both Equations (5.49) and (5.50), the ideal power at denominator is function of the solar hour through the following definition:

$$P_{id}(h) = DNI(h) * w_m * L_{field} * N_m \tag{5.51}$$

where the value of the DNI is obtained from the Clear Sky Model described in Chapter 5.5.1.

By considering a variable DNI, the daily and annual efficiencies are more correctly described as the value of direct normal irradiance varies a lot from morning to noon.

Considering that for each day-time time-step at least one simulation is required, it becomes clear that this definition of the annual efficiency of the system is not practical since it would require as large number of simulations for each configuration of the system analysed.
A method to overcome this issue is developed in Chapter 6.

5.5.1 Clear Sky Model

To increase the accuracy of the results, the Clear Sky Model (CSM) for the hourly variation of the Direct Norma Irradiation (DNI) is introduced.

This simple model, developed by Meinel and Meinel (1976)[13], first defines the extra-terrestrial radiation available depending on the day of the year as:

$$DNI_0 = 1367.7 \left(1 + 0.033 \cos\left(\frac{2\pi D}{365}\right)\right) \quad \left[\frac{W}{m^2}\right] \tag{5.52}$$

Then it defines the air mass coefficient as:

$$AM = \frac{1}{\cos(\theta_z)} \tag{5.53}$$

The air mass coefficient accounts for the fraction of atmosphere the light has to travel through to arrive to the ground: the greater the zenith angle, the longer the path of the light though the atmosphere and, consequently, the higher the attenuation due to scattering, reflection and absorption by the molecules of air.
The final radiation arriving on the ground is evaluated as:

$$DNI = DNI_0 \; 0.7^{AM^{0.678}} \tag{5.54}$$

The annual behaviour of the extra-terrestrial solar radiation is shown in Figure 5-20.

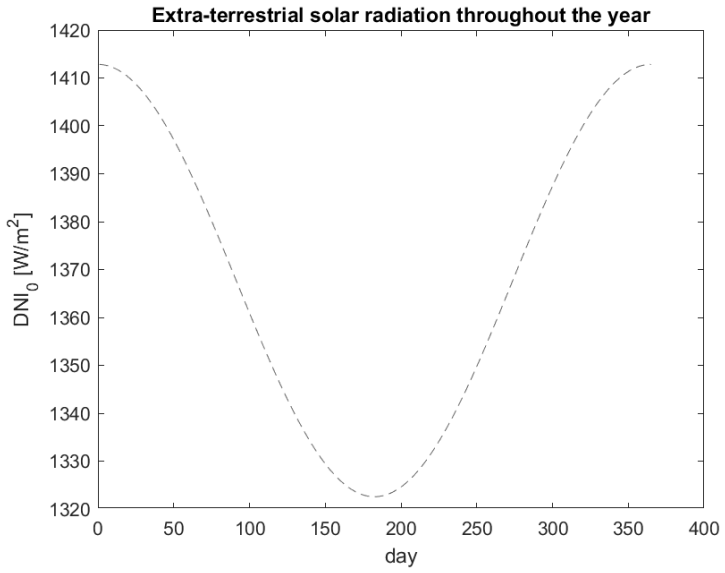

Figure 5-20 Extra-terrestrial solar radiation as function of the day of the year.

Considering the daily behaviour of the zenith angle for a latitude of 40°N in the days of spring and autumn equinox as well as summer and winter solstice shown in Figure 5-21(a), the values of DNI obtained are shown in Figure 5-21(b). Since the zenith curve for the days of the equinox is the same, the slight difference between their DNI curve is given by the extra-terrestrial solar radiation. For the calculations in the next Chapters, the DNI curve of the spring equinox will be considered.

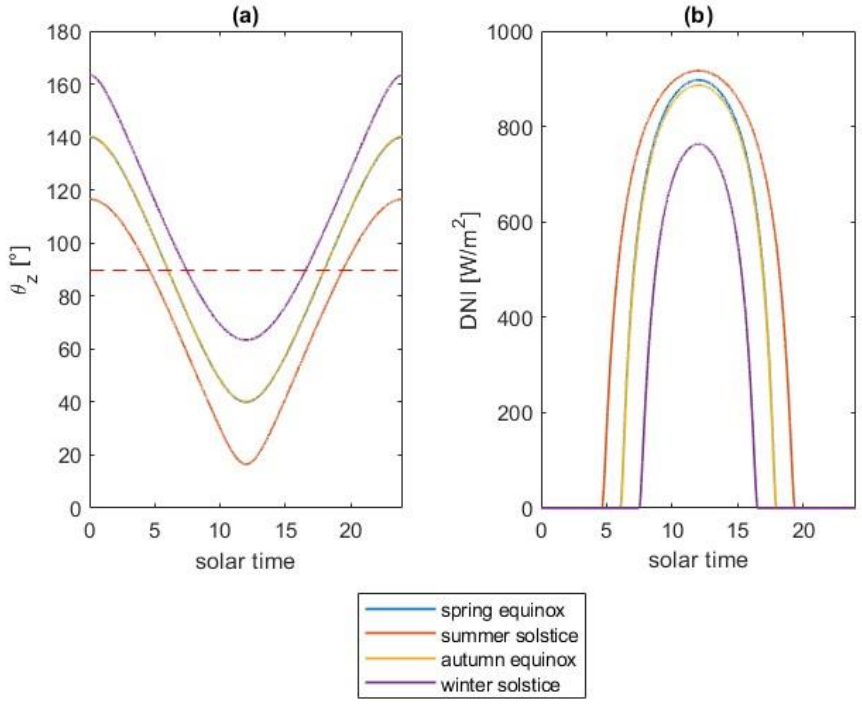

Figure 5-21 (a): zenith angle as function of solar time for the days of solstice and equinox. (b): Direct Normal Irradiation as function of solar time for the days of solstice and equinox. Both plots are obtained for a latitude of 40°N.

6 IAM curves

In the previous Chapter the total efficiency of the system was broken down into a series contributing factors. This is particularly interesting when the main cause of efficiency loss must be evaluated, but it is time-consuming when a large set of sun positions must be analysed, since the SolTrace simulations method requires five simulations to compute all the losses and finally the total or optical efficiency of the system.

It is always possible to compute with one simulation the optical efficiency of the system directly counting the number of hits on the absorber, multiplying by the power-per-ray and then comparing it to the ideal power collected by the mirror field. Even if this is undoubtedly a faster method to determine the efficiency of the system, it is still too time-inefficient when we want, for example, to compute the efficiency in every day-light hour of the year. Since there are 8760 hours in a year and about half of these (depending on the latitude) are of day-light, this method still requires a too large number of simulations.

A faster method to estimate the efficiency, given a certain position of the sun, is to introduce the concept of Incidence Angle Modifier (IAM). The Incidence Angle Modifier is a factor that accounts for all the sources of loss discussed in Chapter 5, condensing them in only one value.

6.1 IAM curves principle and factorisation

The principle of the procedure is to introduce a factor, IAM factor, function of both azimuth and zenith angles, defined as:

$$IAM(\theta_z, \gamma_s) = \frac{\eta(\theta_z, \gamma_s)}{\eta_z} \tag{6.1}$$

where $\eta_z = \eta(\theta_z = 0, \gamma_s = 0)$. η_z represents the efficiency of the system when the sun is in the zenith position. This value can be easily obtained with only one simulation. Once the value of the incidence angle modifier is known for every couple of azimuth and zenith angles the knowledge of the optical efficiency of the system is reduced to the knowledge of the zenith efficiency.

If the IAM is so defined, a wide set of simulations is required to know its value in all the possible couples of θ_z and γ_s. Instead, it would be more practical to use the factorisation of the incidence angle modifier as proposed by McIntire [16]. In Chapter 1.3 is shown how the position of the sun in the sky can be also given in terms of transversal and longitudinal incidence angles. Equation (6.1) can then be rewritten as:

$$IAM(\theta_z, \gamma_s) = IAM(\theta_t, \theta_l) = \frac{\eta(\theta_t, \theta_l)}{\eta_z} \tag{6.2}$$

When the IAM is function of two incidence angles, as it happens in BDLFR systems, McIntire proposes to estimate it for a certain couple of longitudinal and transversal incidence angles as:

$$IAM(\theta_t, \theta_l) \simeq IAM_t(\theta_t, 0)\, IAM_l(0, \theta_l) = \frac{\eta(\theta_t, 0)}{\eta_z} \cdot \frac{\eta(0, \theta_l)}{\eta_z} \tag{6.3}$$

With this factorisation, the knowledge of $IAM(\theta_t, \theta_l)$ is reduced to the knowledge of IAM_t and IAM_l that can be obtained with simulations, respectively, only on the North-South and East-West planes to evaluate the optical efficiency of the system.

When the case of LFR systems is analysed, literature reports different methods of estimation of the IAM. Some, like Balaji S. et al. [17] use a factorisation method as described by McIntire. Others, like Giostri et al. [5], use a factorisation based on the incidence angle θ_i instead of θ_l. In the following analysis the second approach will be used as in produces more accurate results.

IAM_t can be obtained with a series of simulations in which the sun is put on the transversal plane and then varying the transversal incidence angle from 0 up to 90.
IAM_i is obtained through a similar procedure by moving the sun in the longitudinal plane (when $\theta_t = 0$, $\theta_i = \theta_l$) varying the θ_i from 0° up to a suitable value depending on the latitude of the system.
An example of the resulting curves is shown in Figure 6-1.

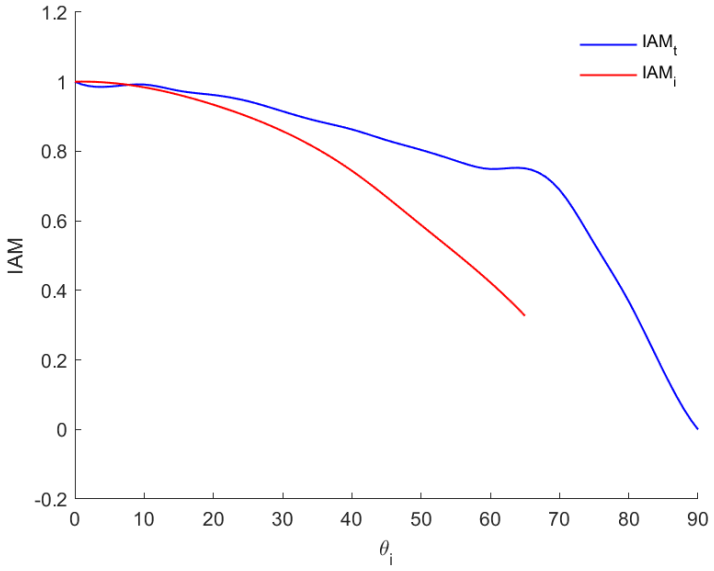

Figure 6-1 Shape of the curves IAM_t and IAM_i as function of the incidence angle θ_i obtained from the configuration defined in Table 6-1.

Number of mirror rows, Nr	10
Primary focus height, h [m]	5.5
Hyperbola shape factor, f	0.8
Mirror spacing [m]	1
Focal length	Slant range of the mirror

Table 6-1 Principal geometric parameters of the configuration for which the results in this Chapter are shown.

6.2 Correction coefficient for factorisation procedure

The factorisation is, however, source of error when evaluating either the daily efficiency or, more pronouncedly, the annual efficiency of the system. Some losses, such as shading or intercept factor on the absorber, are not well represented only with simulations on the two symmetry planes (see Chapter 5.4) of the system but require analysis in intermediate positions as well.

The simulations are carried out by setting the sun in a position defined by both angles θ_t and θ_i so that a matrix of positions is formed: first, for a certain value of θ_t, all the possible values of θ_i are spanned, and then θ_t is increased to the next value. In each position the IAM is evaluated (IAM_{matrix}).

The result is a IAM surface, function of both angles. In each position simulated, the value of the IAM is the real one, not the result of any kind of approximation nor estimation.

Once IAM_{matrix} is known, the first row and the first column will represent the values of IAM_t and IAM_i. It is then possible to compute the efficiency surface obtained via factorisation (IAM_{fact}) according to equation (6.3).

The two surfaces in Figure 6-2 show substantial differences especially for high values of both θ_t and θ_i.

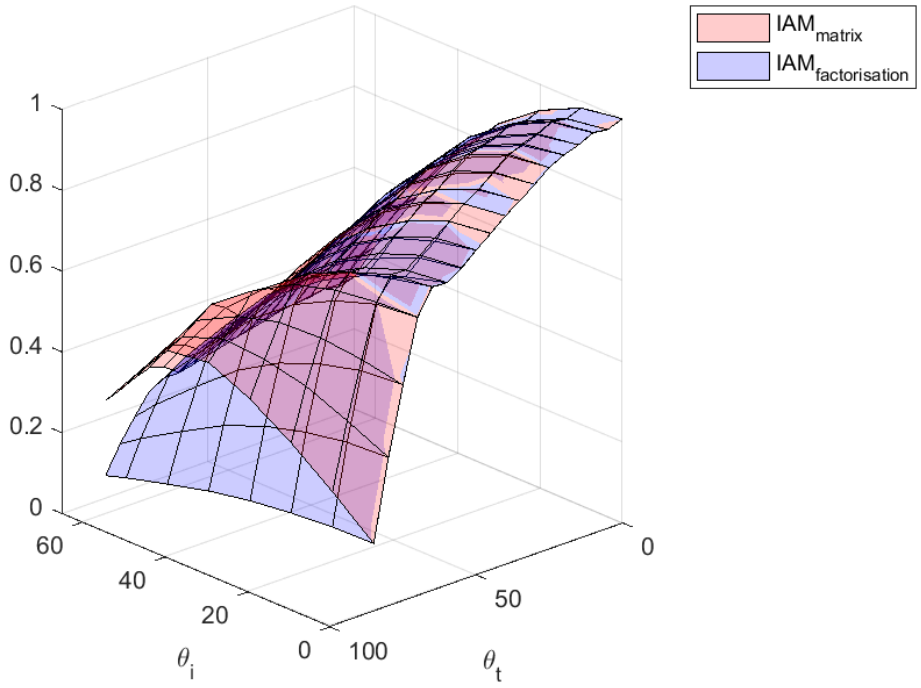

Figure 6-2 IAM surfaces obtained with direct simulation and with factorisation obtained from the configuration defined in Table 6-1.

It is important to remember that not all the points of the surfaces will be active in the definition of the annual efficiency: the sun only occupies some positions in the hemisphere over the system in the arc of the year.

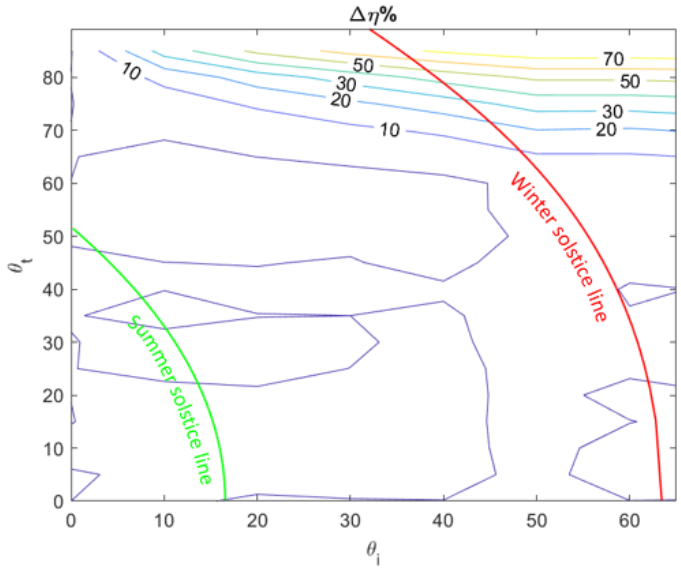

Figure 6-3 Error on the estimation of the efficiency with the factorisation with respect to the real efficiency resulting from simulation obtained from the configuration defined in *Table 6-1*.

The red line in Figure 6-3 represents the couples (θ_t, θ_i) that describe the position of the sun from dawn till noon on the winter solstice, the green one the trajectory of the sun on summer solstice. The region outlined by the two lines describes all the positions of the sun, in terms of (θ_t, θ_i) couples, during the year. Even if the two IAM surfaces don't coincide outside this region, the value of annual efficiency will not be affected. However, it can be seen how the error on the estimation of the efficiency for high values of θ_t is very high (up to 50%). It is necessary, then, to introduce a correction coefficient to correctly estimate the efficiency in this region.

The correction coefficient for the factorisation is defined as:

$$F(\theta_t, \theta_i) = \frac{IAM_{matrix}(\theta_t, \theta_i)}{IAM_{fact}(\theta_t, \theta_i)} = \frac{\eta_{matrix}(\theta_t, \theta_i)}{\eta_{fact}(\theta_t, \theta_i)} \tag{6.4}$$

If a correction coefficient, common to a set of configurations, is known, it allows to bypass the matrix of simulations needed to obtain either η_{matrix} or IAM_{matrix}. In fact, combining equations (6.2) to (6.4):

$$\eta(\theta_t, \theta_i) = \eta_z * IAM(\theta_t, \theta_i) = \eta_z * IAM_t(\theta_t, 0) * IAM_i(0, \theta_i) * F(\theta_t, \theta_i) \tag{6.5}$$

Thus computing the efficiency, only the simulations for IAM_t and IAM_i are required, saving again more computational time.

It is now necessary to determine a correction factor valid for as large category of configurations as possible. To do so a test configuration must be defined by selecting the main geometrical parameters such as number of mirror rows, mirror spacing, focal length and hyperbola shape factor. The selected parameters are the ones listed in *Table 6-1*.

The shape of the correction factor obtained for this test configuration is shown in Figure 6-4. As expected from the scatter plot of the error shown in Figure 6-3, the correction coefficient is greater for the region of elevated values of θ_t.

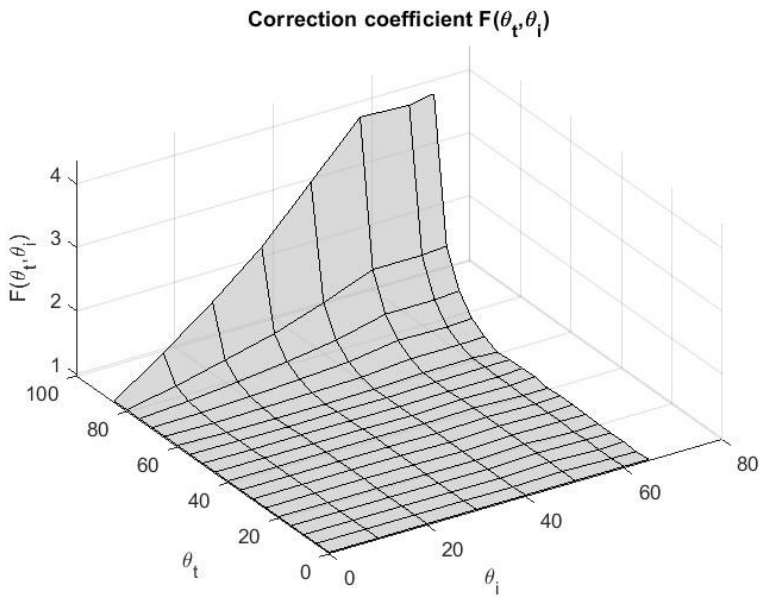

Figure 6-4 Correction coefficient for the test configuration in Table 6-1 as function of θ_t and θ_i.

6.2.1 Dependence of F from mirror spacing

Now that the test configuration has been defined, the mirror spacing parameter is changed to determine if the correction factor computed for the test configuration also reduces the error committed on the estimation of the daily efficiency on the other spacing options. The comparison is carried out for both the daily and annual optical efficiency.

The value of the daily efficiency considered as reference is the one obtained by direct SolTrace simulation with the parameters described in Chapter 5.5 since this will be its accurate evaluation. This value is then compared with the daily efficiency computed via interpolation of the IAM surface (IAM_{matrix}) for the couples (θ_t, θ_i) that describe the position of the sun in the time-steps analysed and the ones obtained by the factorisation of the IAM with ($IAM_{fact} + F$) and without correction coefficient (IAM_{fact}).

The error is computed based on the value obtained by the SolTrace simulation as:

$$\Delta^{day} = \frac{\eta - \eta_{SolTrace}}{\eta_{SolTrace}} \cdot 100 \tag{6.6}$$

For the annual efficiency, as discussed previously in this Chapter, it is too time consuming to extract a value through direct SolTrace simulation. It is then adopted as reference the one obtained via the interpolation of the IAM surface.

The different options considered are: constant mirror spacings of 0.5, 1.5, 2 meters and the noon-optimized spacing discussed in Chapter 3.3. Please notice that only the mirror spacing and consequent width of the hyperbola and absorber have been changed while the hyperbola shape factor, the primary focus point height, the number of mirrors and the focal length of the mirrors are the same of the test configuration.

The results of this comparison are shown in Table 6-2. Firstly, it can be observed that the value of daily efficiency of the noon-optimized configuration are considerably lower than almost all other configurations apart from the 0.5 one. The reason behind this will be described more in detail in the following Chapters.

	Spacing option				
η_{day}^{opt} [%]	0.5	1	1.5	2	noon-optimized
SolTrace simulation	36.9360	44.6884	47.1696	47.6206	39.3875
IAM_{matrix} interp.	36.8914	44.6641	46.9829	47.5362	39.1228
$\Delta\, IAM_{matrix}$ interp. [%]	-0.1208	-0.0546	-0.3958	-0.1771	-0.6718
IAM_{fact}	36.2161	44.6301	46.9409	47.1988	38.1579
$\Delta IAM_{fact.}$ [%]	-1.9491	-0.1306	-0.4849	-0.8857	-3.1216
$IAM_{fact} + F$	36.0916	44.6529	47.0890	47.3873	38.0382
$\Delta IAM_{fact} + F$ [%]	-2.2862	-0.0796	-0.1708	-0.4899	-3.4257

Table 6-2 Daily optical efficiency computed for different spacing options.

The error introduced by the factorisation can reach values of more than 3% (-3.1216% for the noon optimized configuration). This proves that the introduction of the correction coefficient is needed.
Such introduction is beneficial for the spacing of 1.5, given that the error decreases from -0.4849% to -0.1708% that is about the order of magnitude of the one introduced by the interpolation of the IAM surface. The value for the configuration with spacing equal to 2 also benefits from the application of the correction coefficient but in smaller measure.

The correction coefficient is instead detrimental to the accuracy of the noon-optimized configuration and the one with spacing equal to 0.5. This happens because the IAM curves of these last two configurations differ in larger measure from the test one then the ones of constant spacing 1.5 and 2.

The correction coefficient seems to be a function of the mirrors spacing.

6.2.2 Dependence of F from focal length

Similarly to what has been done in the previous Chapter, now only the focal length of the different mirrors is changed while keeping constant all the other parameters, mirror spacing included. The different focal length options are the ones mentioned in Chapter 4.5.

	Focal length options			
η_{day}^{opt} [%]	Slant range	optimized	constant	flat
SolTrace simulation	44.6884	42.6735	40.6712	14.3767
IAM_{matrix} interp.	44.6641	42.5403	40.5016	14.3544
$\Delta\, IAM_{matrix}$ interp. [%]	-0.0546	-0.3123	-0.4171	-0.1550
IAM_{fact}	44.6301	42.3597	40.3774	14.64

$\boldsymbol{\Delta IAM_{fact.}}$ [%]	-0.1306	-0.7354	-0.7224	1.8308
$\boldsymbol{IAM_{fact} + F}$	44.6529	42.4286	40.4392	14.6932
$\boldsymbol{\Delta IAM_{fact} + F}$ [%]	-0.0796	-0.5740	-0.5704	2.2015

Table 6-3 Daily optical efficiency computed for different focal length options.

From the results shown in Table 6-3, it can be deduced that the correction coefficient has a positive effect on the accuracy of the daily optical efficiency of all focal length, reducing their error. The exception is the configurations with flat mirrors: again, the configuration with an IAM curve shape much different from the others doesn't respond well to the introduction of the correction coefficient.

This becomes even more evident if the annual optical efficiency is analysed. The reference value on which the error is evaluated cannot be the result of a SolTrace simulation, as previously explained in this Chapter. The reference value will be the one obtained from the interpolation of the IAM surface IAM_{matrix} that showed very small errors in the evaluation of the daily optical efficiency (Table 6-2 and Table 6-3).
The error will then be evaluated as:

$$\Delta^{year} = \frac{\eta - \eta_{matrix}}{\eta_{matrix}} \, 100 \tag{6.7}$$

	Focal length options			
$\boldsymbol{\eta_{year}^{opt}}$ [%]	Slant range	optimized	constant	flat
$\boldsymbol{IAM_{matrix}}$ interp.	44.8510	42.7521	40.7348	14.4936
$\boldsymbol{IAM_{fact}}$	44.0765	41.8488	40.6006	14.5453
$\boldsymbol{\Delta IAM_{fact.}}$ [%]	-1.7268	-2.1129	-2.1271	0.3568
$\boldsymbol{IAM_{fact} + F}$	44.8450	42.6954	40.6688	14.8772
$\boldsymbol{\Delta IAM_{fact} + F}$ [%]	-0.0133	-0.1326	-0.1622	2.6471

Table 6-4 Annual optical efficiency for different focal length options.

The effect of the correction coefficient becomes much more relevant on annual basis, reducing the error by an order of magnitude for all the configurations except for the one with flat mirrors.

It can be deduced that, except for the flat mirror configuration, the correction factor is not a function of the focal length of the configuration as long as the mirror position and all other geometrical parameters remain constant.
The exception of the flat mirror configuration doesn't represent a problem as both values of daily and annual optical efficiency are considerably lower than all other configurations and therefore to be excluded a priori in the selection of the optimal configuration.

7 Simplified thermal model

The thermal model describes the radiative loss from the absorber to the environment.
The radiative power exchanged is computed as:

$$\dot{Q}_{loss} = \sigma \varepsilon_{abs} S_{abs} (T_{abs}^4 - T_a^4) \quad [W] \tag{7.1}$$

where $\sigma = 5.670367\ 10^{-8}\ \left[\frac{W}{m^2 K^4}\right]$ is the Stefan-Boltzmann constant and $T_a = 20°C$ is the ambient temperature. The remining symbols in the formula are referred to the absorber: S_{abs} is the exchange area of the absorber, $\varepsilon_{abs} = 0.2$ is the value of its global emissivity and T_{abs} its temperature.

The exchange area of the absorber depends on its shape. In this case, a cylindrical absorber will be used. The absorber is considered to be perfectly insulated in its lower side as shown in Figure 7-1. This way only the upper contributes to the radiative loss. The exchange area is then computed as:

$$S_{abs} = \frac{\pi w_{abs} L_{abs}}{2}\ [m^2] \tag{7.2}$$

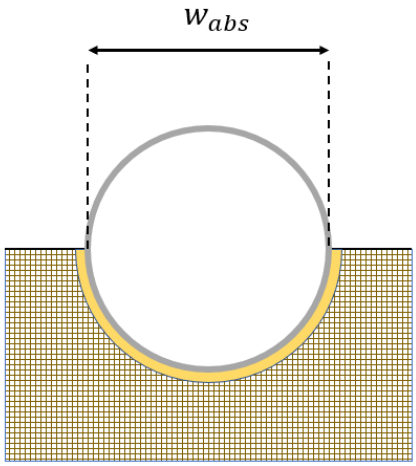

Figure 7-1 Absorber structure. View of the cross-sectional area.

Substituting equation (7.2) in (7.1) the following expression for the radiative loss is obtained:

$$\dot{Q}_{loss} = \frac{\sigma \varepsilon_{abs} \pi w_{abs} L_{abs} (T_{abs}^4 - T_a^4)}{2} \quad [W] \tag{7.3}$$

As equation (7.3) suggests, the value of the radiative loss is function of the absorber length. The absorber is fixed on the ground and, as the sun moves from East to noon position, the image of the mirror field moves northward. If the length of the mirror field is so that the end-losses can be neglected, then also the active length of the absorber (i.e., longitudinal length intersected by the rays reflected by the mirror field) will roughly coincide with the longitudinal length of the mirror field. It follows that:

$$\frac{L_{abs}}{L_{field}} = 1 \tag{7.4}$$

7.1 Power balance

The power balance on the absorber is derived considering the scheme in Figure 7-2.

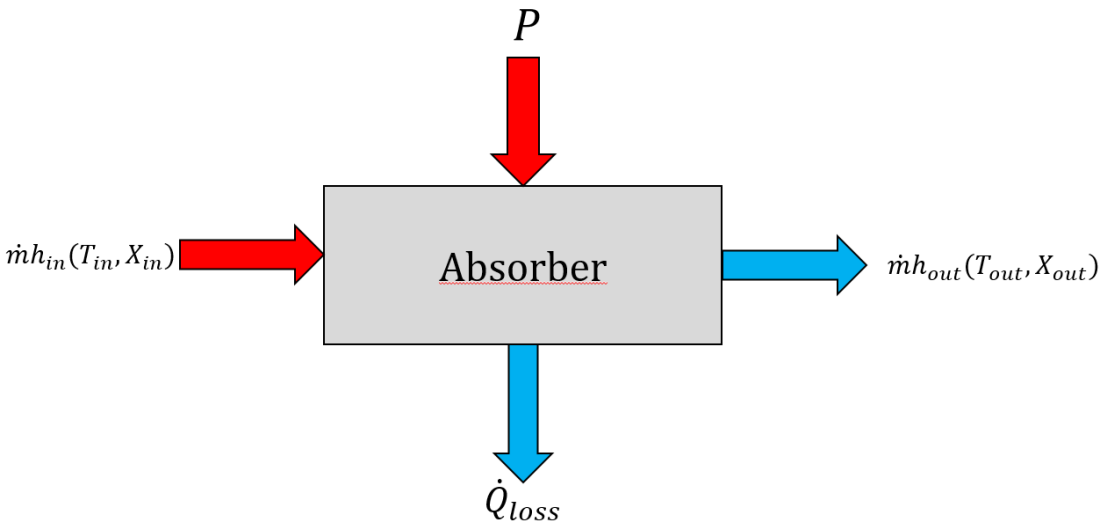

Figure 7-2 Power balance on the absorber for a generic process.

This scheme is valid for any thermal or chemical process: $\dot{m}$ is the total mass flow rate of the inlet stream (sum of the single components in case of a multi component stream) and, since no nuclear reactions are considered, it coincides with the total mass flow rate of the outlet stream. The inlet and outlet enthalpies (specific to the mass) are function of both temperature and chemical composition of the streams.

The resulting power balance is given by:

$$\dot{m}h_{in}(T_{in}, X_{in}) + P = \dot{Q}_{loss} + \dot{m}h_{out}(T_{out}, X_{out}) \tag{7.5}$$

where P is the power impinging on the absorber.

It is useful to introduce the definition of useful power as:

$$\dot{Q}_u = \dot{m}h_{out}(T_{out}, X_{out}) - \dot{m}h_{in}(T_{in}, X_{in}) \tag{7.6}$$

so that it becomes possible to rewrite equation (7.4) as:

$$P = \dot{Q}_{loss} + \dot{Q}_u \tag{7.7}$$

Once the incoming power from the solar field is known (using the IAM curves developed in Chapter 6 or directly through SolTrace simulation) some assumptions are necessary to compute the useful power of the system.

The absorber is assumed to operate at a fixed temperature designated as target temperature ($\overline{T}$), considered constant along the longitudinal direction. The target temperature must be chosen taking into account the typical operating temperatures of the process in question, considering both the kinetics of the chemical and physical reactions that may take place into the absorber and the desired composition at the outlet. By selecting a low temperature to contain the radiative losses, the process may require a too long an absorber to be of practical interest as the residence time increases due to the slower reaction kinetics;

on the other hand, if the target temperature is too high, this may compromise the chemical composition of the outlet stream, favouring the production of unwanted by-products (e.g. in the pyrolysis process for syngas generation the increase of operating temperature generates an increase of production of bio-oil to the detriment of the syngas mass fraction)

The corresponding radiative loss is evaluated through equation (7.3) and designated as target radiative loss ($\overline{\dot{Q}_{loss}}$).

Like the operating temperature, also the length of the absorber must be defined thinking of the underlying process: mass flow rate and length of the absorber have to be designed so that the required outlet chemical composition can be achieved in the least favourable condition of the day (adopting a conservative approach). The actual length of the absorber will vary from process to process. Since in the previous Chapter the equivalence between field and absorber longitudinal length has been established, the length of the mirror field will be chosen according to the process in question.

7.2 Power balance (specific to the longitudinal length of the mirror field)

It becomes then interesting to evaluate the efficiency of the system removing the influence of the longitudinal length of the system. To do this, both members of equation (7.7) can be divided for the longitudinal length of the mirror field L_{field}.

$$\frac{P}{L_{field}} = \frac{\dot{Q}_{loss}}{L_{field}} + \frac{\dot{Q}_u}{L_{field}} \qquad \left[\frac{W}{m_{long}}\right] \tag{7.8}$$

Inserting equation (7.3) in (7.8) and designating the quantities specific to the mirror field length with an apostrophe:

$$P' = \frac{\sigma \varepsilon_{abs} \pi w_{abs} (T_{abs}^4 - T_a^4)}{2} \left(\frac{L_{abs}}{L_{field}}\right) + \dot{Q}_u' \tag{7.9}$$

Since the value of $\frac{L_{abs}}{L_{field}}$ is set to 1 by equation (7.4), the new expression of the power balance for meter of mirror field is derived as:

$$P' = \frac{\sigma \varepsilon_{abs} \pi w_{abs} (T_{abs}^4 - T_a^4)}{2} + \dot{Q}_u' = \dot{Q}_{loss}' + \dot{Q}_u' \tag{7.10}$$

7.3 Control logic of the process

As already mentioned, the system is operated at a constant temperature called target temperature. This temperature sets the specific target radiative loss $\overline{\dot{Q}_{loss}}'$ as:

$$\overline{\dot{Q}_{loss}}' = \frac{\sigma \varepsilon_{abs} \pi w_{abs} \left(\overline{T}^4 - T_a^4\right)}{2} \tag{7.11}$$

The power supplied by the mirror field can be either lower than this specific target radiative loss or greater.

If the first case the plant is not operated: the inlet mass flow rate is null and so is the useful power that it receives. It follows that the useful power is null ($\dot{Q}'_u = 0$). Consequently, all the incoming power from the optical system will be exchanged with the environment and the absorber will assume a temperature lower than the target one. The absorber temperature in this case is derived setting the specific useful power to 0 in equation (7.10) as:

$$T_{abs} = \sqrt[4]{\frac{2P'}{\sigma \varepsilon_{abs} \pi w_{abs}} + T_a^4} \quad [K] \tag{7.12}$$

In the second case the plant is activated as it is able to operate at the required temperature. The specific useful power will be the difference between the specific input power and the specific target radiative loss:

$$\dot{Q}'_u = P' - \overline{\dot{Q}_{loss}}' = P' - \frac{\sigma \varepsilon_{abs} \pi w_{abs} \left(\overline{T}^4 - T_a^4\right)}{2} \tag{7.13}$$

The temperature of the absorber is then set at exactly the target temperature ($T_{abs} = \overline{T}$).

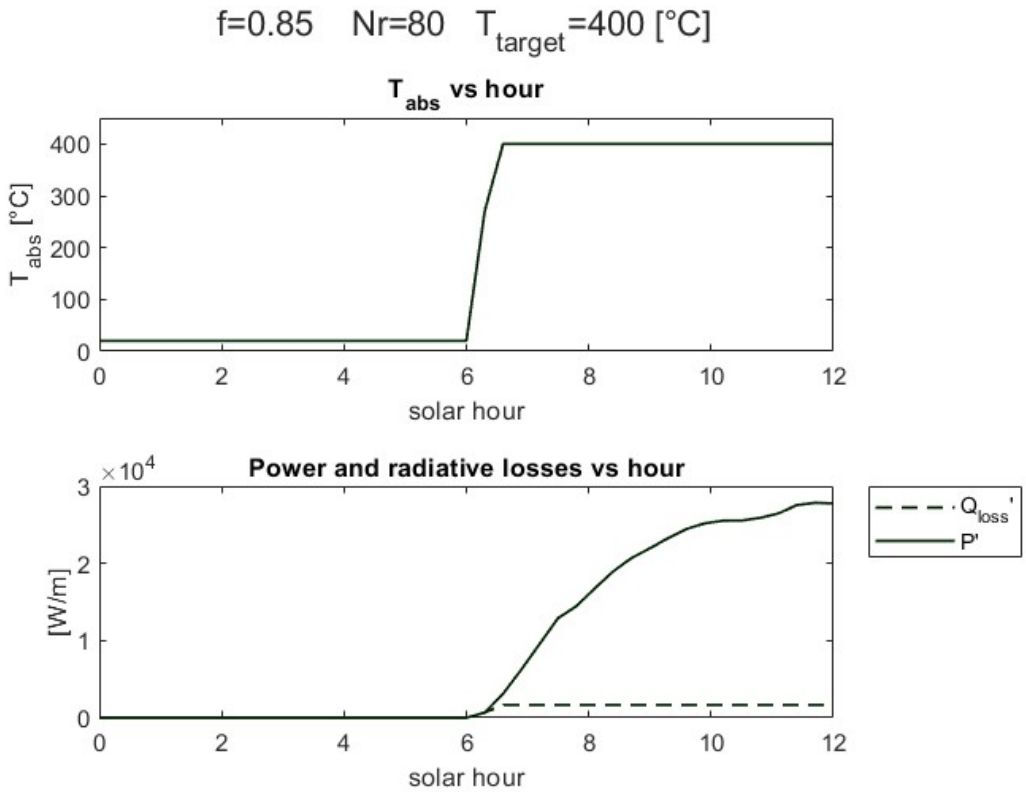

Figure 7-3 Control strategy results for a noon-optimized configuration with f=0.85, Nr=80, h=22.87 m and target temperature equal to 400°C.

Figure 7-3 show the specific power and power losses for a target temperature of 400°C. It is visible that for the first time-steps, the power provided by the mirror field wasn't enough to allow the operation of the system at the required temperature: power and power losses curve then coincide. As noon approaches, the power coming from the optical system increases and most of the power is transmitted to the underlying process.

If the target temperature where to increase, the specific power curve would remain the same while the specific power loss curve would rise and the process would be inactive for a longer period of time from the moment of sunrise decreasing the daily efficiency of the system as the energy conveyed by the optical system on the absorber in that period is just exchanged with the environment.

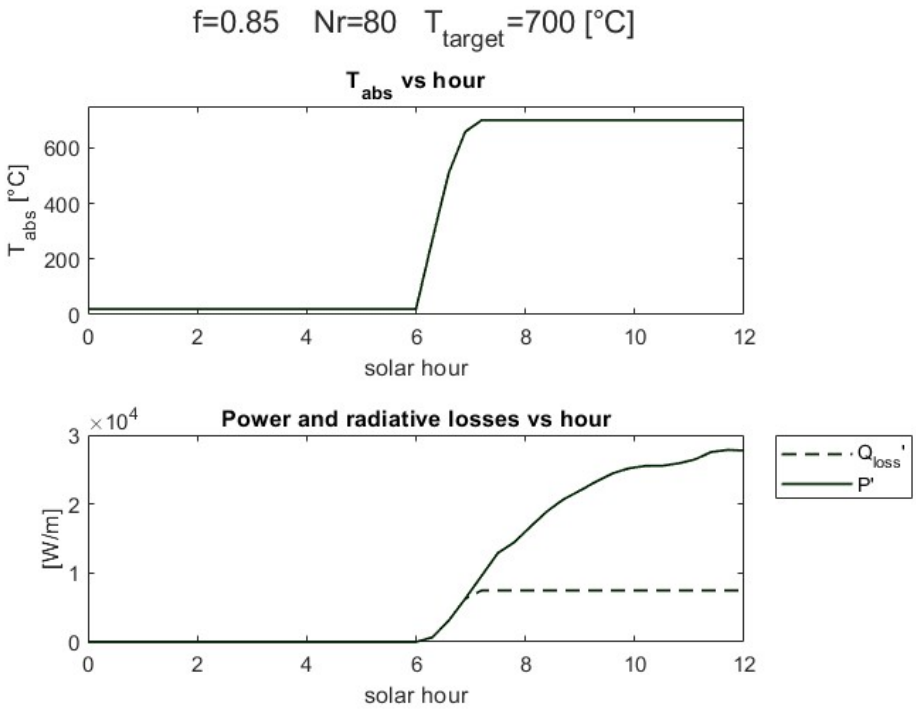

Figure 7-4 Control strategy results for a noon-optimized configuration with f=0.85, Nr=80, h=22.87 m and target temperature equal to 700°C.

7.4 Thermal and global efficiencies of the system

The thermal efficiency of the system, both daily and annual, are expressed analogously to the optical ones (the time discretization explained in Chapter 5.5 is directly introduced):

$$\eta_{day}^{th} = \frac{\sum_{h:\,\theta_z(h)<90^\circ}^{h=12} \dot{Q}_u(h) \cdot dh}{\sum_{h:\,\theta_z(h)<90^\circ}^{h=12} P(h) \cdot dh} \tag{7.14}$$

$$\eta_{year}^{th} = \frac{\sum_{1}^{365} \sum_{h:\,\theta_z(h)<90^\circ}^{h=12} \dot{Q}_u(h) \cdot dh}{\sum_{1}^{365} \sum_{h:\,\theta_z(h)<90^\circ}^{h=12} P(h) \cdot dh} \tag{7.15}$$

The quantities at nominator represent the amount of energy conveyed to the process, respectively in the day and in the year; the ones ad denominator the amount of energy conveyed on the absorber surface by the optical system.

The global efficiency of the system is given by the product of optical and thermal efficiencies:

$$\eta_{day}^{global} = \eta_{day}^{opt} \eta_{day}^{th} = \frac{\sum_{h:\,\theta_z(h)<90^\circ}^{h=12} \dot{Q}_u(h) \cdot dh}{\sum_{h:\,\theta_z(h)<90^\circ}^{h=12} P_{id}(h) \cdot dh} \tag{7.16}$$

$$\eta_{year}^{global} = \eta_{year}^{opt}\eta_{year}^{th} = \frac{\sum_{1}^{365}\sum_{h:\,\theta_z(h)<90^\circ}^{h=12}\dot{Q}_u(h)\cdot dh}{\sum_{1}^{365}\sum_{h:\,\theta_z(h)<90^\circ}^{h=12}P_{id}(h)\cdot dh} \tag{7.17}$$

Note that the value of the efficiencies is not affected by the use of powers specific to the longitudinal length of the mirror field.

8 Selection of optimal layout for a BDLFR system

The selection of the optimal (with noon-optimized mirror spacing) layout starts from the geometrical considerations reported in Chapters 3.4.1 and 3.4.2, meaning the optimal configuration is selected among those that minimize the absorber width. For all configurations the mirror width is equal to 0.5 m.

For different values of hyperbola shape factor ($f = 0.65 \div 0.95$), the number of mirror rows is changed in the range $Nr = 10 \div 80$. The primary focus height for every couple of (f, Nr) is chosen from the data set provided by the $h - Nr$ curves of Chapter 3.4.2 (*Figure 3-14*). Adopting this logic implies, as shown in *Figure 3-17*, moving the last mirror row further and further away as the number of mirror rows increases but contextually increasing the primary focus point height.
For all the configurations a CPC is adopted to further decrease the absorber surface according to the method and assumptions described in Chapter 3.5.

The procedure for the determination of the IAM curves correction coefficient here is time-ineffective, as the configurations differ for hyperbola shape factor and most importantly number of mirror rows. These two parameters in fact impact heavily on the average distance between mirrors: the first can determine a different position of the first mirror row, changing the position of all the following ones as it affects the absorber width; the second increases the distance of the mirrors since the more mirrors are present the further away from each other the last mirror rows will have to be to avoid blocking in the noon condition. As in Chapter 6.2.1 the dependence of the correction coefficient F for IAM curves from the mirror spacing was established, it results impossible to find a coefficient F common to all or a set of configurations.

The power output is then obtained directly through SolTrace simulations. The conditions of the simulations are the ones reported during the definition of the daily and annual optical efficiency (Chapter 5.5): the power reflected by the optical system on the absorber (the direct radiation impinging on the absorber is not considered) is evaluated for time intervals of 18 minutes from the moment the sun appears over the horizon on the day of the spring equinox. The values of the DNI are taken from the Clear Sky Model described in Chapter 5.5.1.

The results shown in *Figure 8-1* show how the optical daily efficiency reaches an asymptote between 30 and 40 mirror rows for all values of f. This is due to the beforementioned method for the selection of the primary focus height: as the number of rows increases and consequently the distance of the last mirror row, the primary focus height is increased, preventing the increment of shading and blocking losses in the initial hours of the day. The result is that, apart for small number of mirror rows, all the layouts are in a condition of “similitude” having almost the same optical daily efficiency while their actual geometry changes. The effect of the hyperbola shape factor is that of increasing the optical efficiency. This is due to the effect of the CPC: the difference between the absorbers’ widths is minimal after the introduction of the CPC which implies almost constant radiative losses for a certain Nr. Higher f implies smaller hyperbola width and so smaller hyperbola shading losses, especially at noon when the DNI value is at its maximum and it’s important to have a high instantaneous optical efficiency.

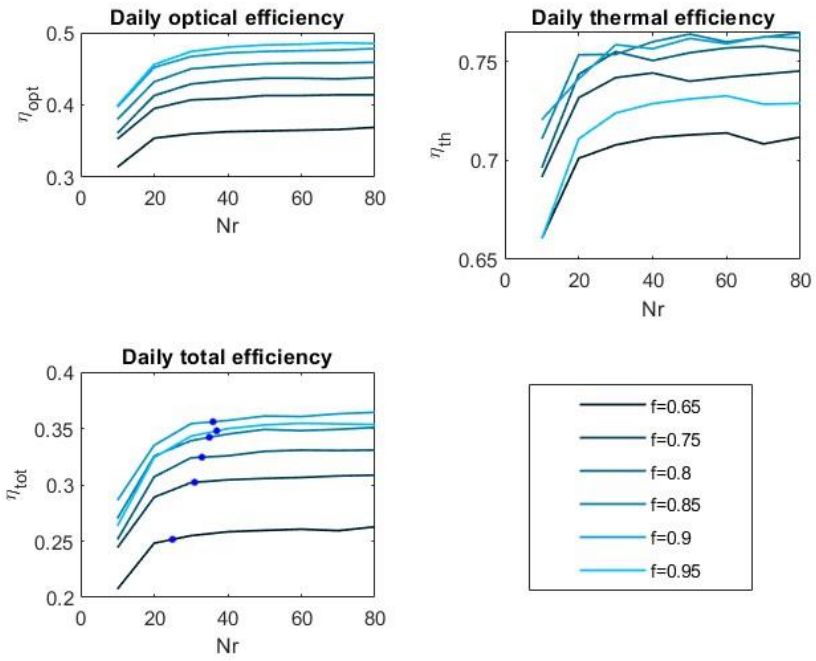

Figure 8-1 Daily optical, thermal and global efficiency of noon-optimized layouts with a target temperature of 600°C as function of Nr and parametrised for hyperbola shape factor.

The thermal efficiency has a slightly more erratic behaviour. The general trend for this quantity is again to increase with the number of rows. This is due to the higher power conveyed on the absorber by configurations with higher Nr: this determines an earlier start of the process in the day and so more energy is used by the process.

The trend of the global efficiency is determined mainly the daily optical efficiency. The actual value instead is highly influenced by η_{day}^{th}. The effect of the target temperature is particularly interesting: as the target temperature increases, the curve of thermal efficiency gets lower and lower, determining a decrement of the global efficiency. This decrement is higher as the absorber width increases: configurations at very high values of f (i.e., $f = 0.95 \div 0.99$) would suffer from low thermal efficiencies as the temperature increase since they have the highest values of w_{abs} (configuration with $f = 0.95$ has the bigger absorber width in *Figure 3-22* and the difference with the values of $f = 0.9$ are very high: it is reasonable to assume that the absorber for a configuration with $f = 0.99$ would have an even higher increase). As the target temperature increases, the configurations at high hyperbola shape factor become less and less efficient.
A techno-economic analysis should be carried out to account for determine the actual best configuration both in terms of both primary focus height and number of rows since the global efficiency doesn't show a maximum but instead an asymptotic behaviour in Figure 8-1.
A criterion for the choice of the optimal configuration is instead selected. In commercial LFR systems the focus height revolves around 5-7 meters and it coincides with the actual height of the receiver. Choosing to position the hyperbolic cylinder too high could expose to technical problems such as increased cost of the support structure and lower resistance to wind loads, even if the actual vertex of the hyperbola is lower than h. For this reason, a maximum height of the primary focus point is assumed to be 10 meters. For configurations of this height (blue marked points in *Figure 8-1*), usually the asymptote of the global efficiency can be considered reached. A further increase in number of rows would mean only an increase of power on the absorber and consequently of energy available to the process, not of the efficiency of the system.

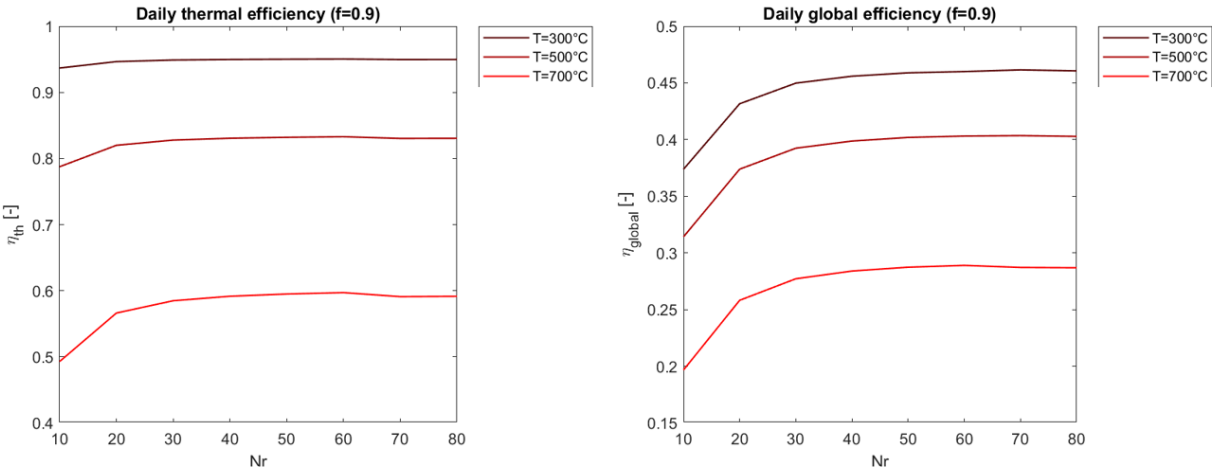

Figure 8-2 Thermal (left) and global (right) daily efficiencies as function of the number of rows a parametrised according to the target temperature.

The optimal layout is choses as the most efficient (daily global efficiency) from the layouts that have a primary focus height inferior to 10 meters (better performing layout among the blue-marked points in *Figure 8-1*). The choice of the layout depends on the target temperature as previously mentioned. The presence of a value of f that maximise the global efficiency is highlighted in red in *Figure 8-3*.
The optimal configuration is selected for three different values of target temperature: 400°C, 500°C and 600°C. The main geometrical parameters that define the layouts and the performance parameters are summarised in Table 8-1.

		Target temperature $\overline{T}$ [°C]		
		400	500	600
Geometrical parameters	Hyperbola shape factor, f [-]	0.95	0.9	0.9
	Number of mirror rows, Nr	37	36	36
	Primary focus height h [m]	9.7393	9.93	9.93
	Absorber width, w_{abs} [m]	0.4155	0.3534	0.3534
	Hyperbola width, w_{hyp} [m]	1.8862	3.339	3.339
	Geometric concentration ratio, C_g [-]	89.05	101.75	101.75
Performance parameters	Daily optical efficiency, η_{day}^{opt} [%]	47.82	47.00	47.00
	Daily thermal efficiency, η_{day}^{th} [%]	90.25	84.83	75.73
	Daily global efficiency, η_{day}^{global} [%]	43.16	39.87	35.60

Table 8-1 Geometrical and performance parameters of the optimal layout obtained the selection procedure described in Chapter 8 for different target temperatures.

For a target temperature of 400°C the optimal configuration has an hyperbola shape factor equal to 0.95 while for 500°C and 600°C the optimal configuration presents $f = 0.9$. For both these last two cases, the geometrical parameters are the same, meaning that the layout configuration is identical. As the temperature increases, the detriment of the thermal efficiency becomes evident.

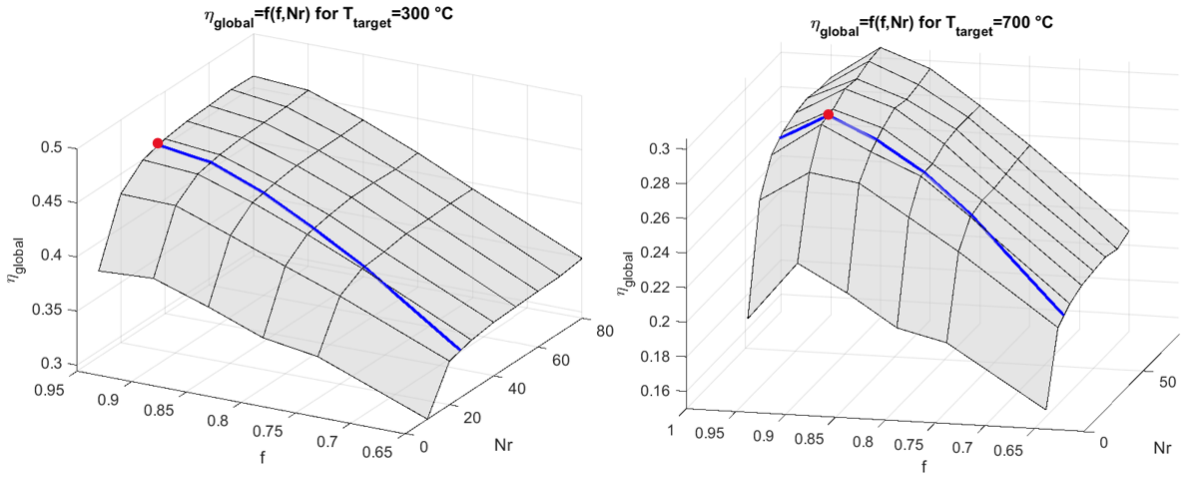

Figure 8-3 Daily global efficiency surface as function of number of mirror rows and hyperbola shape factor for different target temperatures.

9 Conclusions

In the present thesis work the methods and principals for the optical design of a beam down linear Fresnel reflector have been defined and investigated.

Firstly, the beam down technology required has been defined: the second reflective stage consists of a hyperbolic cylinder in whose focus point coincides with the one of the mirror field. The effects on the geometry of this component of the hyperbola shape factor have been state as well.

An ideal model of the BDLFR system has been implemented in Matlab. This model is used to compute the value of the main geometric parameters of the system such mirror positioning (studied to avoid blocking at noon of the spring equinox for a latitude of 40°N), hyperbola and absorber width. On the computation of this last quantity, the results yielded by the edge ray method proposed by Sánchez-González and Gómez-Hernández was compared with ones obtained with an alternative two-dimensional edge ray method, this one based on the projection on the transversal plane of the solar cone impinging on the mirrors. The comparison with a SolTrace simulation revealed that the second method is better capable of approximating the three-dimensional sequence of reflections of the solar cone from the centre of the last mirror row to the absorber passing through the beam down stage. The intercept factor on the absorber when the absorber width is computed with the 2D method is greater than 95% for distances of the last mirror row up to 500 meters; for distances lower than 100 meters the intercept factor reaches values close to 100%.
Once the method for the computation of the absorber width was consolidated, the ideal model was used to analyse how the beforementioned quantity responds to the variation of other geometric parameters such as primary focus point height, number of mirror rows and hyperbola shape factor. In particular, for fixed hyperbola shape factor and number of mirror rows, the existence of a primary focus height that minimizes the absorber width was demonstrated and the resulting optimal curves analysed.
The ideal model was then used to extract a first estimate of the instantaneous optical efficiency of the system and the main optical losses of the system.

A non-ideal model of the BDLFR system has been implemented in SolTrace. Using the geometrical input provided by the ideal model, the optical errors have been introduced in the SolTrace simulations to better estimate the optical efficiency of the system. To this end a second method, this time base on a series of SolTrace simulations, to evaluate the optical losses of the system has been defined.
The two methods for the evaluation of optical losses have been compared in two different scenarios: sun vector laying on the transversal plane and sun vector describing the trajectory of the sun in the sky of a reference day (spring equinox): the ideal method equals the non-ideal in the first analysis but in the second lacks accuracy, underestimating the optical efficiency of the system by about 8%. From this analysis is evinced that the main sources of optical loss of the system are cosine effect, present in all hours of the day because the primary focus point is not rigidly connected with the tracking surfaces like in a PTC system, hyperbola shading and shading mirror-to-mirror loss (main limiting factor of the optical efficiency when the

sun is far from the noon condition). The maximum optical efficiency is reached by the system at noon with a value of about 51%.

Daily and annual optical efficiencies of the system have been defined. In the effort to provide a time-efficient method to compute the annual efficiency of the system without recurring to a huge number of SolTrace simulations, the Incidence Angle Modifier surfaces have been introduced as function of the transversal incidence angle and the angle between the sun vector and its projection of the transversal plane. Incidence Angle Modifier curves have been computed for the BDLFR systems and a correction coefficient to allow the shift from IAM surfaces to IAM curves has been defined and studied. In particular the dependence of said correction coefficient from mirrors focal length and position has been investigated. The annual efficiency of a constantly spaced configuration (1 meter) with a primary focus height of 5.5 m, hyperbola shape factor of 0.8 and mirrors width of 0.5 m yielded an annual efficiency of 44.68% while the one of a noon-optimized presented a yield of 39.38%. This indicates that designing the mirror field to maximize the optical efficiency in noon condition and so gaining and advantage in terms of energy collected in the central hour of the day, is not rewarding as the energy loss in the other hours of the day is too high.

A simplified thermal model of the receiver has been defined to estimate the radiative losses of the system when a generic process uses the thermal power provided by the optical system, leading to the definition of daily and annual thermal efficiency of the system. The global efficiency of the system was defined as the product of optical and thermal efficiencies. The control logic of the underlying process was defined.

The three models where used to select an optimal configuration of the system, choosing from the ones with a noon-optimized mirror spacing that minimized the absorber width. The selection procedure takes into account both the daily global efficiency of the system and some technical constraints (i.e., limit on the primary focus height). The selected configuration depends on the choses operating temperature of the system.

For a target temperature of 500°C the selected optimal layout presents an hyperbola shape factor equal of 0.9, primary focus height of 9.93 meters with a mirror field of 36+36 mirrors. The global efficiency of such configuration amounts to 39.87%.

10 Bibliography

[1] "European Green Deal".

[2] "Database documentation." [Online]. Available: https://www.iea.org/terms.

[3] S. sro, "Solargis yearly maps Global Horizontal Irradiation Product note," 2020. [Online]. Available: https://solargis.com

[4] A. Rabl and N. Y. Oxford, "Active Solar Collectors and Their Applications," 1985.

[5] A. Giostri, M. Binotti, P. Silva, E. MacChi, and G. Manzolini, "Comparison of two linear collectors in solar thermal plants: Parabolic trough versus Fresnel," *Journal of Solar Energy Engineering, Transactions of the ASME*, vol. 135, no. 1, 2013, doi: 10.1115/1.4006792.

[6] A. Sánchez-González and J. Gómez-Hernández, "Beam-down linear Fresnel reflector: BDLFR," *Renew Energy*, vol. 146, pp. 802–815, Feb. 2020, doi: 10.1016/j.renene.2019.07.017.

[7] A. Segal and M. Epstein, "THE OPTICS OF THE SOLAR TOWER REFLECTOR †," 2000. [Online]. Available: www.elsevier.com/locate/solener

[8] T. Wendelin, A. Dobos, and A. Lewandowski, "SolTrace: A Ray-Tracing Code for Complex Solar Optical Systems," 2013. [Online]. Available: http://www.osti.gov/bridge

[9] S. Taramona, P. Á. González-Gómez, J. V. Briongos, and J. Gómez-Hernández, "Designing a flat beam-down linear Fresnel reflector," *Renew Energy*, vol. 187, pp. 484–499, Mar. 2022, doi: 10.1016/j.renene.2022.01.104.

[10] R. Winston, "Principles of solar concentrators of a novel design," *Solar Energy*, vol. 16, no. 2, pp. 89–95, 1974, doi: https://doi.org/10.1016/0038-092X(74)90004-8.

[11] S. A. Kalogirou, "Chapter 3 - Solar Energy Collectors," in *Solar Energy Engineering (Second Edition)*, Second Edition., S. A. Kalogirou, Ed. Boston: Academic Press, 2014, pp. 125–220. doi: https://doi.org/10.1016/B978-0-12-397270-5.00003-0.

[12] A. M. Bonanos, "Error analysis for concentrated solar collectors," *Journal of Renewable and Sustainable Energy*, vol. 4, no. 6, Nov. 2012, doi: 10.1063/1.4768546.

[13] A. B. Meinel and M. P. Meinel, *Applied Solar Energy: An Introduction*, vol. 45. 1976.

[14] P. Boito and R. Grena, “Optimization of the geometry of Fresnel linear collectors,” *Solar Energy*, vol. 135, pp. 479–486, Oct. 2016, doi: 10.1016/j.solener.2016.05.060.

[15] P. Boito and R. Grena, “Optimal focal length of primary mirrors in Fresnel linear collectors,” *Solar Energy*, vol. 155, pp. 1313–1318, 2017, doi: 10.1016/j.solener.2017.07.079.

[16] W. R. Mcintire~, “FACTORED APPROXIMATIONS FOR BIAXIAL INCIDENT ANGLE MODIFIERSt,” 1982.

[17] S. Balaji, K. S. Reddy, and T. Sundararajan, “Optical modelling and performance analysis of a solar LFR receiver system with parabolic and involute secondary reflectors,” *Appl Energy*, vol. 179, pp. 1138–1151, Oct. 2016, doi: 10.1016/j.apenergy.2016.07.082.